2021

Embedded Energy Landscapes In Soft Matter For Micro-Robotics And Reconfigurable Structures

Tianyi Yao
University of Pennsylvania

Recommended Citation

Yao, Tianyi, "Embedded Energy Landscapes In Soft Matter For Micro-Robotics And Reconfigurable Structures" (2021). *Publicly Accessible Penn Dissertations*. 4968.
https://repository.upenn.edu/edissertations/4968

Embedded Energy Landscapes In Soft Matter For Micro-Robotics And Reconfigurable Structures

Abstract

The ability to manipulate microscale objects with precision to form complex structures is central to the field of micro-robotics and to the realization of reconfigurable systems. Understanding and exploiting the forces that dominate at the microscale in complex environments pose major challenges and open untapped opportunities. This is particularly the case for micro-particles in soft milieu like fluid interfaces or nematic liquid crystalline fluids, which deform or reorganize around dispersed colloids or near bounding surfaces. These energetically costly deformations can be designed as embedded energy landscapes, a form of physical intelligence, to dictate emergent colloidal interactions. The fluid nature of these soft milieu allows colloids to move to minimize the free energy and externally forced robotic structures to re-write the embedded energy landscapes in the domain. Such physically intelligent systems are of great interest at the intersection of materials science and micro-robotics.

Micro-particles on fluid interfaces deform the interface shape, migrate, and assemble to minimize the capillary energy. In the first part of my thesis, I design and fabricate a magnetic micro-robot as a mobile curvature source to interact with passive colloids on the water/oil interface. An analytical expression that includes both capillary and hydrodynamic interactions is derived and captures the main feature of experimental observations. I further demonstrate multiple micro-robotic tasks including directed assembly, cargo carrying, desired release and cargo delivery on the interface.

Micro-particles in confined nematic liquid crystals (NLCs) distort the nematic director field, generating interactions. These interactions depend strongly on the colloids shape and surface chemistry, geometric frustration of director field and behavior of dynamic topological defects. To probe far-from-equilibrium dynamics, I fabricate a magnetic disk with hybrid anchoring. Upon controlled rotation, the disk's companion defect undergoes periodic rearrangement, executing a complex swim stroke that propels disk translation. I study this new swimming modality in both high and low Ericksen number regimes. At high rotation rates, the defect elongates significantly adjacent to the disk, generating broken symmetries that allow steering of the disk. This ability is exploited in path planning.

Thereafter, I design a four-armed micro-robot as a mobile distortion source to promote passive colloids assembly at particular sites via emergent interactions in NLCs whose strengths are characterized and found to be several orders of magnitude larger than thermal energies. While the strength of theses interactions allows colloidal cargo to be carried with the micro-robot during translation, it poses challenges for cargo release. We find that rotation of this micro-robot generates a complex dynamic defect-sharing event with colloidal cargo that spurs cargo release. Thereafter, I demonstrate the ability to exploit NLC elastodynamics to construct reconfigurable colloidal structures in a micro-robotics platform. At the colloidal scale, rotation dynamics are easier to generate, and this motivated me to exploit the topological swimming modality of the micro-robot. Using programmable rotating fields to direct the micro-robot's motion, I achieve fully autonomous cargo manipulations including approach, assembly, transport and release. The ability to dynamically manipulate micro-particles and their structures in soft matter systems with embedded energy landscapes, as demonstrated in this thesis, creates new possibilities for micro-robotics and reconfigurable systems.

Degree Type

Dissertation

Degree Name

Doctor of Philosophy (PhD)

Graduate Group

Chemical and Biomolecular Engineering

First Advisor

Kathleen J. Stebe

Subject Categories

Chemical Engineering

EMBEDDED ENERGY LANDSCAPES IN SOFT MATTER FOR MICRO-ROBOTICS AND RECONFIGURABLE STRUCTURES

Tianyi Yao

A DISSERTATION

in

Chemical and Biomolecular Engineering

Presented to the Faculties of the University of Pennsylvania

in

Partial Fulfillment of the Requirements for the

Degree of Doctor of Philosophy

2021

Supervisor of Dissertation

Kathleen J. Stebe,
Richer & Elizabeth Goodwin Professor of Engineering and Applied Science

Graduate Group Chairperson

John C. Crocker, Professor of Chemical and Biomolecular Engineering

Dissertation Committee

Nader Engheta, H. Nedwill Ramsey Professor of Electrical and Systems Engineering

Daeyeon Lee, Professor of Chemical and Biomolecular Engineering

Amish J. Patel, Associated Professor of Chemical and Biomolecular Engineering

EMBEDDED ENERGY LANDSCAPES IN SOFT MATTER FOR MICRO-ROBOTICS
AND RECONFIGURABLE STRUCTURES

Tianyi Yao

To my beloved parents, grandparents and lovely wife

ACKNOWLEDGEMENT

I would like to thank my thesis advisor, Professor Kathleen J. Stebe for her guidance throughout my doctorate years. Thank you for introducing me the to beauty of soft matter in your class and generously offering me the opportunity to join your group when I was a master student in the department. The work presented in this thesis would not have been possible without your inspiring ideas, consistent support during tough times and unending passion toward unknown problems. Your hard working attitude and constant striving for excellence motivate and help me to become a critical researcher and I am extremely grateful to have you not only as my research advisor but also a life mentor.

I would also like to thank my committee members Professor Nader Engheta, Professor Daeyeon Lee and Professor Amish Patel. Thank you all for being great teachers and mentors and for serving on my thesis committee. Discussions with all of you have always been helpful and inspiring and it is a great honor to have all of you on my committee.

I am also grateful to my undergradute adviser, Professor Mei Wang at Dalian University of Technology (DUT) and my mentor in the undergraduate lab who is also a professor at DUT now, Professor Peili Zhang for guiding me into scientific research and motivating me to pursue a graduate degree.

All the work in this thesis would not have been possible without my wonderful collaborators. I would like to thank Dr. Edward Steager for helping me with the control system, Dr. Nicholas Chisholm for discussions on hydrodynamics, Dr. Žiga Kos for performing beautiful liquid crystals simulations, Professor Miha Ravnik, Professor Francesca Serra and Professor Daniel Beller for helpful suggestion and insights on the liquid crystals work and Professor Nasim Mohammadi Estakhri for guidance in COMSOL simulations on reconfigurable electromagnetic devices.

I would like to thank all former and present Stebe group members: Ningwei, Liana, Neha, Iris, Sarah, Nate, Lisa, Yimin, Giusuppe DV, Ali, Renjing, Wilfredo, Caroline, Jiayi, Jed-Joan, Arthur, Ivy, Jacky, Oluwafemi, Nick, Mehdi, Xu, Yang, Giuseppe B, and Sam. I am so glad to have worked together with all of you. Special thanks to Iris and Yimin for training me to work with fluid interface and nematic liquid crystals. I really appreciate your time spent with me in the lab. I would also like to thank Ningwei, Iris and Yimin for your help and encouragement during every stage of my doctorate years. You all are great mentors to me in all aspects.

As a student from another country, I have been fortunate to have all the amazing friends in Philadelphia. I would like to thank Yichen Ji and Tianqi Chen for being the best apartment mates for my first two years in Philly and always being supportive. Special thanks to my wonderful DUT and Penn CBE alumnus Yifan Wang for always being a big brother to me and always patiently answering all my questions. Thanks to Daming Shi, Tianren Zhang and Entao Yang for all the fun conversations we had during lunch, dinner, in GYM or even on the way to grab a coffee. I would also like to thank Nate, Ali, Wilfredo, Jiayi and Jed-Joan for chatting with me when I got tired with experiment. I will always remember the times we chat about wines, sports, games, movies, TV shows and other random topics. I would also like to thank the CSSAP (Chinese Students and Scholars Association at Penn) and GAPSA (Graduate and Professional Students Association) for giving me the opportunity to be the MC for multiple stage events, organize several social activities and make a lot of friends.

Finally, I could not have done this without my family. I would like to thank my parents, Weidong Yao and Wentong Yang, for their endless love and support and my parents in law, Xinming Chen and Anxia Pan for their encouragement and understanding. I would also like to thank my cat Lucky for randomly lying around me and waking me up every morning. Last but not the least, I am incredibly thankful to my wife, Shiyu Chen, who has always been there for me during the ups and downs of this journey. Thank you for all the trust, sacrifices and love.

ABSTRACT

EMBEDDED ENERGY LANDSCAPES IN SOFT MATTER FOR MICRO-ROBOTICS AND RECONFIGURABLE STRUCTURES

Tianyi Yao

Kathleen J. Stebe

The ability to manipulate microscale objects with precision to form complex structures is central to the field of micro-robotics and to the realization of reconfigurable systems. Understanding and exploiting the forces that dominate at the microscale in complex environments pose major challenges and open untapped opportunities. This is particularly the case for micro-particles in soft milieu like fluid interfaces or nematic liquid crystalline fluids, which deform or reorganize around dispersed colloids or near bounding surfaces. These energetically costly deformations can be designed as embedded energy landscapes, a form of physical intelligence, to dictate emergent colloidal interactions. The fluid nature of these soft milieu allows colloids to move to minimize the free energy and externally forced robotic structures to re-write the embedded energy landscapes in the domain. Such physically intelligent systems are of great interest at the intersection of materials science and micro-robotics.

Micro-particles on fluid interfaces deform the interface shape, migrate, and assemble to minimize the capillary energy. In the first part of my thesis, I design and fabricate a magnetic micro-robot as a mobile curvature source to interact with passive colloids on the water/oil interface. An analytical expression that includes both capillary and hydrodynamic interactions is derived and captures the main feature of experimental observations. I further demonstrate multiple micro-robotic tasks including directed assembly, cargo carrying, desired release and cargo delivery on the interface.

Micro-particles in confined nematic liquid crystals (NLCs) distort the nematic director field, generating interactions. These interactions depend strongly on the colloids shape and surface chemistry, geometric frustration of director field and behavior of dynamic topological defects. To probe far-from-equilibrium dynamics, I fabricate a magnetic disk with hybrid anchoring. Upon controlled rotation, the disk's companion defect undergoes periodic rearrangement, executing a complex swim stroke that propels disk translation. I study this new swimming modality in both high and low Ericksen number regimes. At high rotation rates, the defect elongates significantly adjacent to the disk, generating broken symmetries that allow steering of the disk. This ability is exploited in path planning.

Thereafter, I design a four-armed micro-robot as a mobile distortion source to promote passive colloids assembly at particular sites via emergent interactions in NLCs whose strengths are characterized and found to be several orders of magnitude larger than thermal energies. While the strength of theses interactions allows colloidal cargo to be carried with the micro-robot during translation, it poses challenges for cargo release. We find that rotation of this micro-robot generates a complex dynamic defect-sharing event with colloidal cargo that spurs cargo release. Thereafter, I demonstrate the ability to exploit NLC elastodynamics to construct reconfigurable colloidal structures in a micro-robotics platform. At the colloidal scale, rotation dynamics are easier to generate, and this motivated me to exploit the topological swimming modality of the micro-robot. Using programmable rotating fields to direct the micro-robot's motion, I achieve fully autonomous cargo manipulations including approach, assembly, transport and release. The ability to dynamically manipulate micro-particles and their structures in soft matter systems with embedded energy landscapes, as demonstrated in this thesis, creates new possibilities for micro-robotics and reconfigurable structures.

TABLE OF CONTENTS

LIST OF ILLUSTRATIONS

Chapter 1

Introduction

1.1. Motivation

The ability to manipulate microscale elements into structures with high-resolution is of broad interest in physics, medicine, biology, and material science. This interest has motivated research to understand the manner in which mobile microscale elements interact with each other and with their milieu, focal points at the heart of colloidal science and soft matter physics. When interactions of elements with each other or with colloidal building blocks are harnessed to perform useful tasks, the fields of colloid science and soft matter physics intersect with micro-robotics. At this intersection, micro-robots driven by external fields exploit interactions of driven colloids, whereas self-propelled micro-robot design is guided by fundamental studies of micro-swimmers. Such micro-robots have been harnessed to investigate microscale physical phenomena, thereby enriching our fundamental understanding. For example, controlled externally driven colloids have been widely used as probes to study hydrodynamics in fluidic environments [1, 2] and as model elements to investigate the collective behaviors of active matter [3, 4, 5, 6]. Micro-robots are also exploited to perform tasks similar to those performed by their macroscale robotics counterparts, but in microscale or confined environments. For example, micro-robotic platforms have been developed to perform complex tasks at the submillimeter scale including micro-manufacturing [7] and construction of reconfigurable micro-structures [8, 9], and have been exploited in many biomedical applications including targeted drug delivery [10, 11], biofilm removal [12], single cell manipulation [13, 14, 15], imaging [16] and biosensing [17].

While the integration of on-board computational intelligence in macroscale robot has proven fruitful, such approaches are not feasible for micro-robotic structures due to their limited physical dimensions. Therefore, large-scale hardware such as computers, cameras, microscopes, and field generators are often exploited for off-board micro-robotics control. However, such approaches typically vary the 'global' environment, making high-resolution microscale control difficult. Furthermore, for micro-robots that rely on physical contact with passive micro-objects, a controllable and reconfigurable end-effector, which can physically interact with passive micro-objects such as pushing or gripping, is commonly designed with complicated microfabrication processes. To advance the state-of-the-art, micro-robotics has turned to the paradigm of physical intelligence [18, 19], in which physical and physicochemical interactions between colloidal scale objects in complex milieu are exploited to direct microrobot behavior.

Physically intelligent soft matter systems in which information can be embedded and exploited are excellent candidates for this domain [20, 21, 22]. Interactions that dominate on the colloidal length scale, such as hydrodynamics, electrostatics, capillary interactions at fluid interface and elastic interaction in anisotropic fluids offer important degrees of freedom and provide massive untapped opportunities for micro-robotics design. In addition, colloidal particle geometry, composition, surface properties, and response to external fields have been designed to guide the actuation and structure formation in soft matter systems [23, 24, 25]. Active colloids, which move via self-propulsion or under an external field, are a particularly exciting and rapidly growing aspect of this field [26, 27, 28, 29, 30]. Fundamental studies of active colloids not only identify locomotion strategies but also develop understanding of emergent interactions and collective behaviors ripe for exploitation in micro-robotics. The work in this thesis is focused on harnessing embedded energy landscapes in soft matter systems, specifically by controlling distortion fields on fluid interfaces and within nematic liquid crystals (NLCs), for micro-robotics and reconfigurable systems. The aim is to develop new physically intelligent platforms that bridge soft matter and micro-robotics to address challenges at the intersection of these domains.

1.2. Locomotion of Microscale Objects

Locomotion of microscale objects, an important feature of microrobotics, is produced by diverse mechanisms in natural and synthetic systems [31, 32, 27, 28, 33, 34]. These objects, also referred as artificial micro-swimmers in (active) soft matter physics, can be driven and move under external fields or be self-propelled by conversion of chemical energy via chemical reaction to generate motion [35]. In addition, swimming microorganisms, such as bacteria, can act as bio-actuators that can be harnessed to drive the motion of micro-objects via surface interactions that do not depend on the material properties of the object. In all cases, hydrodynamic interactions, confinement, and object geometry are of central importance in such systems, affecting locomotion speed and direction [36, 26, 27, 28, 34].

1.2.1. Locomotion by Applying External Fields

Locomotion of micro-objects can be achieved by applying constant or time-dependent external fields, including electro-magnetic fields, acoustic waves, light, and temperature gradients, to exert forces and mechanical torques on the object [27, 28, 37, 34]. Among these examples, magnetic fields are the most widely investigated as they can be applied and programmed externally using electromagnetic systems [38], interact selectively with magnetic materials, and are biocompatible. Actuation of a magnetic object relies on the application of magnetic field gradient to generate a force, or a rotating field to generate a magnetic torque. For example, magnetic microparticles with simple shapes can be driven by a magnetic field gradient and directed to move along desired trajectories in various media such as bulk fluids [39] and fluid interfaces [40]. More complex waveforms can generate interesting responses. For example, a dispersion of magnetic microparticles at liquid-air interface can self-assemble into a magnetic ‘snake’ under a vertical alternating magnetic field and swim at the interface [41]. Furthermore, swarms of magnetic micro/nanoparticles have been directed to move in confined channels and to clean biofilm covered surfaces under external field [42, 12]. Time-dependent fields applied to magnetic particles with more complicated shapes have been designed to break the symmetry and avoid the scallop theorem [43]. For instance, the application of a rotating field to chains of magnetic colloids cemented by DNA

[44], to helical structures [45, 46, 47] and to flexible nanowires [48, 49] results in motions similar to those of biological flagella which generate propulsion in bulk fluids. Near solid boundaries, magnetic rollers [50, 6, 51, 52], nanowires [53, 54] and colloids of asymmetric shapes [55] can also translate under a rotating magnetic field due to broken symmetry of viscous stresses near the walls. For example, Tierno et al. demonstrated translational movement of DNA-linked anisotropic dumbbell shaped colloids consisting of two paramagnetic colloids of different sizes under a conical field. The processing motion of the colloid near the solid boundary generate broken symmetry in viscous effects that propels the motion of the colloid.

Micro-objects can also be actuated using electric fields. In the case of charged colloidal particles, the velocity at which the particle moves due to a balance between electrical and viscous forces is linearly related to the strength of the applied DC field, a phenomenon known as the electrophoretic motion [56]. Janus particles with broken symmetry have been predicted to generate an unbalanced liquid flow due to induced-charge electro-osmosis under an alternating electric field [57]. Gangwal et al. experimentally demonstrated the unidirectional motion of Au-coated colloids in NaCl solutions under a uniform AC field with frequencies in the range from 100 Hz to 10 kHz via induced-charge electrophoresis [58]. In addition, when dielectric and metal microparticles are placed in anisotropic fluids such as nematic liquid crystals, more complex dynamics associated with their translation emerge due to the dielectric anisotropy of the elongated nematogens [59, 60].

Light can be used to generate heat and impose thermal gradients that drive motion. For example, when a metal-coated Janus colloid is illuminated with a laser beam, a temperature gradient along the particle can be generated due to the nonuniform heating on the particle surface. Such gradient leads to a self-thermophoretic motion that propels the colloid. The rate of migration of Au-coated Janus particles moving thermophoretically can be controlled by tuning the power of the illuminating laser [61, 62]. The high laser intensity gradient that is typically required in these settings can also generate optical forces which can be directly exploited for colloids manipulation [63, 64] and interfere with the thermophoretic motion. In contrast, actuation can be achieved using very low light intensities if the Janus particle is immersed in a critical binary liquid mixture; the local demixing results in concentration gradient across the particle and, therefore, leads to the active motion of the particle which can be easily tuned by illumination [65, 66, 67, 68]. In addition to thermophoretic motion, a hexagonal micro-platelet with self-assembled monolayer of photosensitive molecules has been shown to rotate and translate under a time-dependent linearly polarized light in nematic liquid crystal due to the distortion of the elastic field around the colloid [69]. Forces can also be applied to micro-objects using acoustic waves. It has been shown that MHz frequency acoustic wave can propel, align, rotate and assembly metallic micro-rods in water; the shape asymmetry leads to a self-acoustophoretic mechanism which drive the directional motion of the micro-rod [70].

1.2.2. Locomotion by Conversion of Chemical Energy

Unlike the systems discussed above that rely on external fields to generate motion, microscale objects can also be actuated by harnessing chemical energy embedded in the environment via chemical reaction. The reaction can create a local electrostatic or chemical gradient that leads to a self-phoretic motion of the object. Typically, the self-generation of gradients by a particle requires broken symmetry in the location of the reactive site or in the drag response to the phoretic motion. This broken symmetry can be controlled by the particle's shape, material or chemical heterogeneity. Following this logic, pioneer works by Paxton et al. [71] and then Fournier-Bidoz et al. [72] demonstrated experimentally the enhanced directed motion of gold-platinum (Au-Pt) and gold-nickel (Au-Ni) micro-rods when they were placed in hydrogen peroxide H_2O_2 solutions. These bimetallic micro-rods can be modeled as electrochemical cells: a redox reaction occurs at the two ends of the micro-rod, where protons are created (at Pt/Ni end) and consumed (at the Au end), and an internal electric current is required to maintain this reaction. Fluid flow is generated that propels the rod due to the proton flux along its length. Proton flux can also be achieved via a bioelectrochemical redox reaction of glucose and oxygen and a similar locomotion behavior has been shown using conductive carbon fibers coated with glucose oxidase and bilirubin oxidase at two ends, respectively [73]. Alternatively, bubble formation in H_2O_2 aqueous solutions can also drive the motion of tubular structures with catalytic materials. For example, micro-jets whose internal wall are coated with Pt decomposes H_2O_2 into water and oxygen. Oxygen produced in the reaction accumulates in the tube and forms gas bubbles, which are eventually ejected from one end of the tube and propel the motion of the micro-jet in the opposite direction [74, 75]. In contrast to electrically conductive systems, propulsion can also be achieved using dielectric Janus particles where dielectric colloids are partially coated with thin layer of catalytic materials such as Pt or palladium (Pd). When such particles are immersed in an aqueous solution enriched with H_2O_2, they locally decompose it into water and oxygen, and thus create a local concentration gradient that eventually leads to self-diffusiophoresis as first demonstrated by Howse et al. [76] using Pt-coated micro-spheres.

In addition to phoretic forces, Marangoni stresses can also generate particle propulsion [77]. Experimentally, this has been demonstrated using a micron-sized droplet of bromine water immersed in a surfactant-laden oil phase. Due to the spontaneous bromination reaction of the surfactant at the interface, a self-sustained bromination gradient along the drop surface is generated that eventually leads to a Marangoni flow and propels the droplet [78, 79]. Similarly, spontaneous self-propulsion has also been demonstrated for pure water droplets that are stabilized in an oil phase with surfactants above the critical micellar concentration (CMC) [80]. More recently, Dietrich et al. reported active micrometric Marangoni surfers by applying laser light to induce the asymmetric heating of Janus colloids adsorbed at water-oil interfaces. The coupling of temperature and surfactant concentration gradients generates Marangoni stresses that propels the colloid [81].

1.2.3. Locomotion by Swimming Microorganisms

Another approach for the locomotion of micro-objects is using swimming microorganisms as bioactuators to propel the motion of passive object [35]. For example, in one of the pioneering works from Sitti's group, Behkam et al. demonstrated that flagellar motors inside the intact cell of Serratia marcescens bacteria could be used for controlled propulsion of a 10 µm polystyrene passive colloid [82]. In the same year, Steager et al. showed the propulsion of a triangular micro-object placed on the surface of swarming Serratia marcescens [83]. Later, Di Leonardo et al. achieved spontaneous and unidirectional rotation of a micro-rotor by immersing the object in an active bacterial bath of motile Escherichia coli (E. coli) cells; the asymmetric geometry of the gear teeth biased the motion of the bacteria and led to an effective torque that rotate the colloid [84]. Since then, various designs and bacteria have been investigated including a micro-bio-robot comprising a motile sperm cell trapped in a magnetic microtube [85], polyelectrolyte multilayer coated polystyrene micro-particle [86] or red blood cells [87] with E. coli attached to the surface. Vaccari et al. reported bacteria-propelled motion of colloidal particles adsorbed at interfaces, showing distinct trajectories, some with persistent ballistic character, enhanced diffusivities and highly non-Gaussian displacments [88]. Most recently, Rajabi et al. demonstrated a unidirectional motion of a water droplet embedded in thermotropic nematic liquid crystals with swimming bacteria attached to the interface. Random motion of bacteria at the interface led to propulsion due to unbalanced viscous effects results from a fore-aft asymmetric director structure around the droplet [89].

1.2.4. Locomotion by Hybrid Actuation Strategy

Based on the understanding of various locomotion and propulsion mechanisms described above, there has been a trend to develop hybrid actuation strategies for more robust and controllable actuation of micro-objects. A hybrid actuation strategy typically combines one method, either self-powered or externally powered, to provide force for propulsion and another method, based on the application of an external source of energy, to steer the object [90].

Magnetic fields are widely used to steer or regulate the motion of self-propelled micro-swimmer as magnetic torque is proportional to the magnitude of the field and magnetic moment of the object. For example, micro-swimmers propelled by various mechanisms, including self-diffusiophoresis [91], bubble formation [75] or encapsulated sperm cells [85] can be easily directed using external magnetic fields, allowing the control over their moving trajectories. Similarly, microcapsules with air bubbles trapped in them can translate near a solid surface in an aqueous environment via a hybrid mechanism in which acoustic wave is used to generate propulsion forces and magnetic field is used to break the symmetry and regulate the motion [92, 93]. In a different system, passive colloids trapped at fluid interface can migrate, via capillary interactions, toward a high curvature gradient site created by a magnetic micro-particle whose motion can be controlled by an external field [40]. Capillarity can also be exploited to generate torque through local temperature variation produced by light absorption. Using this mechanism, asymmetric micro-gears, coated with light-absorbing material and suspended at a liquid-air interface, can spin at hundreds rpm under wide field illumination with incoherent light [94]. In addition to local heating, light can also be exploited to control self-propelled motion generated by photochemical reactions as light can be instantaneously turned on and off, allowing immediate control over the motion of the micro-swimmer. For example, photosensitive catalysts such as hematite and titanium dioxide (TiO_2) have been investigated to replace Pt of Pd on Janus particles in order to introduce extra degree of freedom; those materials can only catalyze the decomposition of H_2O_2 when illuminated with light, allowing control over the on-and-off of the reaction and thus the propulsion [4, 95, 96]. While the systems mentioned above only exemplify how two or more strategies can be combined for more complicated locomotion, a more complete review can be found in [90].

1.3. Micro-robotic Cargo Manipulation in Soft Matter Systems

Despite various locomotion mechanisms achieved in soft matter systems review above, artificial swimmers need to be equipped with additional functionalities to perform complex microrobotic tasks. Examples of these functionalities include cargo manipulation [46, 97, 9, 98], dynamic collective behaviors [99, 100, 50, 101, 102] and incorporated functional materials [103, 12, 104]. In this section, recent progress on cargo manipulation is reviewed; this is a particularly exciting area of microrobotics that is of great interest to soft matter and material science community.

Over the last decade, great effort has been made to identify novel approaches for cargo micro-manipulation which is the key to a broad range of micro-robotic applications such as directed assembly, drug delivery and single cell manipulation [34]. Conventionally, this can be achieved through direct contact (e.g. pushing, rotating or gripping) between the micro-robot and passive cargo. Helical micro-swimmers has been shown to push or steer passive colloids via direct contact in aqueous solutions [45, 46]. Furthermore, various strategies, including spatial confinement and magnetic attraction, have been explored to stabilize the loading and carrying process. For instance, micro-robots with on-board micro-holders can carry and transport passive cargo more stably and several designs has been demonstrated such as a U-shaped micro-robot [105, 39], a helical micro-machine with a micro-holder attached to one end [106], and responsive reconfigurable micro-grippers [107, 108, 9, 109]. Both 2-dimensional and 3-dimensional manipulation has been achieved in aqueous environments. Magnetic attraction between the micro-robot and the cargo has been studied as another approach to stabilize the cargo manipulation process [110, 111]. For example, directed transport of magnetic polymeric drug carriers by a flexible magnetic swimmer has been achieved via the magnetic attraction between the nickel segment on the swimmer and the iron oxide nanoparticles encapsulated in the polymeric drug carriers [111]. Despite robust manipulation capacity, these approaches typically require high-resolution control over the micro-robot and sophisticated multi-step fabrication process that limit some of the potential applications.

Exploitation of interactions that emerge in soft matter systems and dominate in the microscale has been a promising and rapidly growing field at the intersection of microrobotics and colloidal science to develop systems for non-contact manipulation. Interactions intrinsic in soft matter systems, including hydrodynamic interactions between immersed colloids and between colloids and boundaries, and capillary interactions at fluid interface, have been explored for cargo micro-manipulation. A widely studied approach involves the use of various types of fluid flows adjacent to the mircro-swimmer generated by their motions [97, 112, 113, 114, 115, 116, 117, 118, 98, 119, 120]. Depending on the type of swimmer and details of its locomotion and actuation mechanism, the flow around an approaching swimmer may trap or push away the target cargo. For example, the flow generated by a rotating micro-swimmer can be exploited for entrapment and release of cargo particles [114, 115, 116, 117, 119, 120]. Micro-swimmers with helical tails and encapsulating heads have been shown to generate vortices through rotation which can be used to capture and lease cargo [116, 117, 120]. In a different system, micro-rollers near a solid surface are able to translate due to the broken symmetry of viscous effects on top and bottom and to generate micro-vortices adjacent to the micro-roller. These vortices have also been exploited for cargo manipulation [113, 114, 119].

To allow extra degrees of freedom and relieve strict demands on control resolution and micro-fabrication, researchers have started to consider interactions that rely on information embedded in the soft matter environments, which typically emerge spontaneously. For example, capillary interactions have been demonstrated as an efficient tool to guide the migration of passive colloids [121] and assemble micro-and-nanoscale objects [122] at interfaces and, therefore, hold tremendous promise for microrobotics. Thanks to the trending drive for interdisciplinary research, these interactions have drawn more attention of the microrobotic community recently. For example, directed assembly and transport [123, 124] of sub-millimeter passive cargo have been demonstrated by harnessing attractive capillary interactions between a millimeter scale robot and passive cargo at fluid interface.

Moreover, magnetic particles can also self-assembled to form stable groups on the interface by both capillary and magnetic interactions; those structures can also be actuated on the interface and transport cargo [125]. Recently, we have used robots on the scale of hundreds of microns at fluid interfaces to direct assembly, transport, desired release and delivery of passive colloids of tens of micrometers using a capillary interactions that are dominant for particles with negligible weights on a water/oil interface [40]. These results will be described in greater details in Chapter 2. More complicated hybrid systems in which capillary interactions are integrated with other effects for various microrobotic tasks have also been shown [126, 127].

There are other soft matter systems in which colloidal interactions emerge due to the information embedded in the form of boundary energies and curvatures. For example, the elasticity of NLCs gives rise to elastic interactions that have been utilized to direct the assembly of colloids in the domain. Despite the ability to guide the motion of colloids, the exploitation of those emergent interactions remains largely unexplored for micro-robotics.

1.4. Outline of Thesis

My thesis is focused on harnessing embedded energy landscapes in soft matter systems, specifically on oil/water interfaces and in NLCs, for micro-robotics and reconfigurable systems. In both systems studied, magnetic micro-robots are used as mobile information sources that generate local energy landscapes and emergent interactions with neighboring colloids that can be harnessed for cargo manipulation. On fluid interface, the magnetic micro-robot deforms the interface around it, creating sites with high curvature gradients that direct the assembly of passive colloids via capillary interaction; in NLCs, the magnetic micro-robot distorts the director field around it, creating topological defects and regions of high distortion that are attractive to passive colloids through elastic interactions. These interactions have tremendous promise for micro-robotic materials manipulation in multiple aspects; first, the emergent interactions are long-ranged and direct the colloidal cargo to particular assembly sites. This reliance on emergent interaction differs significantly from approaches that rely on hard contact between the micro-robot and passive cargo, and enables untethered manipulation. Secondly, the motion of passive cargo is guided by the energy landscaped embedded in the environment and does not require high-resolution control over the position and orientation of the micro-robot. Finally, these interactions rely on passive cargo shape and surface chemistry and are independent of the details of cargo material properties. This materials-agnostic aspect of these interactions gives significant degrees of freedom with potential applications in the design of reconfigurable devices. The works in this dissertation share the same aim, that is to develop new platforms exploiting interactions dominant in the microscale, and bridge soft matter and micro-robotics for directed assembly, micro-manipulation and reconfigurable systems. This thesis consists of 6 chapters and they are briefly outlined as below:

In chapter 2, I describe directed assembly and micro-manipulation of passive micro-particles at fluid interface using a magnetic micro-robot. A simple theoretical model is derived to describe the interplay of hydrodynamic and capillary interaction at the interface. I compared theoretical expression with experimental results and find qualitative agreement. Directed assembly toward higher curvature gradient sites, cargo capture, transport, release, and delivery to desired sites are achieved. Numerical simulations are performed to help understand the curvature field around micro-robots.

In Chapter 3, I develop the concepts of energy stored in far-from-equilibrium topological defects in NLC. This chapter focuses on understanding topological defect-propelled swimming of nematic colloids. We observe that colloids, forced to rotate in NLC, translate in the domain. We characterize this swimming behavior, propose possible mechanisms with scaling analysis, and demonstrate the ability to plan particle paths. Pair interaction between swimmers are also investigated.

Chapter 4 focus on quasi-static colloidal interactions in NLCs via emergent interactions with boundaries in which colloidal “keys” interact with boundary “locks” via a nematic lock-and-key mechanism. By matching the distortion around a colloid with distortion around the boundary, we demonstrate directed assembly of spherical and ellipsoidal colloids near a wavy wall. This research establishes that colloids near boundaries with given shapes and anchoring interact and assemble via emergent interactions, and motivates our study of a mobile colloid with shape designed for lock and key interactions, We design a 4-armed magnetic micro-robot and study the director field around it. Finally, we investigate multiple modes of static emergent interaction between this micro-robot and a passive colloid. Analysis of the energy map generated from numerically simulated director field around the micro-robot successfully captures trajectories of colloids being assembled into different configurations as observed in experiments.

In Chapter 5, the aforementioned magnetic micro-robot is actuated in NLCs using a permanent magnet, or it is forced to swim via action of its topological defects. Unique defect dynamics observed as the 4-armed micro-robot rotates are explored. Thereafter, the mobile micro-robot is exploited to perform multiple micro-robotic tasks. We achieve cargo capture, transport, dynamic release, and delivery in NLCs using non-equilibrium defect dynamics. Furthermore, we demonstrate construction of various colloidal structures using this micro-robotic platform. Finally, trajectory planning of the micro-robot and a fully autonomous cycle of micro-robotic cargo manipulation including approach, assembly, transport and release are achieved.

Chapter 6 summarizes key findings in this thesis and identifies opportunities and open questions for future investigation of the field.

Chapter 2

Directed assembly and micro-manipulation of passive particles at fluid interfaces via capillarity using a magnetic micro-robot

This chapter is adapted from [40] which was originally published on Applied Physics Letter [Yao, Tianyi, Nicholas G. Chisholm, Edward B. Steager, and Kathleen J. Stebe. Applied Physics Letters 116, no. 4 (2020): 043702.].

2.1. Introduction

The need to assemble microscale elements into structures with high-resolution is of broad interest in materials science and micromanufacturing. This interest drives research at the intersection of micro-robotics and colloidal science to manipulate and assemble colloidal building blocks and to control their structures via external electric [58, 128, 129] and magnetic fields [46, 130]. However, such field-driven strategies are limited to colloids with specific material properties and are ineffective for passive colloids that do not respond to the applied fields. In order to manipulate passive colloids, robotics strategies have been applied, including contact [39, 9] and non-contact manipulation [131, 132]. However, these schemes typically rely on complex geometry and high resolution control. Capillary interactions at fluid interfaces hold tremendous promise for robotic directed assembly. These interactions are a powerful tool to assemble passive colloids [133], and to integrate responsive and passive particles [134, 135, 125] into robust structures that can be driven by external fields. In the robotics arena, the manipulation and assembly of passive particles have been achieved by exploiting capillary interactions between sub-millimeter particles and a millimeter scale robot [123]. While this hybrid approach of using a magnetically driven robot to interact via capillarity with passive particles should apply to smaller, micro-scale robots and to colloids of negligible weight, the origin, range and strength of capillary interactions differ significantly from the heavy, larger counterparts. Far from contact, capillary interactions are dominated by a ubiquitous interaction that occurs for all micro-particles at fluid interfaces. However, near contact, interactions depend strongly on micro-robot geometry, which can be designed to achieve particular tasks. These include site specific attachment with tunable interaction strengths, which can be harnessed to transfer micro-particle cargo to docking sites. This programmable assembly via geometry opens new opportunities for micro-robotics and programmable structures.

In this Chapter, I harness capillary interactions between magnetic micro-robots and passive polystyrene particles trapped at fluid interfaces. To exploit recent findings of capillary forces that attract micro-particles to sites with high interface curvature [136, 137], directed assembly and micro-manipulation of these particles are achieved. In particular, I design micro-robots with different shapes and use visual feedback to control their position using an custom-built electromagnetic control system. I start with a circular micro-robot and demonstrate attraction via an interplay of capillary and hydrodynamic interactions between a moving micro-object and a passive particle trapped at the fluid interface. The interactions are complex as both the micro-robot's motion and capillary interactions contribute significantly to the dynamics. Directed assembly of passive particles toward high curvature sites in the interface generated by the micro-robot is achieved using the sharp corners and associated strong capillary interactions on a square micro-robot. The curvature of the robot's features are modulated modulate by making a flower-shaped robot in order to reduce the strength of the capillary interactions, allowing weaker binding of the particle which enables desired release of colloidal cargo. Finally, a docking station was designed with out-of-plane undulations and strong capillary interactions, and we successfully deliver passive cargo from a micro-robot to this station.

2.2. Background

2.2.1. Capillarity Background

When a particle attaches to an interface between immiscible fluids, it deforms the shape of the interface. This deformation is determined by the particle's weight, and by the shape of the contact line or the contour where the interface and particle meet. The shape of this contour is typically highly undulated owing to contact line pinning at sharp edges or on surface features like roughness sites or chemical heterogeneities [138].

The capillary energy, E_c, associated with the interface deformation is given by

$$E_{cap} = \gamma \Delta A, \tag{2.1}$$

where γ is the surface tension and ΔA is the change in interface area because of the interface deformation. The importance of particle weight relative to surface tension forces is determined by the magnitude of the non-dimensional Bond number:

$$Bo = \frac{ga^2\Delta\rho}{\gamma}, \tag{2.2}$$

where g is gravitational acceleration, a is the characteristic length of the particle, and $\Delta\rho$ is the density difference between the two phases respectively.

For heavy particles with finite Bo, the particle weight, corrected for buoyancy pulls downward, creating a downward sloping interface toward the object. A pair of heavy particles trapped at the interface attract each other with interaction force derived by Scriven et.al [139]. In pioneering work, particles with well-defined, complex shapes, prescribed wetting conditions and finite Bond numbers were assembled into a variety of structures guided by both capillary interactions owing to their weight and their complex contact lines by Whitesides group by tuning the weight and wetting condition of those objects [140, 141, 142].

For small particles, typically $Bo \ll 1$, so surface tension forces dominate and gravitational forces are negligible. For example, the micro-robot and the polystyrene beads I used in my system have Bo number $\sim 10^{-3}$ and 10^{-5}, respectively. Thus, particle weight for the passive particles is orders of magnitude less than the magnetic micro-robot. A detailed inspection of the fluid interface shape in experiment is needed to address capillary interactions between these entities. Theory can provide some guidance.

If we neglect particle weight, and assume small slopes for the interface shape, the interface height obeys the Laplace operator to leading order. The monopole term in this solution is excluded if weight is negligible. The dipolar term is excluded if body torques owing to moments of weight distribution are negligible. The quadrupolar mode is then the leading order deformation that defines far field interface shape and, therefore, defines the far field interaction between such objects [143]. The distortion from the reference height of the interface made by the particle $h_{particle}$ is given by

$$h_{particle} = h_{qp} \frac{a^2}{r^2} cos 2\phi, \tag{2.3}$$

where h_{qp} is the magnitude of the quadrupolar mode, r is the radial distance from the particle center in a coordinate located tangent to the interface and ϕ is the azimuthal angle.

This leading order mode in the interface distortion is also key to understanding interactions between the particle and the shape of the fluid interface. The disturbance associates with a capillary energy in an interface with varying deviatoric curvature Δc, defined as the difference between principal curvatures: $\Delta c = \frac{1}{R_1} - \frac{1}{R_2}$, where R_1 and R_2 are principal radii of the interface. This curvature captures the saddle-like shape of the interface. The curvature capillary energy results from the area minimization of a quadrupolar surface distortion, in which the quadrupole rotates to align its rise axis along the rise axis of the host interface. The resulting curvature capillary energy for an aligned quadrupole is given by:

$$E_p = -\frac{\pi}{2}\gamma a^2 h_{qp} \Delta c. \tag{2.4}$$

For a micro-particle with characteristic length around 10 µm, it creates a quadrupolar distortion, as shown in Fig. 2.1, at hexadecanewater interface with h_{qp} in the range of tens of nanometers. When trapped at a curved interface created using a micropost as in [136, 137, 144], the corresponding curvature capillary energy is in the range of $10^4 k_b T$ which results in the non-Brownian, deterministic path for those microparticles at curved interface.

The associated capillary force, F_p, moves particles along the direction dictated by the deviatoric curvature gradient:

$$F_p = -\nabla E_p = \frac{\pi}{2}\gamma a^2 h_{qp} \nabla(\Delta c), \tag{2.5}$$

where the gradient is evaluated at the center of the particle.

This expression predicts that particles move along the interface from regions of low deviatoric curvature to regions of high deviatoric curvature. That is, an energy landscape is embedded in the shape of the fluid interface that can guide the migration of small particles on the interface. Such a curved interface can be prepared by pinning the contact line at desired location with the help of microstructures, such as a micro-pillar. The Stebe lab has focused on assembling particles using capillary forces on curved fluid interface. For example, Cavallaro et.al. report that micro cylinders on curved fluid interfaces deforms the interface with a quadrupolar deformation. Once the particle attaches to the curved interface, it rotates to a particular orientation, and migrates to high curvature site [136]. Additionally, the migration and assembly of micro disks and spheres at the interface display similar migrations to sites of high curvature [137, 144]. In addition to these attractive interactions, repulsion in the near-field between wavy particles with different wavelengths or similar-sized micro-post and disks have also been reported [145, 146].

2.2.2. Magnetics Background

Magnetic forces and torques on the magnetic robot result from the applied magnetic field in the workspace and are used to control the pose of the robot. A gradient in the magnetic field exerts a force on a magnet, **F**, calculated by:

$$\mathbf{F} = (\mathbf{M} \cdot \nabla)\mathbf{B}, \tag{2.6}$$

where **M** is the magnetization of the permanent magnet and **B** is the magnetic field. The magnetization of the permanent magnet rotates to align with the direction of the field. The torque applied on the magnet, τ, is calculated by:

$$\tau = \mathbf{M} \times \mathbf{B}, \tag{2.7}$$

When stationary electromagnetic coils are used, the magnetic field generated by a current loop can be derived using the Biot-Savart equation:

$$\mathbf{B_{loop}} = \frac{\mu_0 I}{4\pi} \int_C \frac{d\mathbf{s} \times l}{|l|^2} \tag{2.8}$$

where I is the current, μ_0 is the permeability constant for air, l is the unit vector from the coil wire segment to the point of interest, and a closed integral is taken around the entire current loop, C, for each infinitesimal segment $d\mathbf{s}$.

Using a point dipole model [147] for estimation. the magnetic field generated by a coil with radius R centered radially at $[x, y] = [0, 0]mm$, with a current I is given by:

$$B_x = \frac{\mu_0 I R^2}{4r^3}\left[2 - \frac{3y^3}{r^2}\right], \tag{2.9}$$

$$B_y = \frac{3\mu_0 I R^2 xy}{4r^5}, \tag{2.10}$$

where B_x and B_y are the components of the magnetic field in the x and y direction respectively and $r = \sqrt{(x^2 + y^2)}$, the distance from the center of the coil.

2.2.3. Magnetic micro-robots at fluid interfaces

To develop control over assembly at fluid interfaces, the interplay of magnetic fields, capillary interactions and hydrodynamic interactions has been exploited. Magnetic particles, placed on the interface, deform the interface shape around them. Particles can interact through capillary interaction and form assemblies that can be actuated under external magnetic field. There is emerging literature using magnetic fields and capillary interaction to build reconfigurable systems or to control micro-robot assembly. Grosjean et al. [148] used three soft ferromagnetic beads several hundred microns in diameter powered by externally applied magnetic fields to swim across a water/air interface. The resulting millimeter scale structure is self-assembled by capillary interactions. These interactions remain strong for smaller particles, making scaling the system to micro-scale applications feasible. Additionally, micro manipulation and assembly of passive parts using magnetic actuation has been demonstrated with the help of capillary interactions. The same group, later on, presented complicated locomotion of self-assembled magnetic clusters and exhibited applications such as capture of heavy particles and mixing [125]. More recently, He at al. showed capture, transport and release of microbeads with diameter of $400\,\mu\text{m} \sim 800\,\mu\text{m}$ at water/air interface using a magnetically actuated pentagram-shaped microrobot with external diameter of $800\,\mu\text{m}$ [124]. Moreover, by tailoring the geometry of a millimeter robot, directed assembly of $200\,\mu\text{m}$ passive micro-spheres was achieved at hexadecane/water interface [123]. Passive particles migrate toward the corners of a triangular robot which are the regions with highest curvature at the interface. Once assembled, the robot can transport the passive particle on the fluid interface under external field [124]. More recently, complicated hybrid systems in which capillary interactions are combined with other effects for various micro-robotic tasks at fluid interface have also been demonstrated [126, 127].

2.3. Materials and Methods

2.3.1. Fabrication and surface roughness characterization of magnetic microrobots

The magnetic micro-robots are made of SU-8 2050 epoxy resin (MicroChem Corp.) with 2wt% iron (II III) oxide nanopowder (Sigma Aldrich) on a 4 inch silicon wafer (UniversityWafer, Inc.) using standard lithographic methods as shown in Fig. 2.2. First, the silicon wafer is plasma etched for 60 seconds using oxygen (Plasma Etch, Inc.) prior to lithography. The mixture of photoresist and magnetic nanopowder is spin-coated onto a silicon wafer before soft bake at 65° for 5 min and then 95° for 20 min. Next, the wafer is transferred to a mask aligner (OAI Model 100) and exposed to 365 nm UV through a photomask. The substrate is hard baked at 65° for 5 min and then 95° for 12 min. After cooled to room temperature, the wafer is immersed in a petri dish with SU-8 developer (MicroChem Corp.) for 20 min with gentle agitation and then washed with IPA and dried. Subsequently, a layer of nickel is sputtered on the surface of the particle using physical vapor deposition (Lesker PVD75 DC/RF Magnetron Sputterer) and an example of a resulting micro-robot is shown in Fig. 2.3(a). Finally, particles are magnetized with a permanent magnet (K&J Magnetics, Inc.) along the horizontal direction before being released from the wafer using a razor blade or micro-pipette tip.

The surface roughness of the micro-robot is characterized using a optical profilometer (Zygo NewView 7300) and the particle surface after sputtering shows ridge-like roughness in the order of tens of nanometers as shown in Fig. 2.3. Those rough sites can pin an undulated contact line between the oilwater interface along the top edge of the micro-robot and therefore creating interfacial deformation around the object.

2.3.2. Applying an external magnetic field

In this work, the field gradient required to move the microrobot can be generated either using a custom-built electromagnetic control system describe below or a permanent magnet (K&J Magnetics, Inc.). The electromagnetic control system consists of four electromagnetic coils (APW Company) mounted on an aluminum supporting structure arranged around the workspace as shown in Fig. 2.4; visual feedback is provided by a CCD camera (Point Grey Grasshopper3 Monochrome) mounted on a Zeiss inverted microscope (ZEISS Axio Vert.A1). A data acquisition board (USB-3104, Measurement Computing) is used to control the current via a custom power electronics circuit. Each coil is connected with a DC power supply (XG 850W, Sorensen) whose output is controlled using a self-developed Python algorithm to generate the desired magnetic field. In this work, only two coils, one of each pair, are energized at a time to create the field gradient required for translation depending on desired trajectory. The direction of motion can be tuned by changing the ratio of currents on powered coils. Alternatively, the magnetic field is applied by using a permanent NdFeB magnets (K&J Magnetics, Inc.) attached to the end of a tweezers. The magnet is placed parallel to the interface at roughly 0.5 cm from the sample, creating a field gradient strong enough to move particle in arbitrary directions.

2.3.3. Formation and characterization of oilwater fluid interface

The oil-water interfaces were confined in a small circular glass petri dish with diameter of 1 inch. The entire substrate is cleaned by multiple rinses with isopropanol and deionized water (Milli-Q Integral 5, EMD Millipore Corp., water conductivity = $18.0\,\mathrm{M}\omega$), followed by oxygen plasma treatment, which makes the surface hydrophilic. Immediately thereafter, a 2 mm layer of deionized water is added to the petri dish above which the oil phase (Hexadecane, $\geq$ 99%, Sigma-Aldrich, used as a received) is slowly added to cover the entire water phase. Polystyrene micro-particles ($2a$=45 µm and 90 µm, Spherotech Inc.) are triple rinsed with deionized water before being diluted and dispersed in hexadecane. Then, micro-particles suspension is gently pipetted and dispersed onto the oilwater interface by sedimentation through the oil phase. Finally, individual micro-robot is directly introduced to the interface using a micro-needle.

The interface shapes around the micro-objects are characterized using interferometry by a gel-trapping technique [149]. A 2 wt% aqueous gel solution is prepared by adding gellan gum (Kelcogel, supplied by CPKelco) in 3 batches into deionized water preheated to 95 °C followed by gentle shaking. The aqueous solution was then cooled to 60 °C and gently poured into a Petri dish. Micro-particles from a similar waterethanol suspension were spread onto the air-gellan solution interface, after which the entire sample was cooled to room temperature for 30 min to fix the gel.

Random pinning of the contact line on the passive particles and on the micro-robot sets the magnitude of the quadrupolar deformation around each object. For structures with rough edges, like the micro-robots, the quadrupolar distortion is similar to the amplitude of the roughness. For the spherical particles, random pinning along the particle sides allows a wide range of amplitudes [138]. Using interferometric imaging, we measure the magnitude of the quadrupolar distortion at a distance four radii away from the center of the passive colloids. We fit this measurement to the functional form $h = h_{qp1}\frac{a^2}{r^2}cos(2\phi + \alpha)$ to extract the magnitude of the quadrupolar mode. Fifteen measurements for $2a$=90 µm polystyrene particles yielded 0.04 µm $<=$ h_{qp1} $<=$ 0.48 µm with average 0.229 µm and standard deviation 0.148 µm. Similarly, we measure the quadrupolar distortion magnitude two radii away from the center of the disk shaped micro-robot. Ten measurements for $2R$=350 µm circular micro-robot yielded magnitudes of the quadrupole ranging from 0.31 µm $<=$ h_{qp1} $<=$ 3.4 µm with average 1.920 µm and standard deviation 1.068 µm. Finally, we measure the quadrupolar distortion magnitude two radii away from the center of the square shaped micro-robot. Five measurements for square with side-length of 350 µm yielded an average 2.05 µm and standard deviation 1.03 µm.

2.3.4. Imaging and micro-particle tracking

Micro-particle trapped at fluid interface is imaged using an Zeiss inverted microscope (Axio Vert.A1) and the trajectories are recorded at 26 frames per second using a CCD camera (Point Grey Grasshopper3 Monochrome). Vibrations were minimized using a nitrogen-floated optical table (8" by 4" CleanTop) mounted to the cement. Image and trajectories are processed and analyzed using ImageJ and MATLAB.

2.4. Simulations of interface shape

Since the interface shape around the micro-object is governed by the Laplacian equation under small Bo number and small slope approximation, they can be solved using the PDE module in COMSOL Multiphysics with governing equation of the interface height h given by:

$$\nabla^2 h = 0. \tag{2.11}$$

within a two-dimensional space confined by the edge of the micro-object and a far-field boundary. Dirichlet boundary conditions of 1) monopolar, 2) quadrupolar or 3) both monopolar and quadrupolar can be applied to the boundaries of the space of interest. The space is meshed using a extremely fine triangular mesh and solved under stationary condition.

Under small slope approximation, the mean curvature H and the Gaussian curvature K of the interface $h(x, y)$ are given by

$$H = \frac{1}{2}\left(h_{xx} + h_{yy}\right), and \tag{2.12}$$

$$K = h_{xx}h_{yy} - \left(h_{xy}\right)^2 \tag{2.13}$$

respectively and the deviatoric curvature $\Delta c = \frac{1}{R_1} - \frac{1}{R_2}$ can be calculated from

$$\Delta c^2 = \left(2H\right)^2 - 4K. \tag{2.14}$$

Therefore, the deviatoric curvature field and its gradient in the space can be derived from the second order derivative of the height profile and its gradient along the x and y directions from the numerical simulation.

Alternatively, another open source package Surface Evolver [150] can also be used to simulate the height profile of the interface around the micro-objects when they are positioned on the fluid interface. Along the edge of the micro-robot and the far-field boundary, the contact lines are pinned with Dirichlet boundary conditions and the linear Young–Laplace equation is discretized with standard second-order finite-difference formulas.

2.5. Results and Discussion

2.5.1. Directed assembly of passive micro-particles using a circular micro-robot

Actuation of the micro-robot enables the interface deformation field, or, alternatively, Δc to be dynamically positioned, allowing passive particles in the vicinity of the micro-robot to be assembled via capillary interaction. When the interface distortions from the micro-robot and from the micro-sphere overlap, the distance between the two will decrease to minimize the deformation area, hence minimizing the total capillary energy through this attractive interaction. Fig.2.5(a) shows a time-stamped image of a $2a$=90 µm polystyrene particles being assembled by a $2R$=350 µm circular magnetic micro-robot. The micro-robot is moving toward the particle at the interface and finally attracts the particle to its edge; their trajectories are indicated in Fig. 2.5(b). The inset in Fig. 2.5(b) shows the interferometric image of the interface height around a circular robot which reveals a weak downward monopole owing to the robot's weight and a quadrupolar deformation in the far field, as shown in Fig. 2.5(c), and irregular distortions owing to the undulated contact line in the near field as shown in Fig.2.5(d). The average magnitudes of the quadrupoles are $h_{qp1} \sim 0.229\,\mu\text{m}$ and $h_{qp2} \sim 1.92\,\mu\text{m}$ as determined from multiple interferometric measurements. As we are neglecting the weak monopolar deformation from its weight, the deviatoric curvature at the center of mass of the particle is expressed as [121] $\Delta c = 12 h_{qp2} R^2/L^4$ where L is the center-to-center distance between the passive particle and the the micro-robot. Therefore, the dominating capillary force is expressed as:

$$F_{cap} = 24\pi\gamma h_{qp1} h_{qp2} a^2 R^2/L^5, \tag{2.15}$$

where γ is the average surface tension of the two phases.

Hydrodynamic interactions also play an important role in this process as the two objects approach on the fluid interfaces. Dani et al. [151] studied pair interactions for identical micro-spheres trapped at oilwater interface and they demonstrated both theoretically and experimentally a velocity reduction due to the hydrodynamic interaction between the pair. We observed similar behaviors between micro-robots and passive particles in the experiment indicated by the red dots in Fig. 2.5(e).

We approximate the flow created by the micro-robot moving at interface under the external field as a Stokeslet plus a potential dipole at its center [2]. Passive micro-particles in the vicinity of the micro-robot can sense both flow field and capillary field. The corresponding approach velocity between a moving micro-robot and the passive micro-particle when moving along line of centers, from Fax$\acute{e}$n's law, is expressed as (see Appendix for derivation details)

$$\mathbf{U} - \mathbf{U_p} = \mathbf{U} - \mathbf{U}\left[\frac{3}{2}\left(\frac{R}{L}\right) - \frac{1}{2}\left(\frac{R}{L}\right)^3\right] + \frac{\mathbf{F}_{cap}}{6\pi\mu a}. \tag{2.16}$$

where $\mathbf{U}$ and $\mathbf{U_p}$ are the velocities of the micro-robot and passive particle, μ is the average viscosity of the two phases and $\mathbf{F}_{cap}$ is given by (2.15).

To examine the validity of (2.16), we substitute the relevant parameters in this expression, including h_{qp1} =0.229 µm, h_{qp2} =1.92 µm, a=45 µm, R=175 µm. The velocity U and separation distance L are extracted from the videos. We plot the approach velocity as a function of separation distance in Fig. 2.5(e) where the theory agrees qualitatively with experimental results. As the micro-robot is driven toward its target from afar, the approach velocity decreases due to long-ranged hydrodynamic repulsive interaction. However, once within a critical distance, $L \sim 2R$, capillary attraction rapidly pulls the pair together. The discrepancy between theory and experiment may come from several sources. First, there are higher order modes for capillary interactions between the objects in the near field. Second, the hydrodynamic model adopted is strictly valid for far field interactions between spheres, while our robot is disk-shaped. A third possible source of error is that we have not accounted for the effect of interface deformation on hydrodynamic drag. However, the theory captures the main features of the interaction and agrees qualitatively with experiment.

2.5.2. Directed assembly toward high curvature gradient sites using a square micro-robot

While the circular micro-robot demonstrates the concept of capillary directed assembly, we exploit a square micro-robot with similar Bo to show the importance of high curvature sites generated in the interface near corners. Because of its weight, the robot rests slightly below the plane of the interface ($\Delta h \sim 0.5\,\mu\mathrm{m}$). This causes strong distortions and associated pronounced deviatoric curvature gradients near the corners. Instead of randomly assembling anywhere as on the circular micro-robot, passive particles near the square micro-robot now migrate to its corner, as shown in Fig. 2.63(a). The deviatoric curvature field and curvature gradient around the square micro-robot with a pinned contact line and weak vertical displacement are simulated via finite element method, performed using COMSOL Multiphysics, as shown in Fig. 2.63(b). The curvature gradient, as shown by white arrows in Fig. 2.63(b) and the magnitude of the capillary force along the diagonal near the corner, as shown in Fig. 2.63(c), indicate the strong local capillary interactions near the corner. These interactions result in a strong capillary bond that is hard to break. Tracking the approach velocity of the pair (Fig. 2.63(d)) reveals the behavior similar to the circular micro-robot far from contact. However, in the near field, rapid approach and strong local attraction to corners are apparent. For smooth heavy robots, corner attraction is predicted to occur over distances comparable to the half-side of the robot. Roughness generates competing interactions; corner assembly can be preserved by increasing micro-robot weight.

For smooth enough square objects in a plane that differs from the far field reference plane, repulsion from planar sides and attraction to the corner is robust. We have previously established that the side of a square structure is repulsive, as the deviatoric curvature is zero at the symmetry point on the side, and increases along curved contours toward the corner [136]. Particles are repelled from the planar sides and directed toward the corner by these gradients in the deviatoric curvature field. This repulsion from sides and attraction toward corners is predicted in in our system for a smooth square micro-robot with a downward distortion of the interface caused by its weight. We simulate the height profile in Fig. 2.7(a) and the corresponding deviatoric curvature (color map) and curvature gradient (vector field) associated with a heavy, smooth micro-robot in Fig. 2.7. The flat side will be repulsive to passive colloids while corners are attractive. In this case, a passive particle would always migrate toward corner of the micro-robot. All vectors within distances comparable to the half-side length of the square point toward the corner. Random roughness competes with this corner attraction. Random roughness along the edges of the micro-robot pins the contact line, which also generates deformation in the interface. (See the ridge-like roughness made in the Nickel sputtering process Fig. 2.3(a)). The leading order contribution from this undulated contact line that dominates far from contact is the quadrupole term. The height and the curvature profile of a quadrupolar distortion is shown in Fig. 2.8. This contribution drives passive particles along radial paths toward the micro-robot, but does not direct particles to the corner.

There is a third contribution that we do not simulate. Small scale random roughness along the particle side of wavelength smaller that the passive particle generates repulsive interactions [145]. These three terms determine the interactions that occur; in the small slope limit that applied to this study, these terms are additive. To ensure robust assembly at corners, micro-robot weight can be increased.

2.5.3. Understanding the critical distance between micro-robot and passive particle

There is a ‘critical distance’ L_c between micro-robot and passive particle. At this distance, capillary attraction attributable to the quadrupolar mode around the robot exceeds hydrodynamic repulsion. This is substantiated in Fig. 2.9(a), in which the 3 terms in the approach velocity given in (2.16) for the particle approaching the disk in the disk fixed reference frame are shown versus distance to contact with the micro-robot surface. The relevant terms include two hydrodynamic contributions, U, the velocity with which the micro-robot is moved toward the disk, the hydrodynamic interaction terms from Faxén’s law, and the capillary force normalized by $6\pi\mu a$.

At a critical distance, capillary attraction grows faster than the hydrodynamic contributions, and the passive particle rapidly approaches the micro-robot surface. We show this for the average quadrupole magnitudes for the disks and particles obtained by interferometry in Fig. 2.9(a) by the black solid line. For circular-shaped micro-robots and for the passive particles, we found a range of magnitudes of quadrupoles. We show as dashed lines in Fig. 2.9(b) the analytical predictions for the average magnitude plus their standard deviations, and for the average magnitude minus their standard deviations. Note that near field capillary interactions are important and are not included in our analysis, as they are determined by random roughness.

This critical distance differs for the results presented for the circular micro-robot of diameter $2R$ and square micro-robot of side $2R$. This difference can be explained by three factors. Most importantly, the passive particle assembles on the corner of the square robot, coming to contact at a center-to-center distance $L = \sqrt{2}R + a$, while the passive particle assembles on the circular disk's edge at a center-to-center distance $L = R + a$. This points to the importance of near field capillary interactions. When graphed against distance to contact, the critical distance for the two cases is similar. Other details differ in the experiments. For example, the the robots were not driven with identical velocities toward the passive particle. Rather, the square micro-robot was moved at a more rapid approach velocity as shown in Fig. **??**. There is third important difference that has appeared in other experiments: While the particles moved along relatively straight trajectories toward the disks until contact, the highly non-uniform curvature field around the square micro-robot creates curvilinear trajectories as shown in Fig. 2.11. The particles avoid the repulsive planar sides of the robot and move via capillary attraction toward the corners of the robot. The complexity of this motion changes the speed of approach.

2.5.4. Particle release by tuning the strength of capillary attraction

Strong capillary interaction is desirable for assembly but not for release. We can prescribe intermediate strength interactions by designing a planar flower-shaped micro-robot of $2R$=350 µm with periodic wavy structure of wavelength λ =40 µm and amplitude A =10 µm. We also make this micro-robot lighter, so the weak weight results in a weaker interface depression. This results in a deviatoric curvature field near each protrusion with gradients that are gentler than those at sharp corners, and the resulting capillary force is one order of magnitude weaker as shown in Fig. 2.12 which makes the release of the assembled particle easier. The 'petals' on the flowers define docking sites, with colloids closest to the micro-robot attaching either to one or two protrusions. The energy from these docking sites is quite local, so colloids approaching the micro-robot chain with each other due to particle-particle interaction. This chain can be transported together with the micro-robot or broken under external torque. As the chain breaks under external torque, assemblies of passive particles, (i.e. the dimer labeled as 1&2 in Fig. 2.13), were released from the micro-robot. Through such process, various structures of particles or passive cargo can be assembled, transported and released at fluid interface.

2.5.5. Delivery of passive micro-particles to more attractive sites

In addition to assembly and release, delivery of passive particles to desirable locations is another important micro-manipulation process toward building micro-structures. To do this, we introduce a passive docking station with out-of-plane undulations to the fluid interface as shown schematically in Figs. 2.15(a) and 2.14. This docking station is fabricated via lithography from the negative resist SU-8 exposed under UV light through an undulated mask that defines the wavy form and length of the docking station. The thickness of the resist film defines the width of the docking station. Contact line pinning on the top wavy edge gives abrupt height change close to the docking station that decays over distances comparable to the wavelength of the feature. Because of this local interface distortion, the deviatoric curvature field, shown in Fig. 2.15(b) using the open-source software Surface Evolver [150], is orders of magnitude stronger than that around the planar micro-robots, as is the associated capillary force. As a result, passive particles can be transferred as cargo from a circular micro-robot to this docking station. After delivering the passive particle to one of the out-of-plane protrusions, the capillary bond between circular micro-robot and passive particle can be broken under external torque as shown in Fig. 2.15(c). The micro-robot is then driven away by external field to complete the transfer process.

2.6. Conclusion

To conclude this chapter, directed assembly and micro-manipulation of passive particles at the fluid interface are achieved via the interplay of hydrodynamic and capillary interactions using magnetic micro-robots. The micro-robot acts as a mobile fluid interface deformation source and generates a flow field as it is maneuvered through the work space to interact with passive micro-particles. Hydrodynamic interaction is more important than capillary attraction in the far field and pushes passive particles away, whereas capillary attraction dominates in the near field and assembles passive particles at high curvature gradient sites. By strategically designing the geometry of the micro-robot, preferred assembly sites, such as corners, for passive particles can be created. Furthermore, the interaction strength can be tuned by modulating the curvature of the micro-robots or out-of-plane shape of docking stations, allowing passive particles cargo to be delivered to desired sites. The strategy we have developed in this chapter will have potential applications in single cell manipulation, bio-sensing and micro-manufacturing.

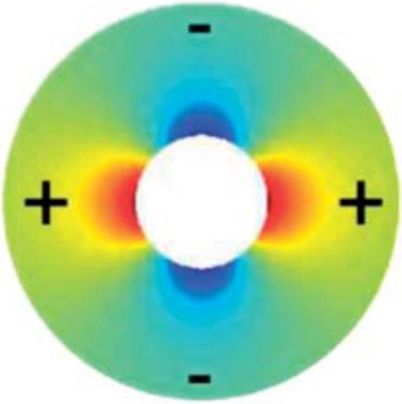

Figure 2.1: Schematics for the shape of the interface around a micro-particle with quadrupole deformation, top view. Adapted from [134].

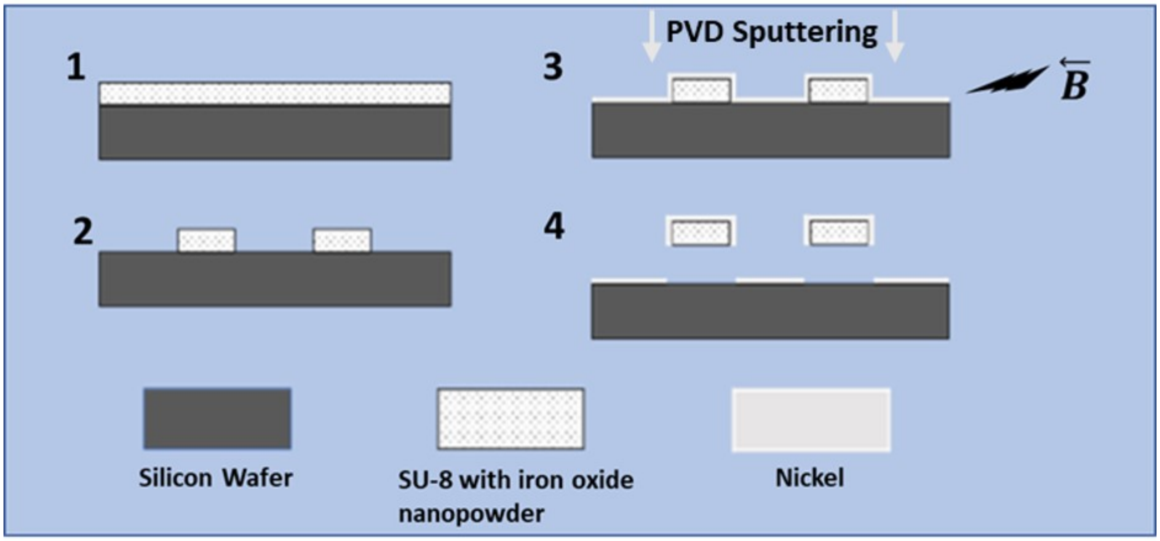

Figure 2.2: Fabrication of magnetic micro-robots using photolithography and PVD sputtering.

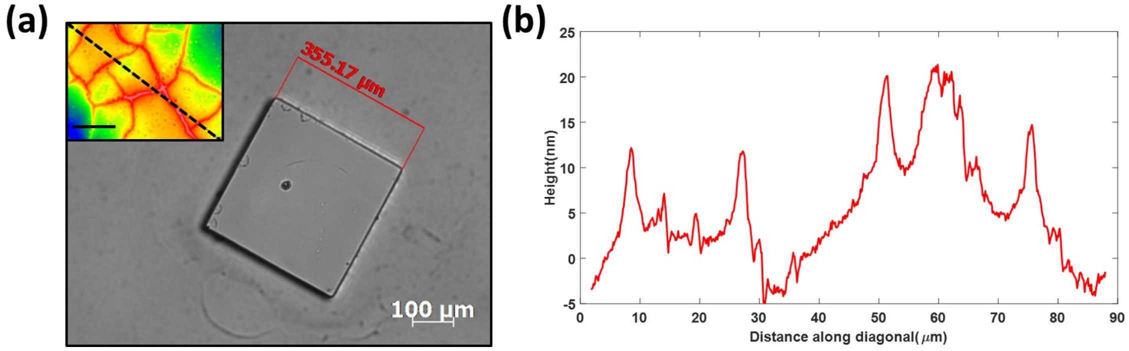

Figure 2.3: Surface roughness: (a) Microscopic image of a square micro-robot with side length S=350 µm after sputtering. Inset: Interferometry image of the sputtered surface. Scale bar is 20 µm. (b) Height profile along the diagonal indicated by the black dash line in the interferometry image in (a) reveals ridge-like surface roughness from the sputtering process.

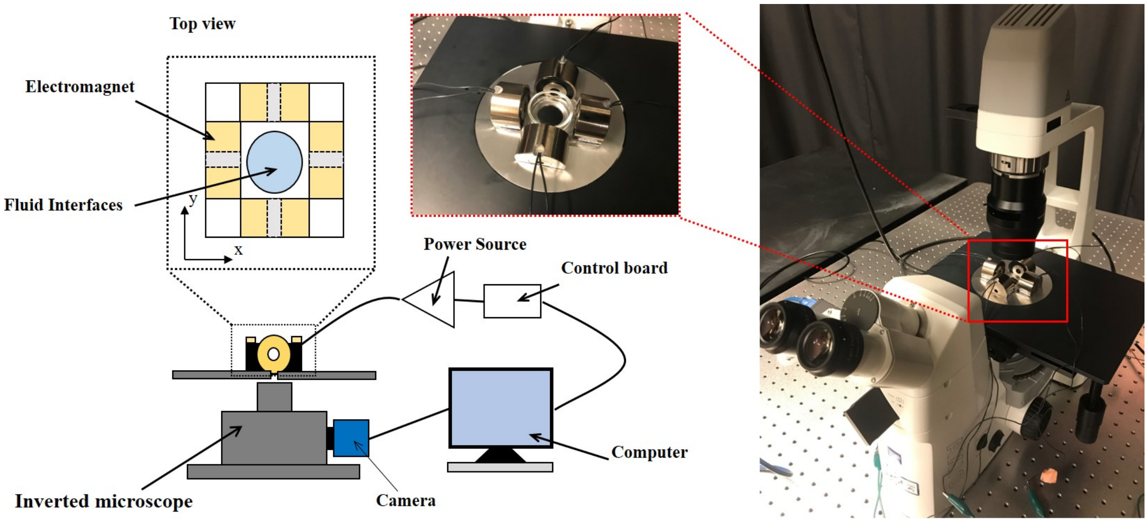

Figure 2.4: Diagram and pictures of the custom-built electromagnetic control system.

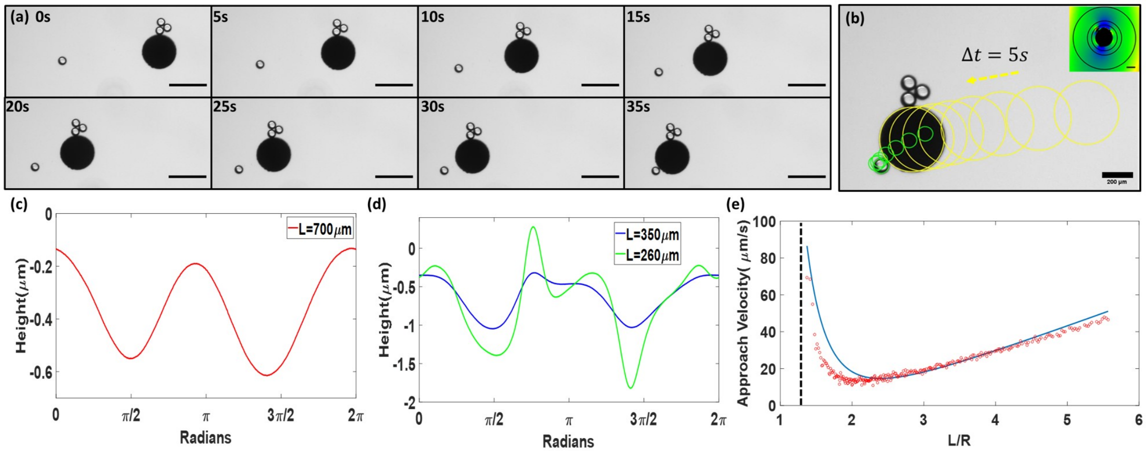

Figure 2.5: (a) Time-stamped image of a $2a$=90 µm polystyrene microshpere being assembled by a $2R$=350 µm circular micro-robot. Scale bar is 400 µm. (b) Trajectories of micro-robot and passive particle. Inset: Interferometry image of $2R$=350 µm circular micro-robot at fluid interface. Scale bar is 200 µm. (c) Height profiles at radial distance L=700 µm from the center of the micro-robot. (d) Height profile at radial distance L=260 µm and 350 µm from the center of the micro-robot. (e) Approach velocity between circular micro-robot and passive particle with dashed line indicating the contact point. Red circles represent experimental results and blue line represents theoretical results given by equation (2.16).

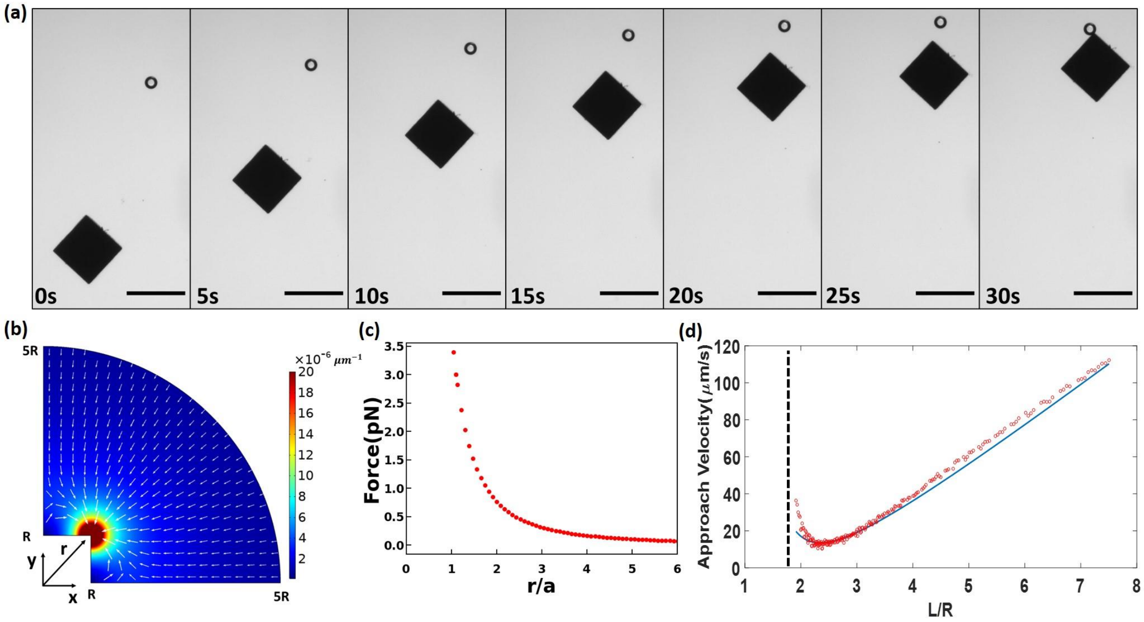

Figure 2.6: (a) Time-stamped image of a $2a$=90 µm polystyrene microspheres migrating toward the corner of a S=350 µm square micro-robot. Scale bar is 400 µm. (b) Finite element simulation of the deviatoric curvature (color map) and curvature gradient (white arrows) of one quadrant around the square micro-robot. (c) Magnitude of the capillary force along the diagonal of the square as a function of the distance from the corner r. (d) Approach velocity between the square micro-robot and passive particle. The side of the robot is equal to $2R$. The dashed line indicates contact between the passive particle and robot at the corner. The red circles represent experimental results; the blue line represents theoretical results given by (2.16).

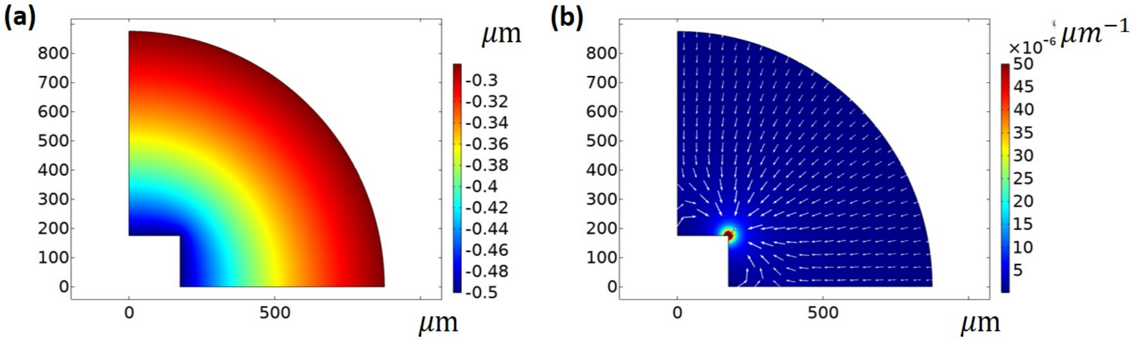

Figure 2.7: COMSOL simulation of the (a) height and (b) curvature (color map) and curvature gradient (vector field) of a smooth square micro-robot that rests at a height below the far field reference plane.

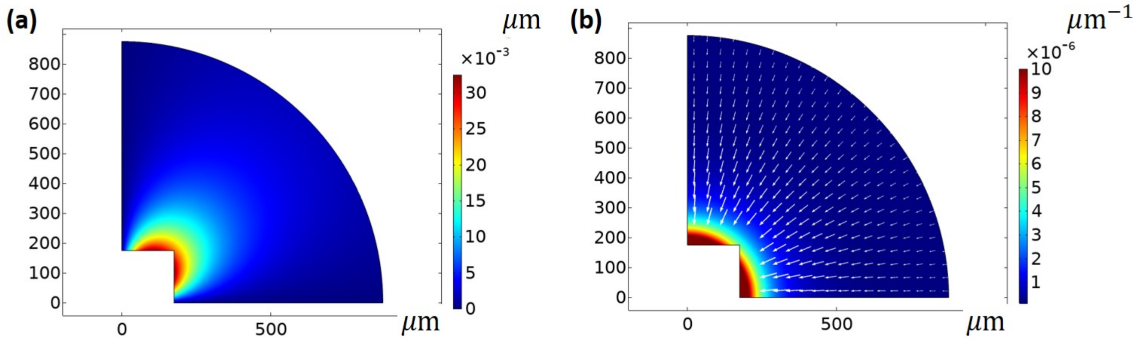

Figure 2.8: COMSOL simulation of the (a) height and (b) curvature (color map) and curvature gradient(vector field) of a square micro-robot with quadrupolar deformation aligned with corners.

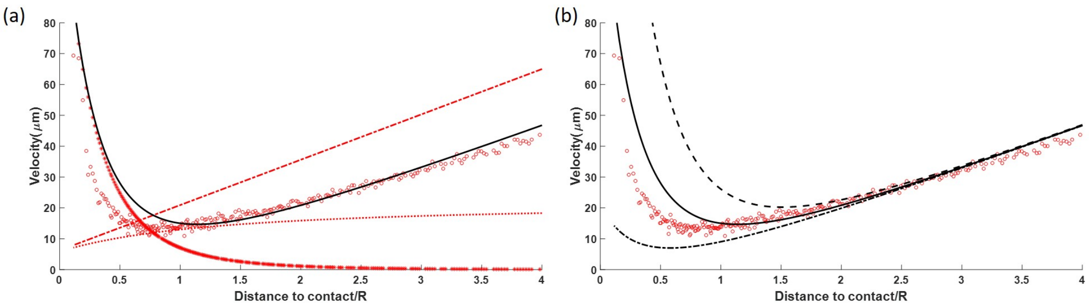

Figure 2.9: Here we show data for $2R$=350 µm circular micro-robot and $2a$=90 µm polystyrene particle, and compare it to theory ((2.16)). (a) Experimental approach velocity (red circles), and theory for interaction based upon average value of quadrupolar amplitudes (black solid line). Each term in (2.16) is also shown, including robot velocity U (red dash-dot line), velocity contribution from hydrodynamic interaction, the second term in (2.16) (red dotted line), and the velocity due to capillary interaction (red stars). The abscissa of this graph is the distance to contact normalized by the radius of the micro-robot R. (b) Comparison between experimental results and theory. We compare theory using average values for quadrupolar magnitudes for passive particle and micro-robot (solid black curve), using the average values plus the standard deviation (black dashed line), and using the average values minus their standard deviations (black dash-dot line).

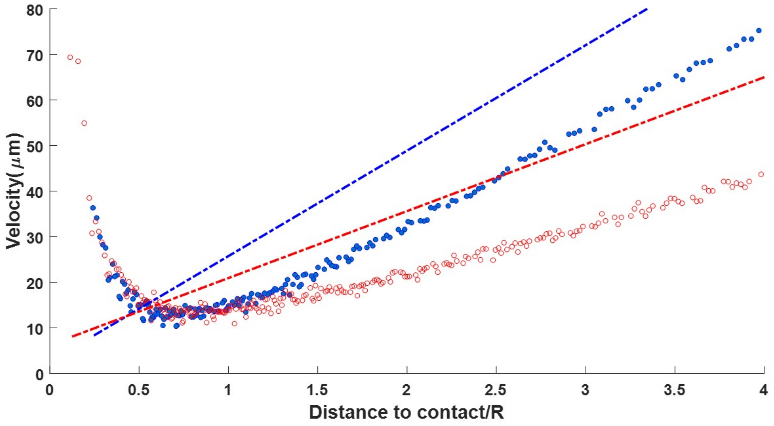

Figure 2.10: Comparison of trajectories near disk shaped and square shaped microrobot versus distance to contact, both of diameter or side length 350 µm interacting with polystyrene particle with $2a$=90 µm. The red dashed line and blue dashed line indicate the velocities U with which the circular micro-robot and square micro-robot were driven. While the two micro-robots were driven at different velocities U, the capillary interactions with the polystyrene particles are similar, and become dominant at similar separation distances, as apparent in the experimental approach velocities between the circular micro-robot (red circles), and square micro-robot (blue dots).

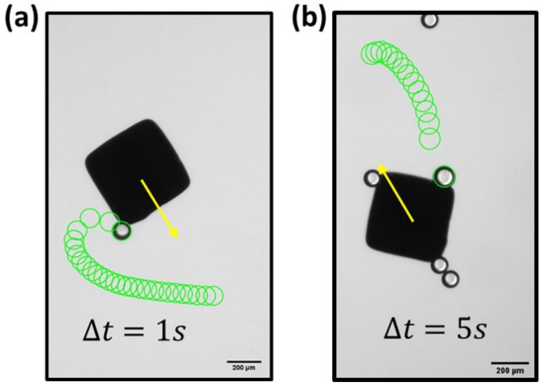

Figure 2.11: Two experiments showing a $2a$=90 µm passive polystyrene bead takes a curved path to the corner of a side length 350 µm square micro-robot where the yellow arrow indicates the moving direction of the micro-robot and green circles indicate the curved trajectories of the passive particle.

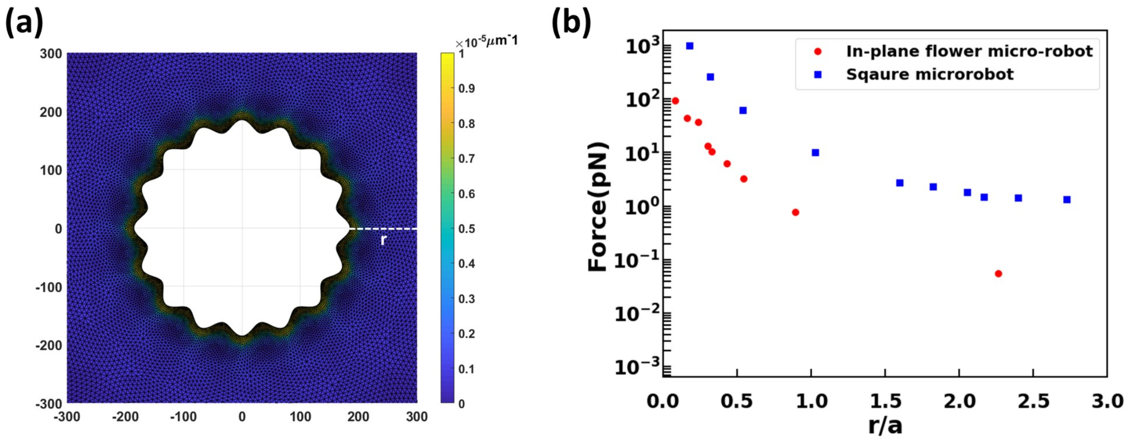

Figure 2.12: (a) Deviatoric curvature field around a in-plane flower-shape micro-robot of $2R$=350 µm with periodic wavy structure of wavelength λ =40 µm and amplitude A =10 µm given by Surface Evolver. (b) Comparison between capillary force along the diagonal of a square micro-robot and capillary force along one of the in-plane protrusions, as indicated by the white dashed line, of the flower-shape micro-robot.

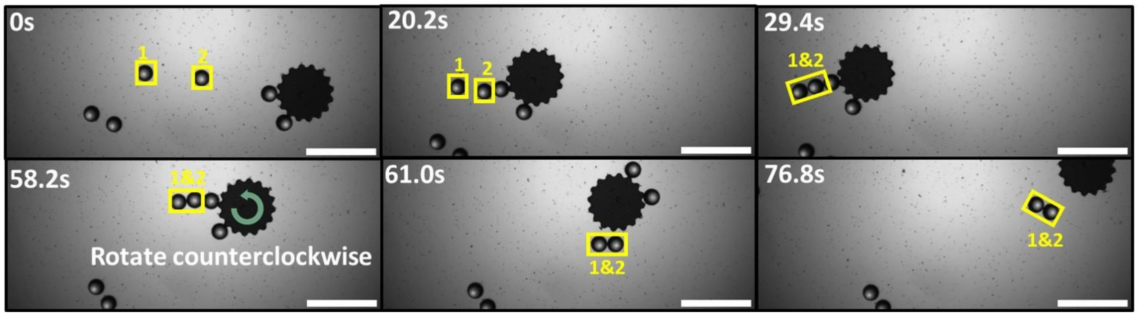

Figure 2.13: (Color online) Time-stamped image of assembly, transportation and release of passive particles at fluid interface using a $2R$=350 µm in plane flower-shape micro-robot. Scale bar is 400 µm.

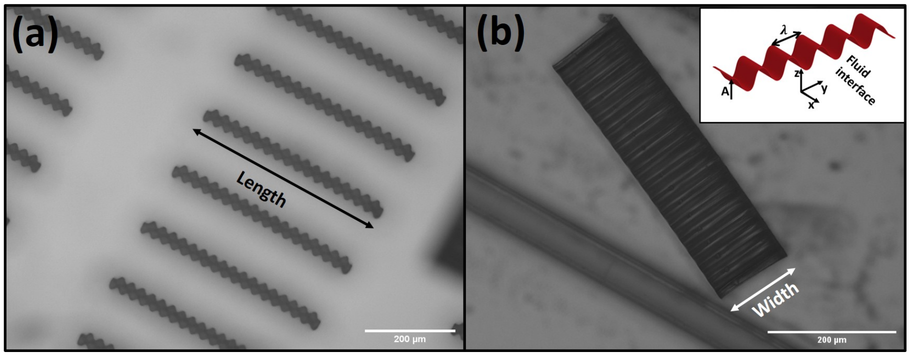

Figure 2.14: Microscopic images of (a) top view and (b) side view of the passive docking station on a silicon wafer. The docking station was fabricated via lithography from the negative resist SU-8 developed under UV light through an undulated mask that defines the wavy form and length of the docking station. The thickness of the resist film defines the width of the docking station. When placed on the interface, those particles lie down as shown schematically in the inset in (b).

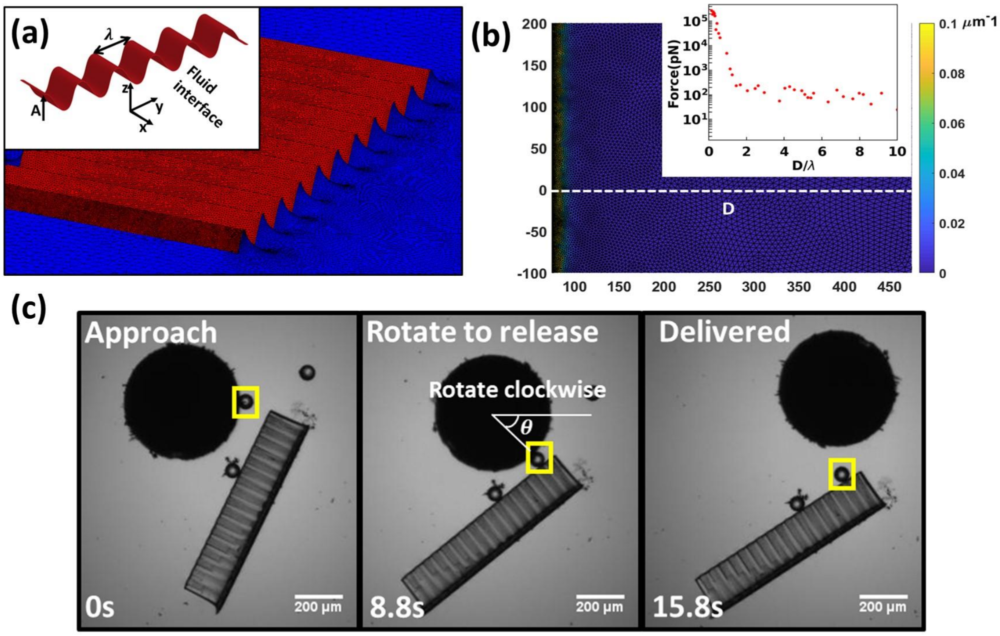

Figure 2.15: (a) Surface Evolver simulation of out-of-plane wavy particle with wavelength $\lambda = 40\,\mu\text{m}$ and amplitude $A = 10\,\mu\text{m}$. Inset: schematics of a wavy particle trapped at fluid interface. (b) Deviatoric curvature near the out-of-plane particle. Inset: Magnitude of the capillary force along one of its bumps indicated by the white dashed line. (c) Delivery of $2a$=45 µm passive particles to the docking station using a $2R$=350 µm circular micro-robot. The micro-robot rotates clockwise for $\Delta\theta \sim 170°$ with $\omega \sim 2.18\,\text{s}^{-1}$ under magnetic torque to break the capillary bond.

Chapter 3

Topological defect-propelled swimming of nematic colloids

Locomotion of colloidal swimmers, an important feature of active matter, is produced by diverse mechanisms in natural and synthetic systems [36, 31, 26, 152, 28, 30]. Self-propelled swimmers convert chemical energy to generate motion with examples including bacteria and algae [153, 154, 155] which swim by rotation of their flagella, Marangoni-stress propelled droplets [77] which move via gradients in surface stresses, and catalytic Janus particles [71, 4] which swim by phoretic motions generated by chemical reaction. Driven systems rely on external fields, including electrophoresis of charged and dielectric particles [56, 58], rotation [55, 6] of magnetic particles in external fields and thermophoretic colloidal motion driven by temperature gradients [61, 62]. Hydrodynamic interactions, confinement, and swimmer geometry [44, 55, 41, 156, 157, 152] are of central importance in such systems, affecting locomotion speed and direction, and can lead to the formation of dynamic aggregates that can be harnessed as functional structures [103, 12].

Interactions of swimmers with their environment play important roles in determining their dynamic behavior [158, 159]. Distinctly anisotropic environments like nematic liquid crystals (NLCs) provide means for controlling the micro-locomotion by a combination of their internal orientational order -described by a headless vector field $\vec{n}$ called the director- and their highly anisotropic viscosities. NLC can exhibit topological defects or regions of lost orientational order in the form of lines, points or even walls that strongly affect the behavior of active nematic colloids [160, 161, 162, 163, 164, 89]. For example, bacteria align and move along the local director [165], causing them to accumulate at sites of splay and to be depleted from sites of bend [166]. Electrophoretically driven colloids move along or perpendicular to the director field, made possible by the fluid's dielectric anisotropy [59, 60]. Marangoni-propelled NLC droplets lose axial symmetry by flow-induced displacement of their topological defects which generate torques that result in helical trajectories [167]. Anisotropic particles that are forced to rotate in NLCs display shape-dependent responses, as their companion defects become topologically unstable and rearrange with complex colloidal dynamics [168, 169, 69, 170]. These latter examples show the importance of broken symmetry and defect dynamics in determining colloid behavior and indicate the general importance of dynamic effects in systems with topological defects.

In this chapter, we introduce the concept of topological defect-propelled swimming of nematic colloids. Specifically, we use ferromagnetic disks with hybrid anchoring in planar cells filled with NLC; a dipolar companion defect loop forms adjacent to the disk, pinned on the disk's sharp edges. The location of the defect defines the disk's polarity. Under continuous disk rotation, we observe periodic defect rearrangements; the disclination loop sweeps along the disk's surface, performing a 'swim stroke' that propels the disk in a well-defined direction. The translation velocity v is determined by the angular velocity ω, the sense of rotation and the defect polarity which enable trajectory planning. These nematic colloid swimmers exhibit complex interactions and form stable and unstable dimers that depend on their polarization and the topology of their defects.

3.1. Background

3.1.1. Liquid crystals

Liquid crystals (LCs) are a state of matter with properties between solid crystals and disordered liquids. The simplest liquid crystalline phase is the nematic phase, formed by rod-like molecules as shown in Fig. 3.1(a). In a continuum limit, the orientational order of NLC molecules is described by a headless vector, termed the director $\mathbf{n}$, along which those anisotropic molecule spontaneously co-orient with their neighbors to minimize the orientational disorder. This spontaneous alignment lead to elasticity, and any deviations from this preferred orientation cost energy. In nematic fluids, the distortion of director field in bulk is manifested in three primary modes: splay, twist and bend [171] as shown in Fig. 3.1(b). The Frank elastic free energy density f_b in bulk is expressed as Eq. 3.1:

$$f_b = \frac{1}{2}K_1(\nabla \cdot \mathbf{n})^2 + \frac{1}{2}K_2(\mathbf{n} \cdot \nabla \times \mathbf{n})^2 + \frac{1}{2}K_3(\mathbf{n} \times \nabla \times \mathbf{n})^2 \tag{3.1}$$

where K_1, K_2 and K_3 are the splay, twist and bend elastic constants, respectively. In commonly studied NLCs, these constants are of similar order of magnitude. For simplification, we adopt the one-constant approximation and assume $K_1 = K_2 = K_3 \sim 10^{-11}N$. The total elastic free energy of a NLC system consists of two parts: the surface energy and the elastic energy due to bulk distortions (Eq. 3.2):

$$F = \int_S f_s dS + \int_V f_b dV \tag{3.2}$$

The surface energy density is expressed by Eq. 3.3:

$$f_s = W(\mathbf{n} \cdot \boldsymbol{\nu})^2 \tag{3.3}$$

where W is the anchoring strength of the surface (expressed in N/m) and $\boldsymbol{\nu}$ denotes the preferred orientation of NLC molecules on the surface.

The preferred molecular orientation at a bounding surface is referred to as the surface anchoring which can be experimentally controlled by applying different surface chemistry. Typically, one can apply either planar anchoring where the NLCs molecule align parallel to the surface by rubbing coated polymeric commanding layers or homeotropic anchoring where the NLCs molecule align perpendicularly to the surface by adsorbing surfactant monolayers. In recent years, more exquisite control of the anchoring has been achieved by microscale lithography [172], micro-rubbing using an AFM tip [173], and photo-alignment

[174, 175, 176].

3.1.2. Topological defects and nematic colloids

Topological defects arise due to frustration of the director field. They are small melted, or isotropic, regions of NLCs where the scalar order parameter S vanishes. S is defined as:

$$S =< 3cos^2\theta - 1 > \tag{3.4}$$

where θ denotes the angle between the molecules and the local nematic director.

Defects are characterized by their topological charge, which in two dimensions can be dictated as the winding number. The winding number is defined conventionally as the angle by which the director $\mathbf{n}$ rotates around the defect, divided by 2π. In NLCs, a positive charge indicates that NLC molecules rotates counterclockwise around the defect while a negative charge suggests clockwise rotation of the nematogens around the defect. Taking a spherical homeotropic colloid as an example, the director rotates counterclockwise by 2π around the surface of the colloid, therefore its charge is $+1$. Nematic liquid crystals also allow defects with semi-integer charges ($\pm\frac{1}{2}$).

The concept of topological charge also applies in the three dimensions. However, in this case, it is not defined in terms of the winding number as the director can now escape into the third dimension. For NLC, since the director is represented by a headless vector ($\mathbf{n} \equiv -\mathbf{n}$), the order parameter space, *i.e.* all possible realization of the director field, is the projective plane (P2). The charge N is calculated by considering the direction of $\mathbf{n}$ along the surface of a small volume that includes the entire defect. N is defined as the solid angle spanned by the director field on the P2 plane. Formally, the topological charge N is calculated by carrying out the integration [177]:

$$N = \frac{1}{4\pi} \int \int \left(\frac{d\theta}{du}\frac{d\phi}{dv} - \frac{d\phi}{du}\frac{d\theta}{dv} \right) \tag{3.5}$$

where we parameterize the director field as:

$$\mathbf{n} = \{sin\theta sin\phi, sin\theta cos\phi, cos\theta\} \tag{3.6}$$

In systems with the same topology, the total charge is conserved. Introducing a colloid with topological charge into a uniform director field, which has no defects and zero total charge, will require a companion defect with topological charge of opposite sign. The charge of the defect is related to the topology of the object. Two objects are topologically equivalent when one can be continuously transformed to the other. For example, a sphere has the same topology as an ellipsoid, a tetrahedron, a cube and a icosahedron. Euler characteristic, which is a parameter used to describe the topology of the object, is defined as

$$E = vertices + face - edges. \tag{3.7}$$

All of the objects mentioned above have Euler characteristic $E = 2$. Another way to define the topology is through the concept of genus. Genus is related to Euler characteristic in the following way:

$$E = 2(1 - g). \tag{3.8}$$

It is best understood as the number of holes an object has, but can be generalized into more complex geometries. Spheres, tetrahedrons, cubes, and icosahedrons all have $g = 0$. On the other hand, a donut or a washer shape both have $g = 1$.

With the concept of Euler characteristic, now we are ready to introduce the Gauss's Theorem, which applies to an object with homeotropic anchoring. Gauss's Theorem says that the total charge m_i within an object is equal to half of its Euler's characteristic E:

$$\sum m_i = E/2. \tag{3.9}$$

By introducing into this system a sphere with homeotropic anchoring, one essentially introduces a charge of $m_i = +2/2 = +1$ into the system originally free of defect, so a companion defect of charge -1 is required.

The companion defect can be in the form of a point defect, also called a hedgehog, or of a disclination line encircling the waist of the particle, also called a Saturn ring. These two configurations are topologically equivalent with charge -1 and, in some cases, the ring can shrink into a point. While the total topological charge of particle and associated defect is always zero, the energetics of hedgehogs and Saturn rings are very different. There are electrostatic analogies for these objects in the far-field. In the limit of small slopes and weak gradients in the director field, in the one elastic constant approximation ($K = K_1 = K_2 = K_3$) , the components of the director field obey Laplace's equation.

For a particle with planar anchoring, the topological charge of the object is given by the Poincaré Theorem. This theorem states that an object with director field that conforms to its surface introduces charges that sum up to

$$\sum m_i = E. \tag{3.10}$$

For spherical particles with planar anchoring, the most commonly observed configuration is the bipolar state, with two -1 defects, called "boojums" located at the two poles. The boojum colloids also behaves as quadrupoles and assemble in a zig-zag manner. Surface defects like boojums stay on the surface while Saturn rings and hedgehogs can move to a distance away and pin to objects in space.

The field of nematic colloids, in which particles interact in confined nematic liquid crystals, reveals rich interactions owing to elasticity and topological considerations absent for particles in isotropic fluids [160]. Interaction of nematic colloids with complex shapes have been summarized in recent reviews [178, 161, 162, 163, 164], which emphasize the importance of particle aspect ratio, curvature, corners, edges, topology (genus), among other features. For example, homeotropic particles of various shapes of genus zero, including spherocylinders [179], "cylinders" with edges of differing radii of curvature, and ellipsoids [180] form companion disclination lines that wrap the colloids in complex manners. On cylindrically shaped particles, the disclination lines interact preferentially with sharp edges, while on cubes, they avoid sharp corners to minimize the energy in the domain [181]. In the far field, pairs of particles with uniform anchoring interact with potentials that are analogous to electrostatic multipoles, with relevant elastic multipole interaction depending on particle shape [182]. Homeotropic particles with varying genus generate complex three-dimensional director fields and topological charge related to their genus via the Gauss-Bonnet theorem [183]. Grooved and helical shaped particles of genus zero have been studied as means of trapping energetically induced disclinations, not required by topology, that attract particles [184]. In the near field, particles can form complex structures with shared and knotted topological defects [185, 186]. Domain boundaries also influence interactions of colloids in NLC. The shape and anchoring energies of particles and domain boundaries can be designed to repel particles or to attract them to particular locations [187, 188, 189, 190, 191, 192, 176, 193, 194, 195]. From these and related studies, particle shapes, domain boundaries, and their anchoring conditions can be designed to exploit the NLC elastic energies in strategies for reconfigurable assembly. These elastic interactions do not rely on the particle's material properties, but rather on particle shape, surface chemistry and confinement.

3.2. Materials and Methods

3.2.1. Fabrication of ferromagnetic disk colloids and assembly of nematic liquid crystal (NLC) cell

Circular disk colloids of diameter $2a$=75 µm and thickness h=25 µm were fabricated out of SU-8 photoresist following standard lithographic processes on a supporting wafer. Thereafter, a layer of nickel was sputtered onto the surface using a Lesker PVD75 DC/RF

Sputterer to make the colloids ferromagnetic. Subsequently, treatment with 3 wt% solution of N-dimethyl-n-octadecyl-3-aminopropyl-trimethoxysilyl chloride (DMOAP) imposed homeotropic anchoring condition on the disk's Ni coated surfaces. The treated disk colloids were then released from the wafer and dispersed in 4-cyano-4'-pentylbiphenyl (5CB). Glass slides were spin-coated with polyimide (PI-2555) and rubbed with a velvet cloth along the desired direction to impose uniform planar anchoring. Two glass slides with uniform planar anchoring were assembled in an antiparallel fashion and glued together using a UV sensitive epoxy with two layers of $\sim 15\,\mu\text{m}$ plastic spacers in between. The resulting thickness of the cell was $\sim 50\,\mu\text{m}$. Finally, a suspension of disk colloids in 5CB was introduced into the cell by capillarity in the isotropic state of 5CB. Depending on the thickness of the nickel layer, the coated disk could either appear transparent (a thin layer of nickel) or black (a thick nickel coating). While the transparent disk allowed us to visualize the swim stroke across the surface of the disk, colloids with thicker coating possess stronger magnetic moments, enabling faster rates of rotation.

3.2.2. Controlled rotation of disk colloids

To rotate the magnetic disk colloids, the assembled NLC cell was placed in a rotating magnetic field generated by a custom-built magnetic control system. The system consists of two orthogonal pairs of electromagnetic coils (APW Company) mounted on an aluminum supporting structure arranged around the workspace. Visual feedback is provided by a CCD camera (Point Grey Grasshopper3 Monochrome) mounted on a Zeiss inverted microscope (ZEISS Axio Vert.A1). Each coil pair was powered independently using a programmable power supply (XG 850W, Sorensen) whose outputs were controlled by a Python algorithm written in house. Sinusoidal time-dependent voltages are applied on each pair and the waveforms are separated by a $\pi/2$ phase lag in order to achieve a rotating field whose periods varied from 4 s to 1200 s for this study.

3.2.3. Characterization of static dipolar defect using fluorescent confocal polarizing microscopy (FCPM)

The configuration and location of the defect in a dipolar configuration around a disk colloid along the vertical z-axis was determined by FCPM [196]. The NLC, 5CB, was doped with an anisotropic dye N,N‘-Bis(2,5-di-tert-butylphenyl)-3,4,9,10-preylenedicarboximide (BTBP; Sigma–Aldrich) at 0.01 wt%. At such low concentration, dye molecules co-align with the NLC molecules while preserving the properties of 5CB and fluoresce when aligned parallel to the polarization direction of the excitation light. FCPM images of the disk colloid with a dipolar defect in a planar NLC cell (Fig. 3.6) were obtained using an inverted IX81 Olympus microscope equipped with a FV300 Olympus confocal scan box. A polarizer was placed between the sample and the objective to rotate the polarization of the scanning laser. As shown in Fig. 3.6, a dipolar defect forms on top of the disk aligned with the far-field director. In addition, FCMP scanning along the z-axis and the cross section of the yz plane (Fig. 3.6b) indicates that this dipolar defect is in the form of a disclination loop anchored on the top and bottom edge of the disk, and the cross-sectional area of the domain containing the loop is changing along the z-axis. This configuration is in agreement with the results from numerical simulations shown in Fig. 3.2c.

3.2.4. Characterization of surface roughness of the disk colloids using atomic force microscopy (AFM)

The surface roughness of the top and side surfaces of the disk colloid after Ni deposition was characterized using a Bruker Icon AFM in standard tapping mode. For the flat surface, the colloid’s surface roughness was measured while still attached to a silicon substrate. Characterization of a 10 µm by 10 µm area gave a root-mean-square roughness R_q=3.29 nm with a peak value of 107 nm, indicating that the top surface is nanoscopically smooth with a few isolated rough sites in the hundred nanometer range as shown in Figs. 3.9(a) and 3.9(b). The roughness of the side surface was obtained by placing the disk on its side, adhered to a planar support. The root-mean-square roughness R_q of a 3 µm by 3 µm scanning area (Figs. 3.9(c) and 3.9(d)) was 19.4 nm with a peak value of 213 nm. The side surface has greater roughness than the top surface. We attribute such surface roughness to non-uniform Ni deposition and typical resolutions achieved in 2D UV photolithography. These rough sides may facilitate the pinning of the disclination line. It is interesting to note that the roughness on the sides and edges are similar in size to the defect core $\sim 10\,\mathrm{nm}$.

3.2.5. Rotation of disk colloids in the isotropic phase of 5CB

To examine the importance of NLC elasticity in the observed translation of the rotated disk, the same colloids were rotated in the isotropic phase of 5CB. A planar cell filled with the disk colloid suspension was sealed on all sides using epoxy resin and submerged in a hot water bath with temperature higher than the phase transition temperature of 5CB. The 5CB in the sealed cell was melted into the isotropic state, and the water bath ensured that any possible drift from temperature gradients was minimized. An external field was applied to rotate the disk in the isotropic phase of 5CB. In comparison to disks rotated in the nematic phase, the translational velocity was attenuated by more than an order of magnitude. For example, the apparent velocities of disk colloids rotating in isotropic and nematic phase of 5CB are $0.025\,\mathrm{\mu m\,s^{-1}}$ and $0.94\,\mathrm{\mu m\,s^{-1}}$ respectively under the same external field with period $T = 20\,\mathrm{s}$. Notably, the velocity is decreased even though the viscosity is reduced; the viscosity of 5CB decreases with temperature and is lower in the isotropic phase than in the nematic phase.

3.2.6. Controlled rotation of spherical colloids in the nematic phase of 5CB

To demonstrate the importance of defect line pinning in the observed translation, $2a{=}8.74\,\mathrm{\mu m}$ ferromagnetic spherical colloids (Spherotech, Inc.) were treated with DMOAP to impose homeotropic anchoring on the surface before being dispersed in 5CB. The colloidal suspension was introduced into a planar cell of thickness $H \sim 30\,\mathrm{\mu m}$, and the cell was placed under an external rotating magnetic field with period $T = 6\,\mathrm{s}$. Spherical colloids rotated with the field with their hedgehog defect oscillating around the initial equilibrium. During this process, no translation was observed. Notably, the defect in this example was not pinned and did not stretch as the colloid rotated. Rather, the companion defect moved freely above the colloid.

3.2.7. Numerical simulations

The numerical simultaions in this chapter are performed in collaboration with Dr. Žiga Kos and Professor Miha Ravnik using a Q-tensor order parameter description of nematodynamics. The director field $\vec{n}$ is obtained as a main eigenvector of the Q-tensor and the degree of order S as its main eigenvalue. Equilibrium structures correspond to a minimum of the free energy

$$\begin{aligned} F = &\int_{\text{bulk}} \mathrm{d}V \left[\frac{A}{2}Q_{ij}Q_{ji} + \frac{B}{3}Q_{ij}Q_{jk}Q_{ki} + \frac{C}{4}\left(Q_{ij}Q_{ji}\right)^2 + \frac{L}{2}(\partial_k Q_{ij})(\partial_k Q_{ij})\right] \\ &+ \int_{\text{disk bottom surf.}} \mathrm{d}S\, W\left(\tilde{Q}_{ij} - \tilde{Q}_{ij}^{\perp}\right)^2, \end{aligned} \tag{3.11}$$

which is calculated from the bulk and the surface contributions. A, B, and C are nematic phase parameters and dictate the degree of order in the equilibrium homogeneous director field S_{eq}. L is the tensorial elastic constant and is directly proportional to the director elastic constant K. The surface integral is performed only over the disk bottom surface, where the anchoring of nematic molecules is planar degenerate. The director field is fixed on the disk side-walls, disk's top surface and the cell's top and bottom boundaries. The planar-degenerate surface is modeled by a Fournier-Galatola potential, where $\tilde{Q}_{ij} = Q_{ij} + \frac{S_{\text{eq}}}{2}\delta_{ij}$, $\tilde{Q}_{ij}^{\perp} = (\delta_{ik} - \nu_i\nu_k)\tilde{Q}_{kl}(\delta_{lj} - \nu_l\nu_j)$, and $\vec{\nu}$ is the surface normal.

Q-tensor dynamics is described by the Beris-Edwards model [197, 198]

$$\dot{Q}_{ij} = \Gamma H_{ij} + S_{ij}, \tag{3.12}$$

where H_{ij} is the molecular field driving the nematic orientation towards a free energy minimum

$$H_{ij} = -\frac{1}{2}\left(\frac{\delta F}{\delta Q_{ij}} + \frac{\delta F}{\delta Q_{ji}}\right) + \frac{1}{3}\frac{\delta F}{\delta Q_{kk}}\delta_{ij} \tag{3.13}$$

and Γ is the rotational viscosity parameter. S_{ij} describes the nematic response to flow gradients

$$S_{ij} = (\zeta A_{ik} - \Omega_{ik})\left(Q_{kj} - \frac{\delta_{kj}}{3}\right) + \left(Q_{ik} - \frac{\delta_{ik}}{3}\right)(\zeta A_{kj} - \Omega_{kj}) - 2\zeta\left(Q_{ij} + \frac{\delta_{ij}}{3}\right)Q_{kl}\partial_l v_k, \tag{3.14}$$

where $\vec{v}$ is the flow field, $A_{ij} = (\partial_i v_j + \partial_j v_i)/2$, $\Omega_{ij} = (\partial_i v_j - \partial_j v_i)/2$, and ζ is the nematic alignment parameter. On the planar degenerate surface, the Q-tensor follows the dynamics of

$$\dot{Q}_{ij}^{\text{surf}} = \Gamma_{\text{surf}}\left[\frac{1}{2}(H_{ij}^{\text{surf}} + H_{ji}^{\text{surf}}) - \frac{1}{3}\delta_{ij}H_{kk}^{\text{surf}}\right] \tag{3.15}$$

where Γ_{surf} is the surface rotational viscosity parameter, and

$$H_{ij}^{\text{surf}} = -\frac{\partial f_{\text{vol}}}{\partial(\partial_k Q_{ij})}\nu_k - \frac{\partial f_{\text{surf}}}{\partial Q_{ij}}, \tag{3.16}$$

is the surface molecular field, calculated from the bulk and surface free energy density given by Eq. 3.11. Simulations of where the disk does not rotate were solved using an approximation of no flow. For simulations with rotating disk, the flow field was calculated by a lattice Boltzmann method with a moving boundary condition, and the resulting stationary flow field was used in Eq. 3.12.

Simulations were performed using a finite difference method to solve Eq. 3.12. The simulation in Fig. 3.5 was obtained on a 580 × 580 × 140 mesh size with disk radius $a = 105\,\Delta x$ and disk height $h = 70\,\Delta x$ (Δx is the mesh resolution), while other simulations were performed on a 380 × 380 × 280 mesh with $a = 95\,\Delta x$ and $h = 140\,\Delta x$. A plane with a no-slip velocity boundary condition and a fixed planar director field is used at the top and at the bottom of the simulation box. Periodic boundary conditions are used in the lateral directions of the numerical simulation box. Mesh resolution is set as $\Delta x = 1.5\xi_{\text{N}} = 1.5\sqrt{L/(A + BS_{\text{eq}} + \frac{9}{2}CS_{\text{eq}}^2)}$, where ξ_{N} is the nematic correlation length that sets the size of the defect cores. The following values of the model parameters are used: $\zeta = 1$, $B/A = 12.3$, $C/A = -10.1$, $W = 0.5\,L/\Delta x$, $\Gamma_{\text{surf}} = \Gamma/\Delta x$ (unless otherwise specified), and a timestep of $0.1(\Delta x)^2/(\Gamma L)$. The results of the simulations are expressed using the mesh resolution Δx, rotational viscosity parameter Γ, and elastic constant L.

3.3. Results and Discussion

3.3.1. Static defects around the disk colloid and its non-equilibrium rotational dynamics

When introduced into the NLC-filled planar cell, a defect forms on the colloid with two disclination lines that connect the top and bottom faces of the disk, assuming a quadrupolar configuration (Figure 3.4). If the disk is perturbed, the defect transforms irreversibly to a static dipolar configuration that features a single loop on one side of the disk (Fig. 3.2b). Numerical simulation (Fig. 3.2c) reveals that this defect is a disclination loop anchored on two locations on the degenerate planar face and extends along the side of the disk toward the homeotropic face. Fluorescence confocal polarizing microscopy corroborates the dipolar arrangement of this disclination loop as shown in Fig. 3.6.

Using the numerical method outlined above, we performed numerical simulations testing the stability and dynamics of dipolar and quadrupolar nematic solutions around a disk particle. In Figure 3.4, we test how different director profiles on the disk's side-wall affect the dipolar solution. Higher disk aspect ratios compared to experiments are used to promote the stability of the dipolar structure, since it is known that the stability of a dipolar solution is increased for large colloidal particles compared to the nematic correlation length [160]. Since particle size is limited in simulations due to computational constraints, the dipolar solution is only metastable for specific side-wall director profiles. When the director field on the side wall is taken to be completely perpendicular to the surface, the dipolar solution is unstable and, in time, transforms into a quadrupolar field (Fig. 3.5).

When the disk is rotated in a continuous manner, the defect undergoes a complex periodic rearrangement (Fig. 3.2d) that propels the disk. The disclination line initially stretches while remaining pinned on the disk's sharp edge, storing elastic energy in the form of effective line tension of the defect core as well as elastic distortion of the NLC director field that deviates from equilibrium. These effects combined with material flow generate complex torques that cause the disk to precess, with its projected area oscillating twice in each period (Fig. 3.2e). When the stored energy is high enough to depin the defect, the disclination line contracts by sweeping across the disk's face and returns to its initial configuration. As this occurs, the disk's tilt is reduced. The disk subsequently flattens and weakly tilts again as the defect re-forms its dipolar configuration. This swimming stroke propels the disk nearly perpendicular to the far field director in an external field at low rotation rates (T=40 second in Fig. 3.2f). In each period, roughly half of the displacement occurs as the defect sweeps across the disk's face, as indicated by the red region in Fig. 3.2e.

3.3.2. Swimming behaviors and trajectory planning

The behavior of the defect propelled nematic swimmers can be characterized in terms of the dimensionless Ericksen number which measures the ratio between viscous and nematoelastic stresses; $Er = \frac{\gamma\omega a^2}{K}$, where γ is the rotational viscosity, a is the disk radius, K is the elastic constant and ω is determined by the period of the rotating field $\omega = \frac{2\pi}{T}$. We observe particle swimming at different Er, showing that the propulsion is affected by both the nematic elasticity and flow. The swimmer moves with Reynolds number $Re = \frac{\rho\omega a^2}{\gamma} \sim 10^{-6}$ to 10^{-5}, where ρ is the density of 5CB. The scallop theorem dictates that non-symmetric strokes are required to swim in Newtonian fluids in creeping flow. Similarly, in the limit of small Er, non-symmetric defect line motion is required to achieve motion in NLC.

A detailed examination of disk displacement and speed (Fig. 3.2e and Fig. 3.7) over the course of the periodic defect motion indicates that translation is strongly coupled to the sweeping motion of the disclination line and the tilting motion of the disk. For slow rotation (small Er), the velocity v is linear in ω (Fig. 3.11a) and is directed along an angle $\phi \sim 90°$ (Fig. 3.11b). The defect polarity and the disk's sense of rotation together determine the swimming direction which can be reversed by changing the disk's sense of rotation. This control of swimming direction is akin to a flagellum, which can generate "pusher" or "puller" motions. As ω increases (finite Er), v deviates from the linear relationship, attaining velocities in excess of $2\,\mu\mathrm{m\,s^{-1}}$ for the highest frequencies probed. Moreover, the translation direction, as characterized by the angle ϕ in Fig. 3.11b, decreases logarithmically with Er. This more complex dependence of ϕ on Er allows additional control over swimming direction; a disk colloid with given defect polarity can explore a half space by simply tuning the sense of rotation and frequency of the external field. For example, in Fig. 3.11c, two disks with opposite defect polarity move in opposite directions under the same sense of rotation. However, when their sense of rotation is reversed, rather than simply reversing their translation direction, they turn along angles that depend upon Er, executing V-shaped trajectories. Furthermore, the defect-propelled colloid can follow a curved path by tuning Er as shown in Fig. 3.11d.

3.3.3. Derivation and scaling analysis on the propulsion mechanisms

Disk propulsion is linked to the anisotropic order within the nematic liquid crystal. In this section, we discuss the relevant mechanisms of propulsion and their scaling with the disk size, viscoelastic properties of the nematic, and disk rotation frequency. The propulsion mechanisms below are roughly on the same order of magnitude and likely all contribute to the final speed of propulsion. This is not surprising, as all of the mechanisms are due to pushing the nematic configuration out of equilibrium.

Elastic forces

In a nematic medium, elastic stress is exerted on confined objects, which is described by the Ericksen stress tensor [198]. The elastic stress aims to displace the objects in order to minimize the nematic elastic free energy. If we assume that the length scale of the director distortion is of the order of disk radius a, the Ericksen stress tensor scales as $\sigma_{\mathrm{Er}} \sim K/a^2$, where K is the nematic elastic constant. The propulsion force is calculated by integrating the Ericksen stress over the disk surface, which scales as $4\pi a^2$, assuming that the disk thickness is of similar size as the radius. The obtained scaling for the propulsion force is therefore of the order of the elastic constant $F_{\mathrm{prop}} \sim K$.

Another approach towards estimating the elastic forces on the disk is through the concept of defect line tension. Geometric frustration due to rotation of a disk particle with a hybrid anchoring pattern generates a periodic reshaping of a pinned defect line. During this periodic swimming stroke, the pinned defect line pulls on the colloidal particle and they collectively propel across the nematic liquid crystal. A defect line pinned to the disk surfaces acts upon it with a force of $\pi K/4 \log(a/a_{\text{core}})$ [198], where we have again used the radius a as a measure of the length scale and a_{core} is the size of defect line cores (for 5CB a_{core} is of the order of a few nm). As the logarithmic factor changes very slowly with a and the obtained result for the experimental radius is similar in magnitude to the F_{prop} above, we shall use the scaling of $F_{\text{prop}} \sim K$ in our analysis. Furthermore, in equilibrium, the elastic forces cancel themselves out, and there is no net force on the disk. The above scaling of the propulsion force is valid at disk's high rotation rates, where the nematic field is far from equilibrium.

From the propulsion force F_{prop}, we can write the translation velocity

$$v_{\text{translation}} = \frac{F_{\text{prop}}}{c_d\, \eta\, a} \sim \frac{4\pi K}{c_d\, \eta\, a}, \tag{3.17}$$

where c_d is the linear drag coefficient for the disk and η is the effective viscosity of 5CB, calculated as an average of Miesowicz viscosities. For a disk translating in a confined environment between two parallel plates, the drag coefficient is estimated from lubrication theory as $c_d \sim c_{d,bottom} + c_{d,top} \sim \frac{4a}{h_0} + \frac{4a}{h_1}$, where h_0 and h_1 are the gap thickness between the disk surface and the bottom plate and the top plate, respectively. For a typical cell we used in the experiment, FCPM reveals that $h_0 \sim \frac{1}{2}h_1 \sim 8.6\,\mu\text{m}$. By defining a dimensionless parameter $\varepsilon = \frac{h_0}{2a}$, a drag coefficient $c_d = \frac{3}{\varepsilon}$ will be used for further analysis. For the relevant parameter values of $K = 6.5\,\text{pN}$ [198], $a = 37.5\,\mu\text{m}$, $\eta = 0.064\,\text{Pa s}$ [198], we obtain the value of translational velocity of $v_{\text{translation}} \sim 1.3\,\mu\text{m}\,\text{s}^{-1}$, which is of similar order of magnitude as the experimental results at high frequency of disk rotation.

Hydrodynamic force due to squeezing flow

During the defect rearrangement process, the disk periodically tilts and flattens as the disclination line elongates and sweeps across the disk surface. This squeezing flow results in a hydrodynamic force in the thin gaps between the disk and the bounding plates. On one side of the disk, where the defect performing the swimming stroke is absent, the disk does not experience a net force due to the scallop theorem since the tilting and flattening are completely reversible. However, the defect sweeps over the other side of the disk, causing it to tilt, and is absent during the flattening process. This viscosity difference avoids the constraints of the scallop theorem, and results in a net hydrodynamic force on the disk. To estimate the propulsion velocity from this force, we assume the viscosities of the fluid in the thin gap when the disclination line is present and absent are $\eta_{1,gap}$ and $\eta_{2,gap}$, respectively. Under thin-film approximation, the net hydrodynamic force in the horizontal direction due to the squeezing flow as the disk tilts and flattens is $F_x \sim \frac{4a^2\omega\Delta\eta_{gap}}{\alpha^2} \sim \frac{4a^2\Delta\eta_{gap}}{\alpha T}$, where $\Delta\eta_{gap} = \eta_{1,gap} - \eta_{2,gap}$, α is the tilting angle with respect to the horizontal direction and T is the period of the process. This force is balanced by a drag force along the x direction $F_D \sim c_d \eta a v_{\text{translation}}$. Equating F_x and F_D gives the translational velocity of the disk

$$v_{\text{translation}} \sim \frac{\Delta\eta_{gap}}{\eta}\frac{4a}{c_d \alpha T}. \tag{3.18}$$

Using typical experimental values for T=40 s, $v \sim 1.12\frac{\Delta\eta_{gap}}{\eta}$ µm s^{-1}; taking $\frac{\Delta\eta_{gap}}{\eta} \approx 0.01 - 1$ for thermotropic nematics [89], this predicts a velocity range $\sim 0.01 - 1.12$ µm s^{-1} which contains observed average velocities of 0.55 µm s^{-1} at T=40 s.

Nonhomogeneous viscosity on either side of the colloid

As the disk rotates in the nematic fluid, it experiences a viscous force that is dependent on the structure of the nematic field. The side of the disk with the nematic defect present is in a region of different (and in principle lower) effective viscosity than the opposite side of the disk. Such a difference in viscosities can explain the propulsion of spinning disks in the direction that is observed in experiments (Fig. 1). To estimate the magnitude of propulsion velocity due to different viscosity regions, we assume that the effective viscosity on one side of the disk equals $\eta_{1,side}$ and on the other side $\eta_{2,side}$. The shear at the disk side-wall is estimated to $v_{\text{side-wall}}/a = \omega$. The shear force density on the side-wall therefore equals $\mathrm{d}F_1/\mathrm{d}S = \eta_{1,side}\omega$ in the region of $\eta_{1,side}$. Integrating over $\mathrm{d}S = ah\,\mathrm{d}\phi$, where h

is the disk thickness, we obtain $F_1 = \int_0^\pi \mathrm{d}\phi \, ah\,\omega\eta_1 \sin\phi = 2ah\omega\eta_{1,side}$. The $\sin\phi$ term is included as we are interested only in one component of the force. The net force on the disk can be written as $F_{\text{prop}} \sim F_1 - F_2 = 2ah\omega\Delta\eta_{side}$, where $\Delta\eta_{side} = \eta_{1,side} - \eta_{2.side}$. The net force generates a disk translational velocity of

$$v_{\text{translation}} \sim \frac{2h\omega\Delta\eta_{side}}{c_d\,\eta}. \tag{3.19}$$

Using the same parameters as for Eq. 3.17, disk thickness $h = 25\,\mu\mathrm{m}$, experimental rotational velocity from Fig. 2 of $\omega = 1.0\,\mathrm{s}^{-1}$, and range of viscous anisotropy $\frac{\Delta\eta_{side}}{\eta}$ mentioned above, we obtain the approximate value for the translational velocity of $v_{\text{translation}}$ in the range $\sim 0.02 - 2\mu ms^{-1}$ which is similar in magnitude to the other propulsion mechanisms.

The elongation and subsequent instability of the disclination line along the rotating disk's edge, captured in simulation (Fig. 3.8), plays a prominent role in the swimming phenomenon; edge roughness may also play a role (Fig. 3.9). Elasticity, broken symmetry and disclination line pinning are essential to the observed swimming mechanism. Disks rotated in 5CB in the isotropic phase fail to translate, and no translation was observed in experiments performed with homeotropic spherical colloids in which disclination line pinning was absent. Furthermore, rotated disks with quadrupolar defects exhibit periodic disclination line pinning and release (Fig. 3.10) but also fail to translate.

3.3.4. Dynamics pair interaction

Finally, we demonstrate pair interaction between two swimmers. Colloids at rest with opposite polarity self-assemble in a zig-zag manner (Fig. 3.12a) similar to their spherical counterparts with homeotropic anchoring [199]. Swimming introduces dynamic interactions; swimmers of opposite polarity always dimerize with the stability of the dynamic dimer depending strongly on Er as shown in Figs. 3.12b and 3.12c. At $Er \sim 0.92$, the two swimmers co-rotate as a dimer for a short period of time, separate and move away from each other (first row in Fig. 3.12c). For faster rotation ($Er \sim 1.83$), the swimmers reform a bonded dimer after a small gap is created during the co-rotation (second row in

Fig. 3.12c). Further increasing Er leads to stable dimer co-rotation as shown in the bottom row of in Fig. 3.12c. We hypothesize that such distinct dynamic interactions result from the interplay of repulsive interaction between unmatched boundaries and attractive defect-defect interactions which strongly depends on the Er of the rotation; defects become long enough to entangle and merge above a threshold Er, cementing dimers in configurations that determine their broken symmetry and swimming behavior. Dimers of opposite polarity are nearly antisymmetric and rotate without significant translation. For example, an individual colloid swims at an average velocity of $0.55\,\mu\mathrm{m\,s^{-1}}$ while a dimer translates at $0.031\,\mu\mathrm{m\,s^{-1}}$ under the same field of T=40 s. For disks of similar polarity, dimer formation also depends on defect elongation and topology. Disks with distinct, separate elongated defects co-migrate in the same direction without forming a dimer (MovieS12 in SM). However, above some threshold, the defects of the two disks merge to form a complex shared structure with enhanced broken symmetry; the dimers rotate and translate, as shown in Fig. 3.12d, with a speed of $2.07\,\mu\mathrm{m\,s^{-1}}$, similar to that of an individual swimmer.

3.4. Conclusions

In this chapter, we introduce topological defect-propelled swimming of nematic colloids. We develop rotating magnetic disk colloids with complex, elongated defects which perform a 'swim stroke' that drives their translation. Geometric frustration dominates for small rotation rates, and the colloid's speed is linear in Er. At faster rotation rates, significant defect elongation and local changes in viscosity allow the swimming direction to be tuned for path planning. These defect-propelled swimmers exhibit far-from-equilibrium pair interactions that differ significantly from their static dipolar counterparts.

Defect-propelled swimming of nematic colloids opens opportunities for soft materials manipulation and unveils exciting questions. For example, our disks have sharp edges and hybrid anchoring conditions which generate defects that are not clearly defined by the Poincaré-Hopf or Gauss-Bonnet theorem that relates uniform anchoring to required topological charge [200, 181]. Under quasistatic rotation, the defect elongates along the disk's

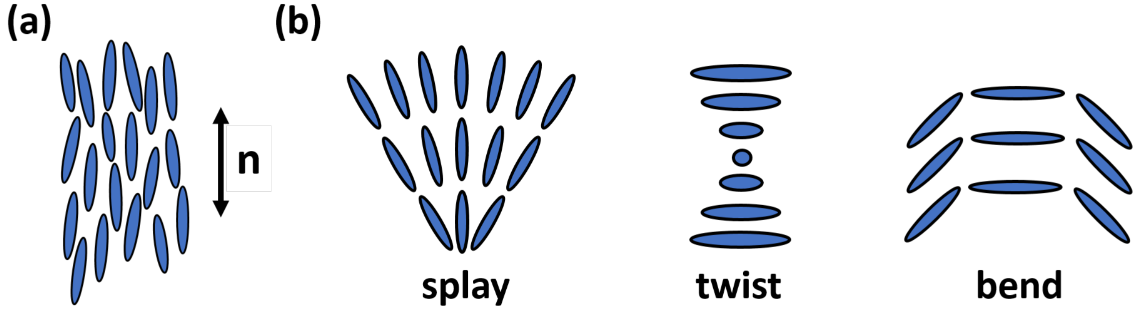

Figure 3.1: (a) The nematic liquid crystalline phase whose long range order is dictated by the director $\mathbf{n}$. (b) Three main types of distortions in liquid crystals: splay, twist and bend.

edge and subsequently depins from the edge; the physics that regulate these transitions and their relationship to colloid geometry are unexplored. Under finite Er rotation, the dipolar defect elongates in the flow field by a dynamic instability. Our colloids also form shared, dynamically changing defects that merge and separate, subject to topological transitions whose rules are far from evident. Finally, we have reported dynamic dipolar interactions for nematic colloids, introducing a spinner colloid with significantly rate-dependent interactions. Future work will address dynamics of systems of many swimmers to probe collective phenomena including the formation of reconfigurable motile structure [201, 6, 202], front propagation and stability [203, 6].

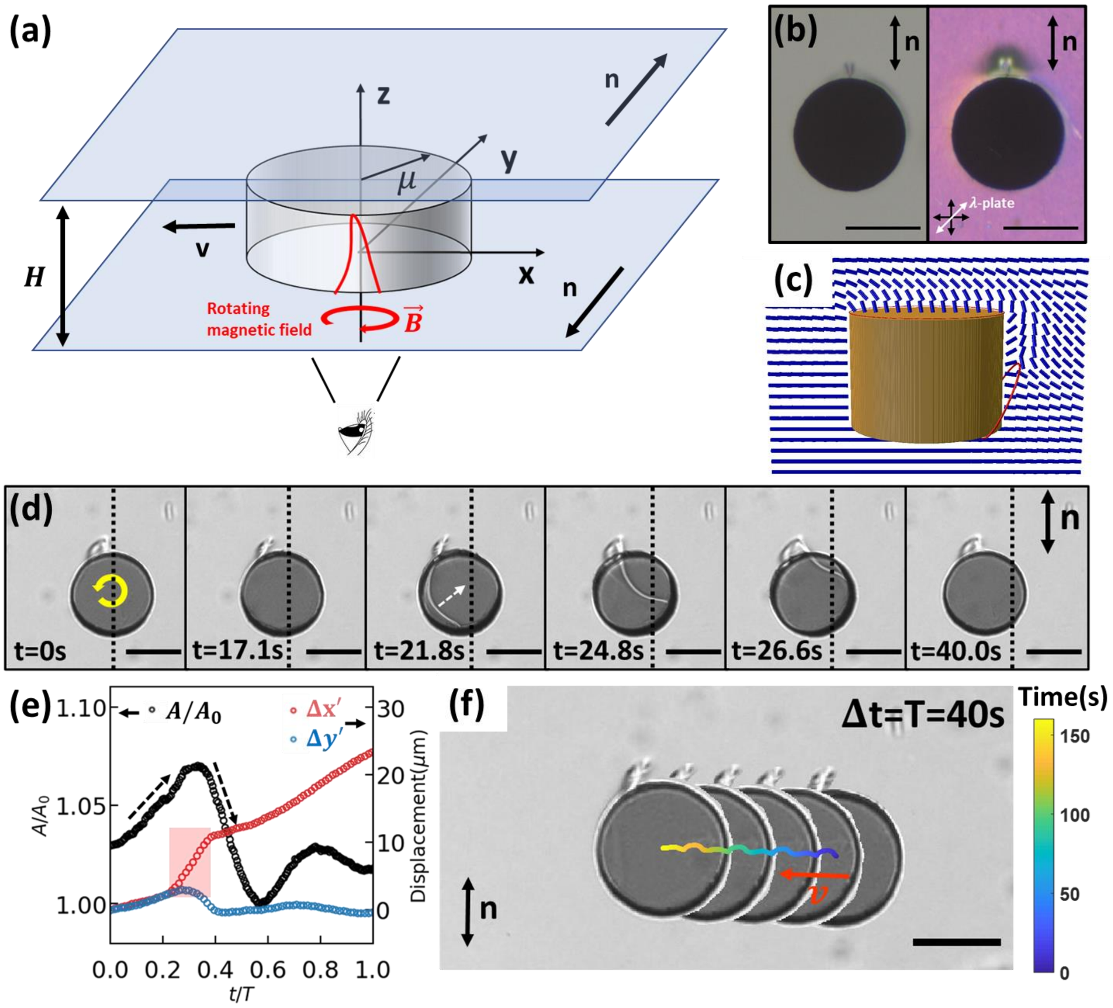

Figure 3.2: Far-from-equilibrium topological defect acts as a flagellum to propel nematic colloids: (a) Scheme of experimental setup showing a magnetic disk of $2a$=75 µm and thickness h=25 µm sandwiched between two glass slides separated by a distance $H \sim 50$ µm with antiparallel uniform planar anchoring. (b) Static dipolar defect configuration under bright field (left) and cross-polarization microscopy with a lambda plate (right). (c) Numerical simulation of the static dipolar configuration. (d) Time-stamped images of the swimming stroke of a disk colloid under a rotating field with period T=40 s. The dashed line indicates the initial position of the center, and the white arrow indicates the direction of the swimming stroke. (e) Normalized projected area A/A_0 (black circles, left axis) and displacement (right axis) parallel (red circles) and perpendicular (blue circles) to the translation direction within one period as shown in (d). The dashed arrows indicate the tilting and flattening of the disk and the red region indicates the sweeping motion of the disclination line across the surface. The sense of rotation observed from below corresponds to clockwise rotation in (a). (f) Equal time step (Δt=T=40 s) image showing swimming trajectory (colored curve) of the disk within 160 s. The red arrow indicates the velocity of the disk. Scale bars: 50 µm.

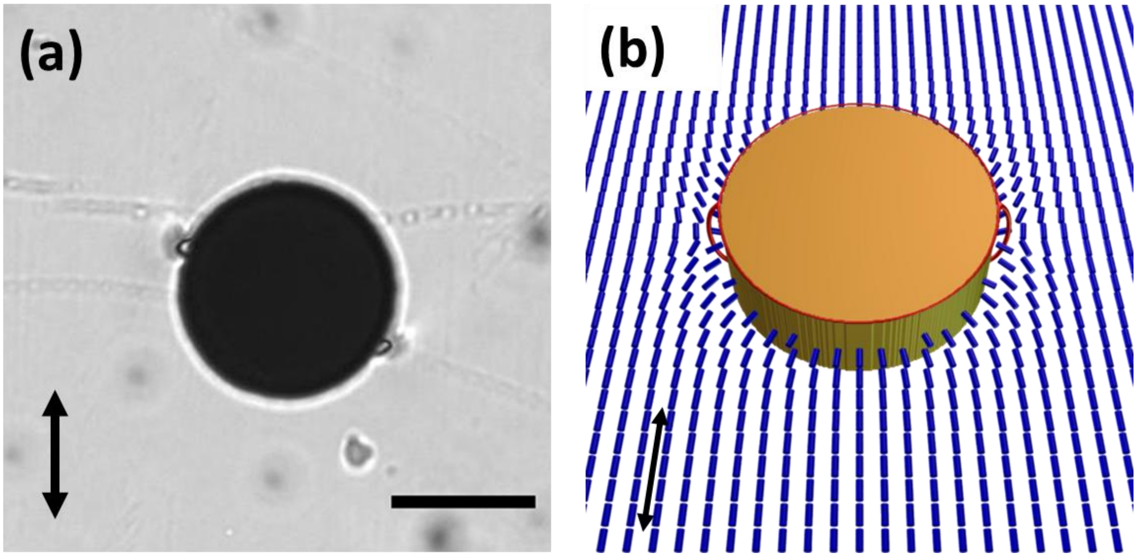

Figure 3.3: Microscopic image (a) and numerical simulation (b) showing the quadrupolar defect configuration around a disk colloid. The double-headed arrows indicate the far-field director. Scale bar is 50 µm.

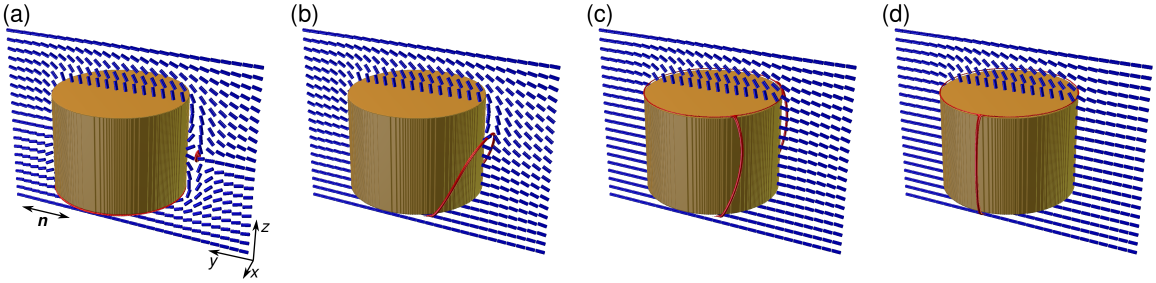

Figure 3.4: Defect configurations in numerical simulations. Depending on the boundary condition on the disk surface, nematic configuration in simulations can show various dipolar or quadrupolar solutions. In all panels, the disk bottom surface is perfectly planar degenerate and the top surface is homeotropic. The disk is positioned in a cell with the director orientation along y axis on the top and the bottom plane. (a) On the side-wall of the disk a splay-like director field is fixed, going from $-z$ to $+z$ orientation between the bottom and the top surface. Such a boundary condition stabilizes a point defect in the form of a small loop along the director far-field axis. (b) If the splay-like boundary condition is enforced only on the top half of the disk's side-wall, a defect line is the stable dipolar configuration. The defect line is pinned at two points to the bottom edge of the disk, and its cross-section shows a half-integer profile. (c) If the boundary condition on the whole side-wall is homeotropic, the nematic field evolves from the initial dipolar ansatz into a solution with two defect lines, each pinned to the top and the bottom edge. This dipolar solution is unstable and in time evolves into the quadrupolar field (d). The time evolution from dipolar to the quadrupolar field is shown in Fig. 3.5.

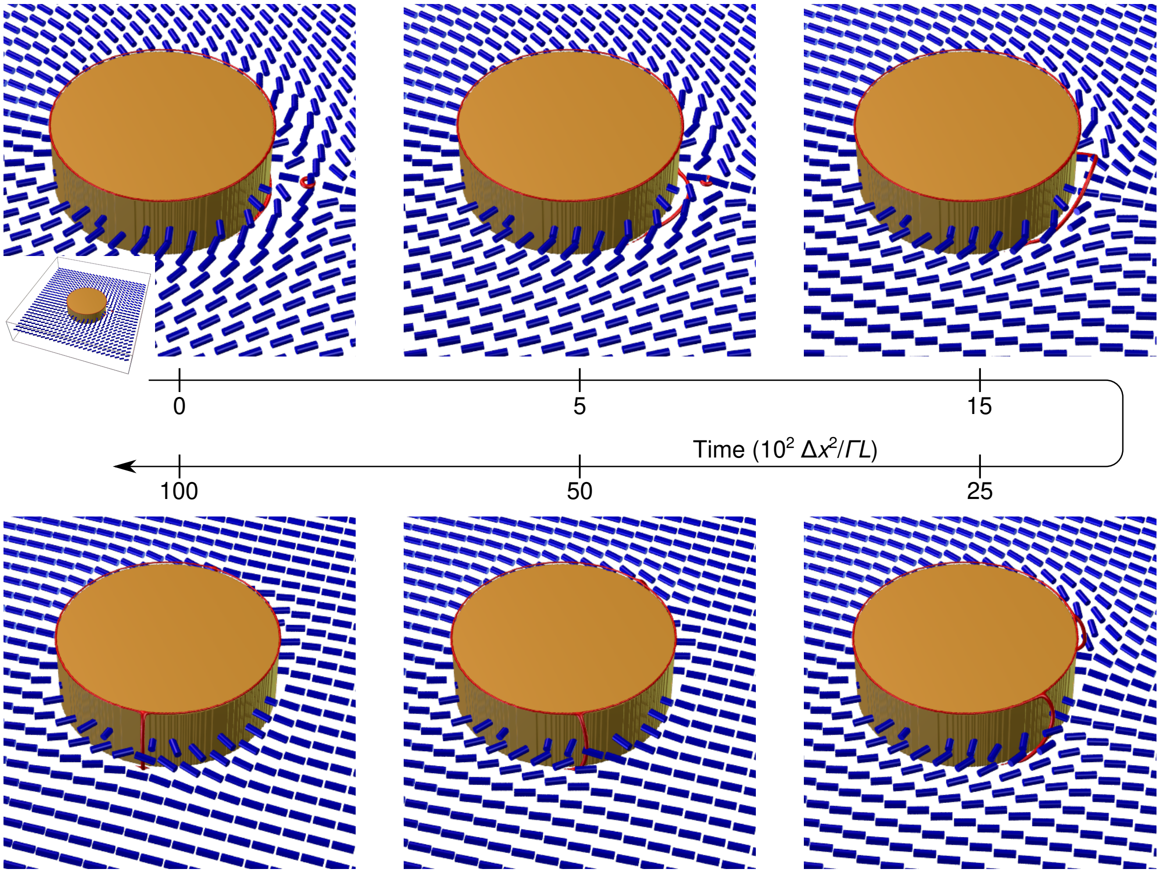

Figure 3.5: Time evolution from the dipolar to the quadrupolar configuration. The initial configuration is a dipolar director field with a point defect not in contact with the disk surface. Inset shows the disk position and dimension inside the numerical simulation box. In time, the point defect comes in close proximity to the defect line protruding from the disk bottom edge ($t = 500\,\Delta x^2/\Gamma\text{Ł}$), and eventually they merge ($t = 1500\,\Delta x^2/\Gamma\text{Ł}$). The newly formed defect line then gets pinned to the top edge ($t = 2500\,\Delta x^2/\Gamma\text{Ł}$), forming two line segments that gradually move away from each other, leading to a stable quadrupolar director field configuration.

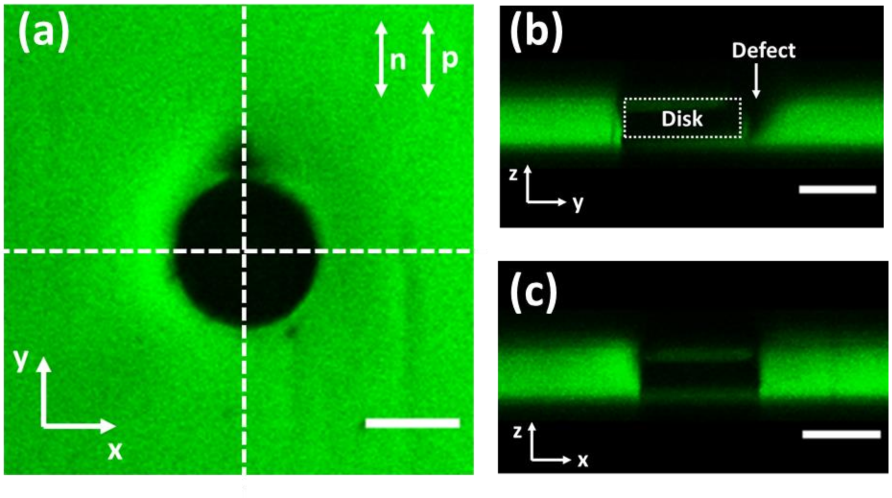

Figure 3.6: Fluorescent confocal polarizing microscopy (FCPM) images of a disk colloid with dipolar defect shown in (a) xy-plane, (b) yz-plane and (c) xz-plane. Scale bars are 50 µm.

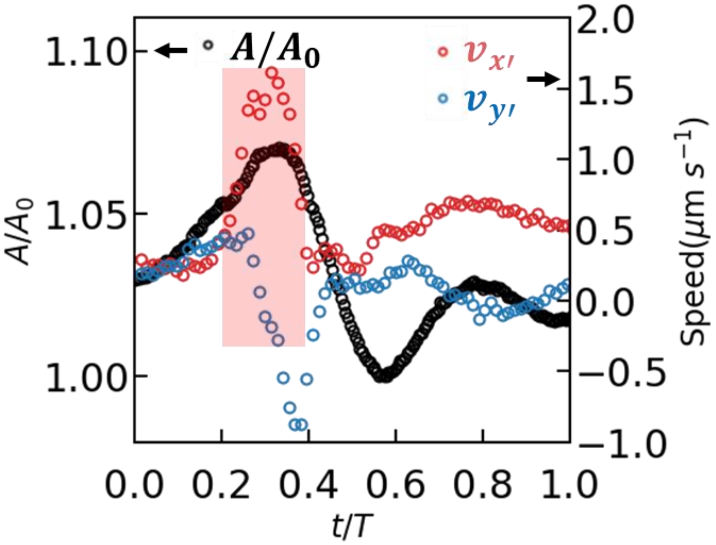

Figure 3.7: Speed variation within one period: Normalized projected area A/A_0 (black circles, left axis) and swimming speed (right axis) parallel (red circles) and perpendicular (blue circles) to the translation direction within one period corresponding to Fig. 1(e) in the main text.

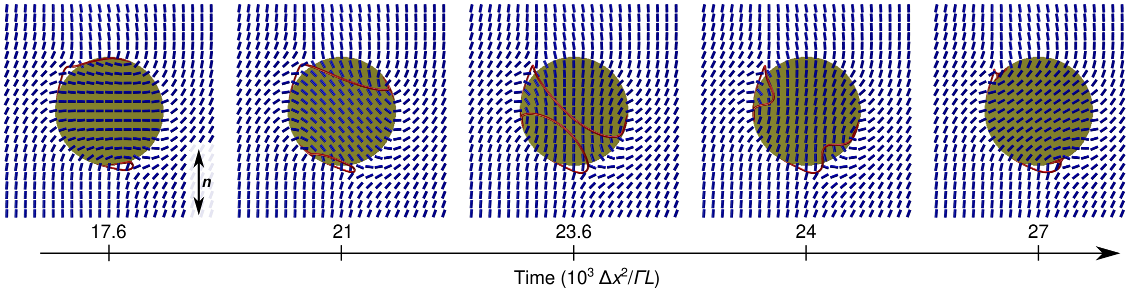

Figure 3.8: Defect sweeping motion in simulation. The timeline shows a period of defect motion as seen in MovieS15. Disk is viewed from the bottom directly towards the planar surface. Surface anchoring profile rotates with the disk and generates a sweeping motion of the defect lines across the disk surface.

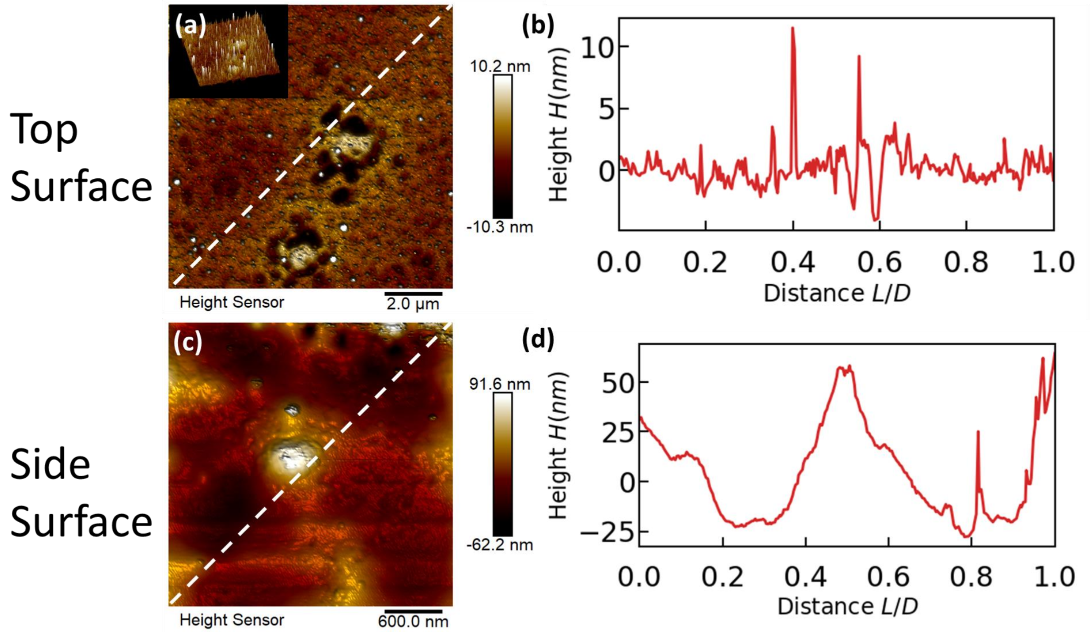

Figure 3.9: Roughness of the disk colloid's top and side surfaces: (a) and (c) AFM images of a 10 µm by 10 µm area on the top surface of the disk and a 3 µm by 3 µm area on the side surface of the disk, respectively. Scale bars are 2 µm and 600 nm. (b) and (d) indicate the height profile along the white dash diagonals in (a) and (c). Note difference in scale in (b) and (d).

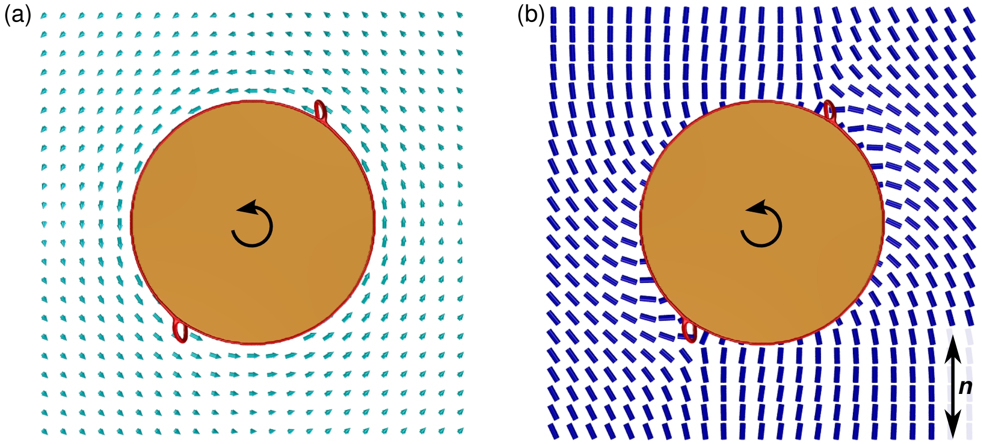

Figure 3.10: Defect displacement in quadrupolar configuration due to rotation of the disk. (a) Flow field due to disk rotation. The magnitude of the flow corresponds to Er = 1.22. (b) Director field is distorted by the flow. Anchoring on the top and bottom plate is along the vertical direction. Rotation of the disk displaces two defect lines along the flow field. The dynamics of the transformation is shown in MovieS16.

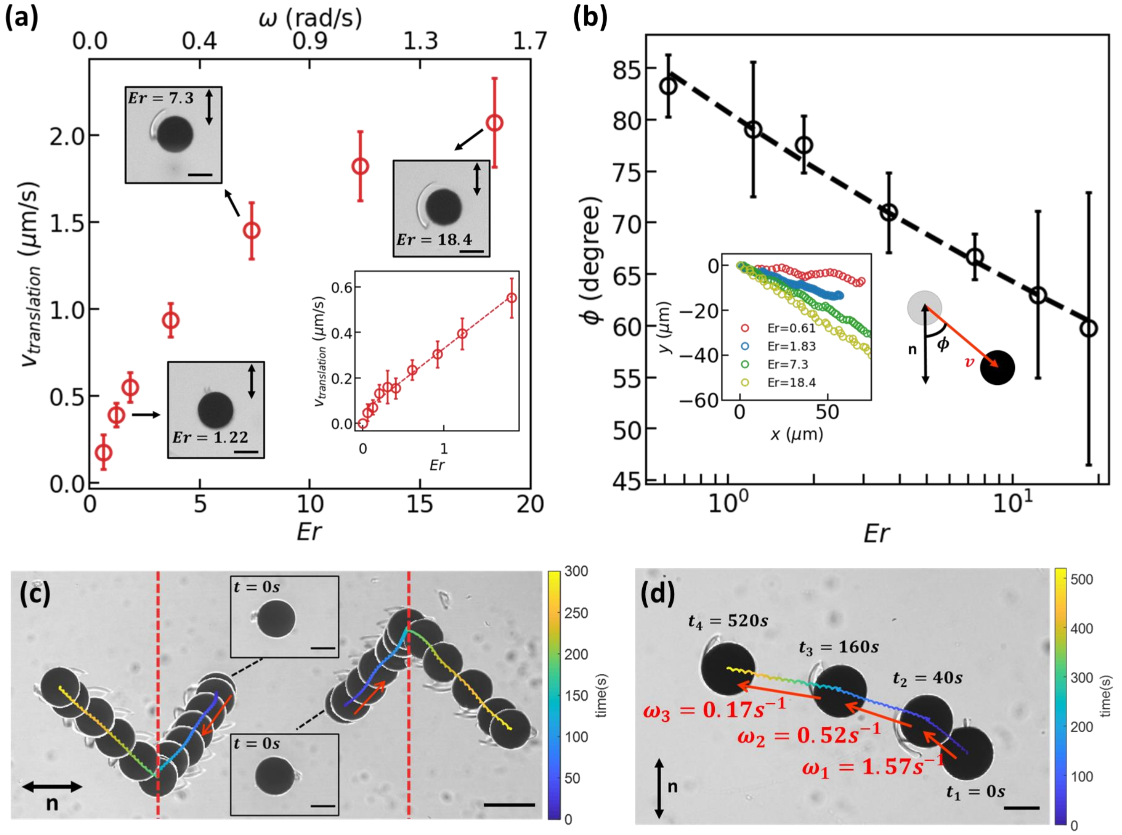

Figure 3.11: Effects of Er and Trajectory Planning: (a) Translational speed and (b) direction of the defect-propelled nematic colloid as a function of Er. (c) Superimposed images (Δt=25 s) of two colloids in same field of view with opposite polarities change swimming directions upon reversing sense of rotation of external field. The period of the external field is 4 s and the red dashed lines indicate the position at which the external field was switched from counter clockwise to clockwise rotation. Insets show static defect structures at t=0 s. (d) A curved trajectory of a disk colloid in 520 s. Angular velocities are labeled in red for each time period respectively. Scale bars are 50 μm in (a), (b) and (d) and 100 μm in (c).

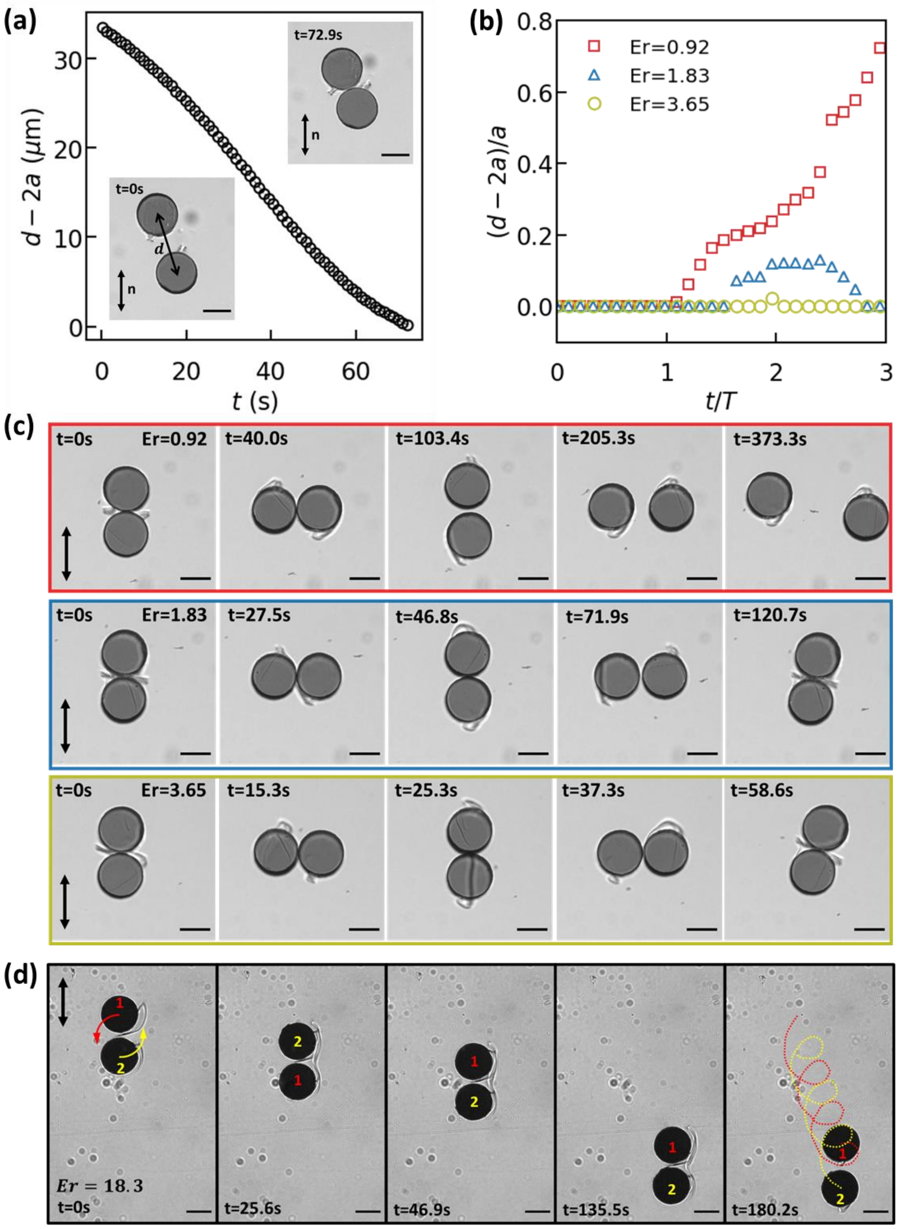

Figure 3.12: Pair interaction between two swimmers: (a) Change in interparticle distance $d-2a$ between two non-swimming (i.e. no external magnetic field) colloids with opposite defect polarities. Insets show configurations at t=0 s and 72.9 s. (b) Normalized interpaticle distances as a function of time of Er = 0.92 (red squares), 1.83 (blue triangles) and 3.65 (yellow circles).(c) Time-stamped images of dynamic pair interactions of colloids with opposite defect polarities under rotating fields of T= 80 s (top row), 40 s (middle row) and 20 s (bottom row) respectively. (d) Time-stamped images of co-rotation and translation of dimer formed by two colloids (labeled as 1 and 2) with similar defect polarity under rotating field of T= 4 s. The red and yellow dash curves in the last frame indicated the curvilinear trajectories of colloids 1 and 2 respectively. Scale bars: 50 μm.

Chapter 4

Directed assembly in nematic liquid crystals (NLCs)

In this chapter, I introduce the background of particle assembly in NLCs and then briefly describe the work on lock-and-key interactions from our group in static settings for both isotropic and anisotropic particles. Finally, I demonstrate directed assembly of passive colloids around a free object in NLCs as a preamble before I talk about micro-robotics in NLCs in the next chapter. Part of this chapter is adapted from [195]. This work is done in collaboration with Yimin Luo and it was originally published in Langmuir [Luo, Yimin, Tianyi Yao, Daniel A. Beller, Francesca Serra, and Kathleen J. Stebe. "Deck the walls with anisotropic colloids in nematic liquid crystals." Langmuir 35, no. 28 (2019): 9274-9285.].

4.1. Background: Colloidal assembly in NLCs

Nematic liquid crystals (NLCs) are excellent candidates to embed extra information for particle assembly due to the internal elasticity of the nematogens. The director of NLCs distorts near solid boundaries which gives rise to long-range elastic interactions and complex behaviors. The elastic energy landscape embedded in the system provides strong guidance ($Ka \sim 10^4\, k_B T$ for colloids of radius $a = 1 \mu m$) to position the particles. The director field of NLCs, which plays a significant role in colloidal assembly, can be disturbed under external electric or magnetic field due to the anisotropic nature of NLC molecules. Furthermore, the molecular ordering disappears when they are heated above their phase transition temperature, and they behave as isotropic fluid. Therefore, NLCs are reconfigurable and so are the colloidal assemblies in NLCs.

However, a global melting strategy lacks control over individual colloids and seldom leads to regular structures through phase transition: the colloids fall into random trapped states where their defects become an entangled mess as the system is cooled from the isotropic state back to the nematic state. Strategy to induce localized melting in NLCs can be realized using laser tweezers. By more direct intervention, colloids can be guided into a remarkable array of complex structures. These methods rely on high resolution control of the laser tweezers for targeted melting to help the system find metastable states. Colloidal assemblies of remarkable regularity ranging from photonic crystals [204], colloidal wires [185], entangled knots [205], and hierarchical assembly [206] have been demonstrated using this approach. Laser tweezers are fantastic tools to probe inter-particle interaction but they require highly-sophisticated setup and alignment process, personnel training, and are challenging to scale up. Another strategy to induce localized phase transition is to dope the NLCs with a push-pull azobenzene dye. The phase transition of a nematic liquid crystal is caused by the dynamical disorganizing effect of the push-pull azobenzene dye on the liquid crystalline order through its trans-cis-trans photoisomerizaion cycle under visible light [207, 208]. This approach requires much lower laser intensities and simper setup than laser tweezers and it has been utilized for collecting and organizing particles in liquid crystals [208].

An equally promising route to colloidal assembly focuses on exploiting topological defects, which can be engineered to appear predictably by rules of topology. It has been reported in literature that micro- and nano-particles could be successfully assembled by point and line defects [209, 210]. Such phenomena can also be expanded to all kinds of defects including Saturn rings [206], boojums [211], point defects of strength $m_i = \pm 1$ in capillary [212], and disclination lines in micro-fluidic channels or hybrid cells [213, 214]. Studies on disclination loops on cylindrical or helical structures [215, 184] reveal that it is possible to sort particles based on the orientation of the colloid and its associated defect and defect type with the disclination loop. Furthermore, a cell-spanning disclination line, created by deliberately seeding defects on the boundary plates via antagonistic anchoring conditions, has been used to assemble a micro-wire of colloids [216, 173]. Due to strong elastic interactions between the particle and defect structure, assemblies in defects are typically irreversible.

There are interactions within NLCs that might allow reversible assembly. Related methods rely on matching the distortion field made by the particle with the director field. This method depends not only on the colloid surface anchoring and defect configuration, but also on the local director field enforced by information embedded in the system. For example, information can be embedded via a photo-patterned substrate with designed regions of splay and bend deformation. Particles can migrate to preferred locations to match the bend and splay associated with the colloid and the substrate [175, 176, 191]. Alternatively, micro-structures can also embed information through their geometry and topology and shape the surrounding energy landscape. In those systems, particles can assemble at preferred sites on a boundary based on geometrical complementarity via the so-called lock-and-key interaction [187] which I describe in greater details in later sections.

4.2. Static lock-and-key interaction in NLCs

Inspired by biological systems where a 'lock' substrate perfectly fits into the cavity of a 'key' enzyme, thus promoting catalytic reactions [217], the concept of "lock-and-key" has been explored in colloidal science to direct the assembly of micro-particles. It has been demonstrated that particles with complementary shapes can assemble into structures through depletion interactions in isotropic fluid [218, 23]. Additional studies on the shape of the colloids have demonstrated that rotational degree of freedom of anisotropic colloids, such as ellipsoidal particles or moon-shape particles, also plays a role in determining the fate of whether and how the key colloid docks in the lock [219, 220].

Similarly, a colloid in LC can feel the attraction from a cavity of complementary shape and anchoring condition through elastic interaction that arises from matching the distortions in between. The "lock-and-key" interaction in NLCs has first been proposed by Silvestre et al. in two-dimensional (2D) systems [187]. Using numerical simulations, they demonstrated that there was strong attraction between colloidal disks and structures or sculpted walls with homeotropic boundary condition and cavities that match closely the shape and size of the colloids. Therefore, the colloid docks into the well by minimizing the Landau–de Gennes free energy functional of the nematic orientational order parameter as the boundary does not only serve as a complementary docking site, but also dictates the energy field in the vicinity. Later on, full three-dimensional simulations confirmed the initial concept [188, 189]. For example, Eskandari et al. studied interactions between spherical colloids and a substrate with both convex protrusions or concave dimples of both planar and homeotropic anchoring conditions. The results revealed that particles migrate to the wells if the anchoring of the particle and the substrate is identical and to the hills if the anchoring is different. This phenomenon has also been demonstrated experimentally in a work by Silvestre et al. [190] in which convex protrusions can efficiently trap colloidal particles with an unlike anchoring condition. Note that although the homeotropic particles in those simulations were always companioned by Saturn ring defects, this concept should also be applicable to microscale particles or particles with dipolar hedgehog companion defects.

The original studies suggested that the energy is lowered through the “defect sharing” mechanism: the two 1/2 defects adjacent to the particle move towards the corners of the isolated cavity and merge with the distorted region of the nematic matrix in the absence of the colloid [187]. Afterward, a full 3D study revealed that small variations in the geometry of the substrate led to important changes in the “lock-and-key” interactions in NLCs. The results that a cylindrical channel provides the strongest interactions with a particle, suggesting another mechanism by matching the distortion of the nematogens in the region between the colloid and the substrate (nano-channel) [188]. Both studies predicted that local director field created by topographical features in NLCs can be used to direct the motion of particles.

4.2.1. Defect-free NLCs domain for colloidal assembly

In previous studies from our group [192, 194], Luo et al. have presented an experimental system that confirms the lock-and-key mechanism for particles with both quadrupolar Saturn ring defects and dipolar hedgehog defects. An experimental system was designed in which a wavy micro-stripe was sandwiched between two glass slides with antiparallel uniform planar anchoring. Such a boundary molds the director field around it which can be sensed by passive colloids in the vicinity of the structure and, therefore, defines attractive and repulsive sites for colloidal assembly. The experimental setup is schematically shown in Fig. 4.1a which allows visualization from a bird's-eye-view under optical microscopes and the motion of passive colloids is purely elastically driven as they migrate in the cell along the horizontal direction.

The wavy wall is made of SU-8 photoresist featuring a series of hills and wells, with amplitude $2A$ measured from the bottom of the well to the peak on the hill as shown in Fig. 4.1b. Strong homeotropic anchoring is imposed on the surface of the wavy wall, creating a series of splay and bend distortions along the wall in the near field. In particular, the valleys are sites of converging splay distortions, the hills are sites of diverging splay distortions, and the inflection points are sites of maximum bend distortion (Fig. 4.1c). The wavelength of the structure λ is associated with the radius of curvature R and the amplitude A: $\lambda = 4R\sqrt{\frac{A}{R}(2-\frac{A}{R})}$. Therefore, λ and R are not independent for a fixed A. Different aspects of the colloid-wall interaction are best described in terms of one or the other. For example, the range of the distortion is discussed in terms of λ, and the splay field near the well is described in terms of R. The gentle undulations of this wall deform the surrounding director field but do not seed defect structures into the NLC. Deeper wells, such as those discussed later in this Chapter, are also characterized by their well depth Δ, and opening Ω.

As a result of the undulation curvature, the gentle hills and wells of the walls become sites of splay distortion in the nematic director field $\mathbf{n}$. The distortion in the bulk decays smoothly away from the wall without introducing any topological defects. It is instructive to consider a Fourier mode of the function defining the wall shape:

$$h(x) = Acos(kx). \tag{4.1}$$

Under the one-constant approximation and assuming small gradients in the director field, **n** can be expressed simply (Fig. 4.1c):

$$\begin{cases} n_x = Aksin(kx)e^{-ky} \\ n_y = 1 \end{cases} \tag{4.2}$$

where n_x, n_y are x and y components of the director.

This director field could be realized either near walls with shallow hills and dales, or, alternatively, in regions far enough from the wall where gradients in **n** are weak. This form suggests hills and dales are sites with the highest splay energy density, while the inflection points are sites with highest bend energy density. The distortion created by a particle with homeotropic anchoring always induces a defect, either an elastic dipole or a Saturn ring [221].

The alignment of a colloid-free cell was examined under crossed polarizers (Fig. 4.1d, e), which showed that the bulk liquid crystal was defect-free. The much brighter texture at 45°-135° (Fig. 4.1d) compared to the 0°-90° (Fig. 4.1e) also shows good planar alignment along the y-direction given by the bounding plates. The defects visible in Fig. 4.1d,e are only in the thin NLC film squeezed between the top of the wavy wall and the confining glass, a region which is not accessible to the colloids.

4.2.2. Lock-and-key interactions of isotropic particles near wavy wall

With the defect-free NLCs domain near a wavy boundary described above, previous studies in our group have demonstrated different assembly behaviors of spherical particles with both quadrupolar Saturn rings and dipolar hedgehog defects via the lock-and-key mechanism in NLCs [192, 194]. For a colloid with Saturn ring defect, as shown in Fig. 4.2, it is attracted toward the well in a time span of 20 s. The particle, initially situated near a hill on the wavy wall, moves away from this position due to the mismatch of the director field between the colloid and the wall (Fig. 4.2a). After it moves past the hill, the colloid quickly finds the attractive site and docks into the neighboring well following a trajectory indicated by the yellow curve in Fig. 4.2e. During this process, the Saturn ring around the colloid gets lifted to accommodate the shape of the well, evidencing subtle director rearrangement during the docking process. This docking behavior can be explained by the lock-and-key mechanism as the colloid finds its equilibrium position by minimizing the distortion in the system as shown in Fig. 4.2f. The splay distortion from the bottom of the well matches the splay distortion near the south pole of the colloid, and the bend distortion near the inflection point of the wall matches the bend distortion around the waist of the colloid, a phenomena we describe as ‘like likes like’.

Directed assembly of spherical particles with dipolar hedgehog defects have also been investigated using smaller particles in the same setting. Unlike particles with Saturn ring defect, particles with dipolar defect show different docking configurations: the dipole can attach to either hills or wells, according to its defect orientation with respect to the wall (Fig. 4.3). In the case of a particle with the defect pointing away from the wall, the well is still the preferred location as the splay distortion from the well still matches the splay distortion from the bottom of the particle where the defect is not present as shown in Figs. 4.3a and b. However, if the defect is oriented towards the wall, the equilibrium position of the colloid is on the hill (Fig. 4.3c,d). In both cases from particles with either dipolar or quadrupolar defect, the geometry of the wavy structure and boundary anchoring condition largely affect the docking behaviors. Tunable colloid trajectories in NLCs near wavy walls have been demonstrated using various wall geometries and particle anchoring conditions [194].

4.2.3. Lock-and-key interactions of anisotropic particles near wavy wall

Particle shape also influences assembly behaviors in NLCs. Anisotropic particles interact in complex manners influenced by features like facets and edges or highly curved sites [181, 222, 185, 162, 168]. In all of these settings, the shape and the alignment of the liquid crystal molecules on the colloid surface play an important role in determining how the particle is assembled in a given energy landscape. Based on previous studies in our group on isotropic particles, it is a natural extension to probe the behavior of anisotropic particles in similar settings, as the surfaces of these particles have smoothly varying curvatures to introduce a complex distortion field. In this section, I describe a project I developed in collaboration with Yimin Luo in which we explore the behavior of an ellipsoid near a shallow well of curvature and width similar to the colloid diameter, and note the equilibrium position realized by the colloid in relation to various geometry parameters. Thereafter, we study ellipsoidal particle interactions with deep narrow wells. This section is adapted from ref. [195] which was originally published on Langmuir.

To study ellipsoidal particles with homeotropic anchoring, we fabricate particles with controlled anchoring by coating silica on the surface of stretched polystyrene (PS) particles. To avoid deleterious effects associated with swelling of PS in the NLCs and degradation of the anchoring, we perform all experiments within three days of introducing ellipsoids into liquid crystal. PS particles of two different sizes ($2a = 10$, 25 μm) are stretched. Homeotropic ellipsoidal colloids also impose defects and generate companion defects in an otherwise uniform director field [180]. Homeotropic ellipsoids in NLCs generate three distinct configurations. The hedgehog or dipolar defect configuration has the colloid's major axis aligned with the far field director. The axisymmetric quadrupolar configuration has a small Saturn ring in the plane defined by the two minor axes, and the colloid's major axis aligned with the far field director. Finally, a second Saturn ring configuration has the major axis perpendicular to the far field director and a defect loop that wraps the ellipsoid lengthwise. We refer to the latter two configurations as Saturn I and Saturn II, respectively.

Ellipsoids far from the wall

We have performed control experiments to compare the behavior of homeotropic ellipsoids to prior observations of ellipsoids and other elongated particles [223, 224, 225, 180, 181]. Here, we discuss key findings that influence our understanding of colloid-wall interactions. We confine ellipsoids with semi major axis α and semi minor axis β (Fig. 4.4a) in sandwich cells filled with NLC. The top and bottom surfaces of these cells have oriented planar anchoring in an anti-parallel arrangement to minimize tilt from rubbing, separated by a distance H = 25-45 μm. Once confined in these cells, the orientation of the ellipsoid's major axis differs by some angle θ from the direction of the uniform far field director as defined by the rubbing direction $\mathbf{N}$. We study particles with aspect ratio k from 1.5 to 7.5, where k is defined as $\frac{\alpha}{\beta}$. For smaller colloids (stretched from $2a = 10$ μm PS particles) that are only weakly confined, we primarily observe dipolar structures with the hedgehog localized at the pole of the ellipsoid (Fig. 4.4b,c), and only occasionally observe Saturn rings. While the dipole configuration was not discussed in Ref. [180], a dipole-like "tip-ring" configuration was simulated. In that study, the particles are much smaller (stretched from $2a = 2$ μm PS particles). In Ref. [223], dipole and Saturn ring coexist in a confined setting for rod-like particles (cross section $2a = 1.5$ μm), but only Saturn II is observed. In our work, for larger particles (stretched from $2a = 25$ μm PS particles) in cell thickness $H =$ 25-35 μm, all three configurations are observed, dipole (Fig. 4.4b,c), Saturn I (Fig. 4.4d,e) and Saturn II (Fig. 4.4f,g). They each occur 44%, 23% and 32 % of the time, respectively. When we place the same colloid (stretched from $2a = 25$ μm PS particles) in cells of thickness $H =$ 35-45 μm, only dipoles are observed.

Ellipsoids with dipolar and Saturn I configurations orient along angles distributed around the rubbing direction $\mathbf{N}$, i.e. around $\theta = 0^\circ$ (Fig. 4.5), while Saturn II configurations align along angles distributed around $\theta = 90^\circ$ (Fig. 4.5). Simulation of the elastic energy in Ref. [180] reveals several behaviors relevant to our studies. First, the Saturn II configuration is the equilibrium state far from the wall under strong confinement ($h \leq 2\beta$). The dipole is the equilibrium configuration for microscale unconfined prolate ellipsoids as it is for spheres. Second, the Saturn I configuration is degenerate in θ for angles less than $\theta < 15^\circ$; i.e. there is no torque for small θ to enforce alignment until some critical angle. For $k = 3$, there is a plateau in the energy of the system; for $k = 5, 7$, the plateau becomes a secondary minimum. The energy gradient near $\theta = 90^\circ$ is also weak. These findings may explain the wide distribution of alignment angles observed in experiment, although Saturn ring pinning at rough sites on the particle surface may also play a role. Third, the distribution and strength of distortions in the director field differ strongly for the two Saturn configurations. Guided by simulation of a colloid of same k for Saturn I and II, we note that the Saturn

II configuration has strong splay distortions isolated near the highly curved tips (Fig. 4.4i), while distortion density around the Saturn I is generally more uniformly distributed around the colloid (Fig. 4.4h).

These differences in the distortions around the Saturn configurations suggest that the forces on Saturn I and II should have different ranges and strengths of interaction. The Frank free energy, valid for weak distortions, can be used to arrive at scaling arguments. In the one constant limit, the Frank free energy is expressed as [226]:

$$F = \frac{K}{2} \int \left[(\nabla \cdot \mathbf{n})^2 + (\nabla \times \mathbf{n})^2 \right] dV \tag{4.3}$$

where the integration is taken over a volume where the nematic order is nonsingular. In the Saturn II configuration, the strong distortion near the tips can be approximated as $\sim K\beta$, whereas the distortion along the length of the Saturn I configuration can be approximated as $\sim K\alpha$. The LdG simulation, valid for large distortions, supports these scaling arguments in that the amount of distortion is roughly proportional to the semi-axis of the colloids (Fig. 4.4h-i). Experiments indicate that the range of interaction between a pair of particles is approximately equal to the size of the particles [225, 223]. A related argument has been used to justify the transition to non-aggregated state of long k ellipsoids with planar anchoring [224]. For the Saturn II configuration, the regions of strong distortion at the tips are highly sensitive to perturbations in the bulk director field and play a strong role in wall interactions.

Ellipsoid near shallow wells: Saturn Configurations

We then study ellipsoids near shallow wells (Fig. 4.7), for which the amplitude of the wall geometry $\mathcal{A}$ is much less than the wall radius of curvature R, and colloid length 2α is comparable to the well width $\lambda/2$, defined as the horizontal distance between two hills. Particles in both Saturn I and II configurations equilibrate at some distance from the bottom of the well, roughly centered above the well. Furthermore, both configurations persist, even near wells whose curvature is more compatible with the Saturn II configuration. Ellipsoids initially in Saturn I configurations enter wells with only small changes in angle along their paths, and remain in a nearly upright position. Ellipsoids initially in Saturn II configurations find nearly horizontal positions. Simulation shows that the Saturn II configuration indeed has the global minimum energy. We suspect that the Saturn I configuration is stabilized by the degeneracy of the energy to the inclination angle for small tilt angles reported for colloids in bulk. Indeed, simulation reveals that this degeneracy persists close to the wall. This is shown in Fig. 4.6a, in which the total elastic energy of the system is shown for ellipsoids with their centers of mass fixed at some height ($y = 153\ nm$) above the well as a function of angle θ for $k = 2$ and $k = 4$. Note that a plateau exists for $k = 4$, but only a weak gradient exists for $k = 2$. Thus, for Saturn I configurations with only weak inclination angles, there is no torque to drive rotation to the equilibrium Saturn II configuration. Images of the director field for colloids at their minimum energy state for fixed horizontal (Saturn II) and vertical (Saturn I) orientations are shown in Fig. 4.6b, c. The orientation of the colloid is an input to the simulation, just like the experiment, here we consider the Saturn I configuration as effectively metastable.

We track the position of the ellipsoids with Saturn I (Fig. 4.7a) and Saturn II (Fig. 4.7b) with $k = 2$. For spherical colloids in shallow wells with widths similar to the colloid radius, the Saturn ring remains at the equator of the colloid and the concept of splay matching captures the particle's equilibrium location. The splay fields emanating from the ellipsoids near the walls generated by the tip for Saturn I and the side for Saturn II can also be estimated. However, at equilibrium, the Saturn I configuration finds a site far deeper in the well than would be expected from splay matching owing to the strong attraction between bend along the particle's sides and that at the well's edge. The Saturn II configuration equilibrates further from the wall than would be expected for splay matching because of strong repulsion between the Saturn ring and the wall for this configuration. To gain deeper insight, we simulate the total elastic energy in the system for a colloid at various locations near the well, as reported in Fig 4.7c, d for the two Saturn configurations for a colloid with

$\alpha = 90\ nm$ and $\beta = 45\ nm$.

For fixed colloid orientation, the center of mass of the particle is placed at points separated by 9 nm on a square grid that discretizes the domain within one wavelength from the wall. In these figures, the thin black line indicates the wall location, the dashed blue line adjacent to the wall is an excluded region where the particle would overlap the wall geometry. The reference energy is the total energy of the system when the particle is situated one wavelength above the well at the centerline. The colloid (blue ellipsoid) is shown at its equilibrium position. By moving toward the wall, the ellipsoid replaces regions of strong deformation and brings particle sourced splay and bend deformations that are compatible with those near the well. The elastic force field experienced by the ellipsoid is computed by using Newton's difference method to take the negative gradient in the elastic energy. The resulting vector field is graphed atop the energy landscape diagrams (Figs. 4.7c, d). These vectors define complex paths for ellipsoids with fixed angle throughout their migration. We will explore the predicted paths in future work, as the current particles are not responsive, and cannot be easily reoriented or positioned e.g. by external magnetic fields. The simulated elastic force fields in Figs. 4.7c and d includes the contributions from the complex director for the colloid confined in our system. To guide intuition, we discuss sites of compatible bend and splay with the wall. However, we study ellipsoids, objects of revolution, between top and bottom plates interacting with the undulating wall. The resulting director field is complex and three dimensional. Distortions above and below the objects, i.e. between the colloid and the top and bottom planes, repel the colloid from those bounding surfaces [227]. Near field details owing to the three-dimensional nature of the director field between the colloid and the undulating walls likely also contribute to near field repulsion and prevent the colloid from touching the undulated wall.

Thus far, we have shown that prolate ellipsoids interact via bend and splay near the wall with shallow undulations. The strength of this interaction can be characterized as a "binding energy" or difference in total system energy for a colloid far from the wall and at its equilibrium position. We chose the reference energy for this calculation when colloid is located at $y = 338$ nm from the wall and we round the simulation results to 0.1 simulation units. For ellipsoids of $k = 2$, the binding energy for the Saturn I configuration is -144±0.4 k_BT, while that for Saturn II is -81±0.4 k_BT. Thus, the Saturn I configuration is more strongly bound, even though it always has the higher system energy. This might be ascribed to the strong distortion near the tips in the Saturn II configuration; near these poles, the Saturn II experiences a repulsive region very near the wall.

We also find the total energy of the system when the colloid is located far and near the wall for ellipsoids of $k = 4$ (Fig. 4.8) for the same wall geometry and ellipsoid volume. We conserve volume to mimic our system in which particles of different aspect ratio are obtained by stretching beads of fixed volume. As the colloid length becomes comparable to the well width, near wall repulsion becomes more significant for Saturn II (Fig. 4.8b). For these colloids, the binding energy for Saturn I is -129±0.4 k_BT, while that for Saturn II weakens to a value of -52±0.4 k_BT. Given bulk energy $\sim Ka$, we may rescale the simulated elastic energy to find a rough estimate of the energies in the experimental system. These estimated binding energies are determined by to -3.2, -1.8, -2.9, -1.2 $\times 10^5$ k_BT for Saturn I ($k = 2$), Saturn II ($k = 2$), Saturn I ($k = 4$), Saturn II ($k = 4$), respectively. All trapping energies are much greater than thermal fluctuations, consistent with the deterministic paths followed by the objects. They are similar in magnitude to estimates obtained in prior research by analyzing spherical particles in experiment in which viscous dissipation was inferred along a particle path [192].

The distribution and type of distortion in the nematic director field depend on particle shape. For a sphere, the distortion around it has splay and bend elements, with pronounced distortion near the defect ring. For ellipsoids in the Saturn I configuration, there is strong bend along the sides, and strong splay at poles, while the Saturn II configuration has strong bend and splay deformations at its equator, with only weak distortions on the top and bottom. Distortion fields decay non-uniformly around the ellipsoids in Saturn I and II configurations, yielding directionally dependent ranges of interaction which differ from a sphere of equal volume ($a^3 = \alpha \times \beta^2$).

To summarize these observations, we record the final position of ellipsoids above the well center line for colloids of varying k for well widths greater than the ellipsoid semi major axis ($\lambda > 2a$). We define y_{obs} as the height of the colloids center of mass from the base of the well center (Fig 4.7e). To relate the final position of the colloid to various geometric parameters of the system, we define well aspect ratio $k_w = \frac{2A}{\lambda}$ and ellipsoid aspect ratio $k_e = \frac{Y}{X}$. In this quantity, X, Y are the lengths of the semi-axes in the x and y directions, respectively (Fig 4.7e). For the Saturn I configuration, $X = \alpha$, $Y = \beta$, and $k_e = k$, whereas for the Saturn II configuration, $X = \beta$, $Y = \alpha$, and $k_e = 1/k$. To capture the effect of well geometry we define $\sigma = \frac{k_w}{k_e}$; for shallow wells, $\sigma < 1$. We plot the y location of the particle normalized by its semi-axis length along the y direction $\frac{y}{Y}$ against the quantity $\sigma = \frac{k_w}{k_e}$ (Fig 4.7f). We find σ to be the relevant parameter that captures system behavior. This scaling shows that colloid equilibrium distance from the base of the well decreases with increasing colloid aspect ratio in its aligned direction k_e, and that colloids above wider wells are located lower than colloids over narrower wells.

Particles entering deep wells

While both Saturn configurations were able to interact with shallow wells, we expect narrow, deep wells to be only accessible to the Saturn I configuration owing to steric constraints. Furthermore, the Saturn II configuration should be repelled by the hills that we have placed adjacent to the deep wells, and should fail to dock to the wall. Thus, interactions with the wall should be selective on the basis of colloid orientation. We expect Saturn I to dock, while Saturn II will not. To explore this behavior, we fabricate deep, narrow wells with nearly straight side walls and a circular base. The wall that we studied is shown in Fig. 4.9. It features wall undulations with hills and wells of differing depths, all with widths comparable to particle minor axis. The depth of the well equals to α, and the bottom of the well is semicircle of diameter $2R_{\text{well}} = 15$ μm. Indeed, we observe strong interactions between deep wells and Saturn I configurations. We have observed Saturn II configurations drifting above these high frequency undulations without apparent attraction.

Figs. 4.9a-d shows snapshots of an ellipsoid in the Saturn I configuration as it enters a well. The entire trajectory is shown as the white dashed line. The colloid is attracted over distances comparable to its major axis. Initially, the Saturn ring is pinned at a slightly tilted configuration, as the particle moves into the well, the tilting is gradually corrected, although not completely (Fig. 4.9b-c). As the ellipsoid docks deep within the well, the ring shifts upward (Fig. 4.9d). Fig. 4.9e shows the change in particle position at equally spaced time increments, allowing changes in rate of motion to be captured. As the colloid enters the well, it moves more rapidly in spite of its proximity to the wall and large associated hydrodynamic interactions, indicating steep energy gradients there; we associate this with the highly compatible bend and splay fields from the colloid and the wall. Recall that the microscope stage is horizontal; this insertion of this high aspect ratio object into this deep well is guided entirely by the elasticity of nematic director field.

As the ellipsoids interact with the wells, the Saturn rings can be displaced by interaction with the wall. Previously, we have studied this displacement for spheres, and found that elastic interactions with the wall can drive an irreversible quadrupole-to-dipole transition. We identified a critical angle of 130°, below which the ring could distort and recover, and above which the transition was irreversible [194]. In this study, although the Saturn ring shifts upward, such a transition has not been observed for ellipsoids.

4.3. Directed assembly of passive colloids around a designed 4-armed micro-robot

To harness the lock-and-key interactions for micro-robotics, we designed and fabricated a ferromagnetic 4-armed micro-robot using standard lithographic methods, followed by PVD sputtering of Ni. Subsequently, the micro-robot is treated with dimethyloctadecyl [3-(trimethoxysilyl)propyl] (DMOAP). The resulting micro-robot has homeotropic (perpendicular) anchoring on its Ni-coated top and sides, and degenerate planar anchoring on the bottom face. When placed in a planar cell with anti-parallel anchoring filled with 5CB (Fig. 4.11a), the micro-robot molds the local director field. The micro-robot's arms and wells have curvatures designed to generate gentle distortions in the domain to promote lock-and-key assembly of passive colloids, akin to that reported previously near wavy walls [192, 194]. Furthermore, once placed in the planar cell, two different defect structures emerge, depending on the gap thickness between the two plates. For strong confinement, a metastable defect configuration with quadrupolar symmetry emerges, with two apparent defects at the tip of the two arms aligned perpendicular to the far field director. For weaker confinement, a stable configuration with dipolar symmetry emerges, with a single apparent defect that can appear at the tip of either arm aligned parallel to the far field director as shown in Figs. 4.11b and c. Numerical simulation (Fig. 4.11d) reveals that this defect is a disclination loop anchored on two locations on the degenerate planar face and it extends along the side of the disk toward the homeotropic face. The quadrupolar structure irreversibly transforms to the dipolar structure under external perturbations. Given the micro-robot's complex anchoring and sharp edges, these defect configurations differ significantly from their well-known counterparts on smooth particles with uniform anchoring. To study these micro-robots in interaction with passive colloids under weak confinement, DMOAP-treated silica particles ($2a = 25\,\mu\text{m}$) with homeotropic anchoring are added into the micro-robot suspension in 5CB; this suspension is introduced into the planar cell in the isotropic state, and subsequently quenched into the nematic state by cooling below the isotropic-nematic transition ($T_{NI} = 35.2°$). In the nematic state, as expected, the silica colloids have a dipolar hyperbolic hedgehog companion defect.

The far field director field around the micro-robot shown in Fig. 4.11d resembles the director field around a spherical colloid with a hedgehog defect. Furthermore, due to the concave regions between the arms of the micro-robot and the presence of the defect on a specific arm aligned with the far field director, the director field around the micro-robot is left-right asymmetric along the director. To further understand the effect of this director field on the interactions between passive colloids, a point dipolar defect was placed in the vicinity of the micro-robot and the system free energy was calculated in the quasistatic limit using Landau–de Gennes simulation. By changing the position and polarity of the point dipole, embedded energy landscapes for point dipoles of opposite defect polarity far from the robot (left and right) were generated around the micro-robot. At each location, the point dipoles were rotated weakly to find their optimal orientation. Finally, force fields around the micro-robot were computed by taking gradients of the energy profiles (Fig. 4.12), revealing possible trajectories for colloids in the domain. For example, as shown in Fig. 4.12a, a point dipole of left polarity located near the defect of the micro-robot can be attracted to the micro-robot. Furthermore, several separatrix (purple dashed lines in Fig. 4.12) are observed in the simulation, suggesting colloids placed near the locations could have strikingly different final assembly configurations. Therefore, when this micro-robot moves under external field, it carries the embedded force field with it as a form of physical intelligence. Colloids in the domain sense the distortions and move accordingly by a combination of bottom up and top-down assembly.

By controlling the pose of the micro-robot using a external field, five types of assembly configurations were observed: (i) a dipole chaining configuration in which the colloid chains on the dipolar loop adjacent to the robot with its companion defect outward, oriented along the far field director (Fig. 4.13a), (ii) a dipole on hill configuration in which the colloid docks on the curved tip of the robot arm with its companion defect pointing toward the robot (Fig. 4.13b), (iii) a dipole in well configuration in which the colloid docks in a well with its companion defect pointing outwards, oriented along the far field director (Fig. 4.13c) and (iv) a hybrid configuration where the colloid partially docks in a well with its companion defect tilted toward the nearest arm (Fig. 4.13d) and, finally, (v) a rarely-observed zigzag dipoles configuration in which the colloid assembles with its defect oriented away from the micro-robot's defect in a zigzag structure (Fig. 4.14). The 'dipole chaining' and 'zigzag dipoles' configurations are reminiscent of dipole-dipole interactions of uniform colloids with homeotropic anchoring, although the details of the defect configurations on the micro-robot differ. Note that the 'zigzag dipoles' configuration is rarely observed unless the micro-robot is placed very close to the passive colloids. In the other three cases, the colloids interaction with the curved boundary are a recapitulation of lock-and-key interactions in which colloids interact with gentle distortion fields seeded by the curved boundaries as shown in the insets of Figs. 4.13b-d.

To determine the range of these interactions, we track trajectories and compare the normalized separation distance to their equilibrium position $\frac{d_e}{a}$ as a function of time $t_c - t$, where and t_c is the time when the passive colloid reaches its equilibrium position as shown in Figs. 4.13e-h. The dipole chaining and hybrid configurations show longer ranges of interaction with the largest separation distance observed of almost 6 radii, while for the dipole in well and hybrid configuration, interactions are typically sensed around 2 radii from the colloid's final equilibrium position. Since the colloid-micro-robot interactions are balanced by viscous dissipation, the strength and form of the energy of interaction can be inferred by integration of the drag force along the particle's path. Due to the involvement of defect-interactions, the 'dipole chaining', 'dipole on hill', and hybrid configurations show stronger attraction, on the order of $10^5 k_b T$, while the 'dipole in well' configuration, which involved lock-and-key interactions without involvement of a defect, is on the order of $10^4 k_b T$. Furthermore, the shapes of these energy profiles near contact reveals information concerning the mechanics of the colloid-micro-robot interaction; the curvature of these profiles for the 'dipole in well', 'dipole on hill' and hybrid configurations suggest an elastic interaction, while the linear form of the profile for the dipole chaining suggest a yield force behavior.

For passive colloids with their companion defect facing toward the right (Fig. 4.13i (i)), trajectories observed in experiments are superposed on the micro-robot. A similar image is constructed for the trajectories observed for passive colloids with their companion defect facing toward the left (Fig. 4.13j (i)). Different final assembly configurations are represented using different colors. For example, the green curves represent the 'dipole in well' configuration, while the blue curves represent the hybrid configuration in which the passive colloids first get repelled from the defect of the micro-robot and then get attracted to their final equilibrium positions, resulting in curved trajectories. These observed trajectories were predicted by analysis of the energy map generated from the numerically simulated director field around the micro-robot (Figs. 4.13i (ii) and j (ii)). The multiple modes of assembly around the micro-robot depend on the pose of the micro-robot and the initial positions of the passive colloids. These interactions, which differ in ranges and strength, allow selective directed assembly and can be exploited for cargo manipulations in micro-robotics.

4.4. Conclusions

In this chapter, I briefly review work on colloidal assembly via quasi-static interactions in NLCs including the topological defect interactions and the lock-and-key mechanism. Through the lock-and-key mechanism, we demonstrate directed assembly of spherical and ellipsoidal colloids near a wavy wall by matching the distortion around a colloid with distortion around the boundary. This research establishes that colloids near boundaries with given shapes and anchoring interact and assemble via emergent interactions and motivates our study in which a mobile colloid is used to embed an energy landscape for colloidal assembly. We design a 4-armed magnetic micro-robot with shape and anchoring to embed energy landscapes around the micro-robot. As the micro-robot moves, passive colloids can sense the force field created by the micro-robot and migrate along the force lines predicted from Landau de Gennes free energy landscapes. Experimentally, five different assembly configurations of the passive colloid have been observed and their ranges of interaction and strengths have been characterized. These trajectories correspond to numerical prediction, which captures the main features of the force field such as curved path and separatrix. Therefore, by controlling the pose of the micro-robot, we can selectively assemble passive colloids along particular trajectories which paves the way towards micro-robotic applications described in the next chapter.

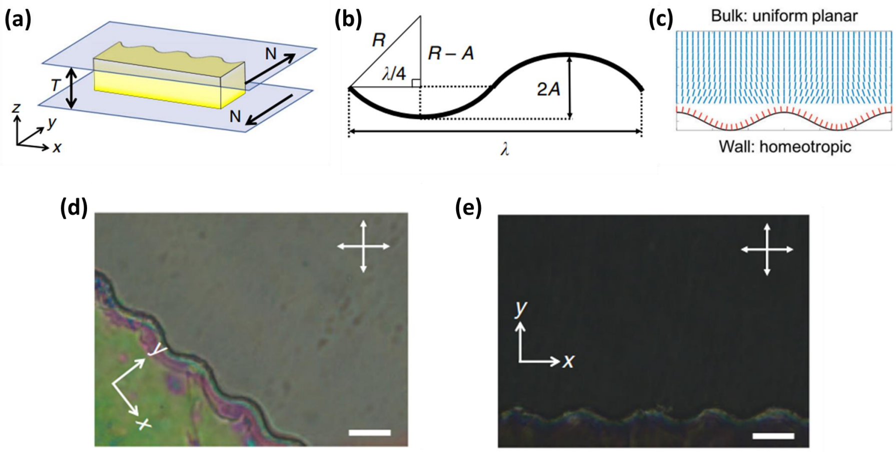

Figure 4.1: Schematics and the director field. (a) Schematic of the experimental setup where **N** denotes rubbing direction and T denotes thickness of the cell. (b) Schematic of the wall shape with relevant parameters: radius of curvature R, amplitude A, and wavelength λ. (c) Simulated director field in the small-slope limit. (d-e) Cross polarized images of liquid crystal near the wavy wall with the long axis either (d) at 45^o angle to the polarizer or (e) perpendicular to the polarizer. The scale bars are 20 μm. Images adapted from [192, 194].

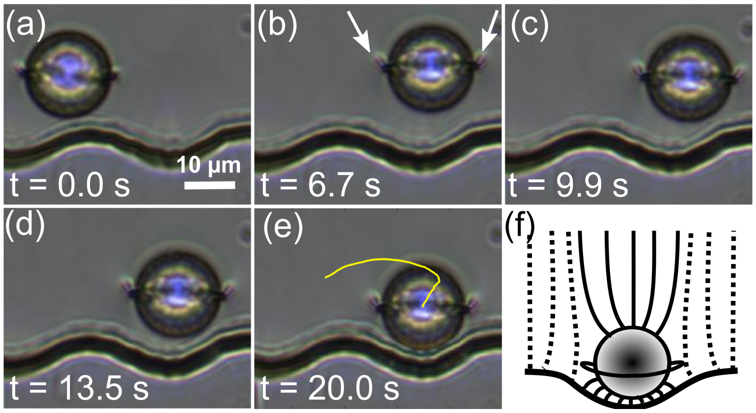

Figure 4.2: Experimental realization of the lock-and-key interaction. (a-e) Time sequence of the particle ($2a = 15$ μm) moving into a cavity of comparable size. White arrows in (b) denote distortion of the Saturn ring. Yellow line in (e) denotes the trajectory of the movement. The trajectory of the particle is extracted by ImageJ and analyzed with MATLAB. This process has been repeated with about 20 different particles and similar trajectories have been observed. (f) Schematic of the director field once the particle docks on the dale, minimizing the total splay distortion. Adapted from [192]

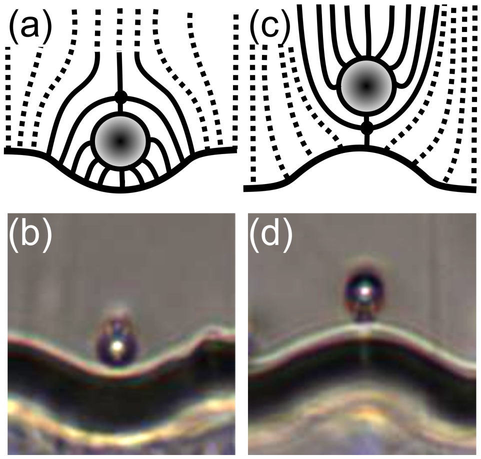

Figure 4.3: Docking of dipoles. Schematic and bright field microscopy images of a particle ($2a = 5\ \mu$m) acting as (a,b) a dipole attracted to a dale with its point defect oriented outwards and (c,d) a dipole attracted to a peak with its point defect oriented towards the wall. Adapted from [192]

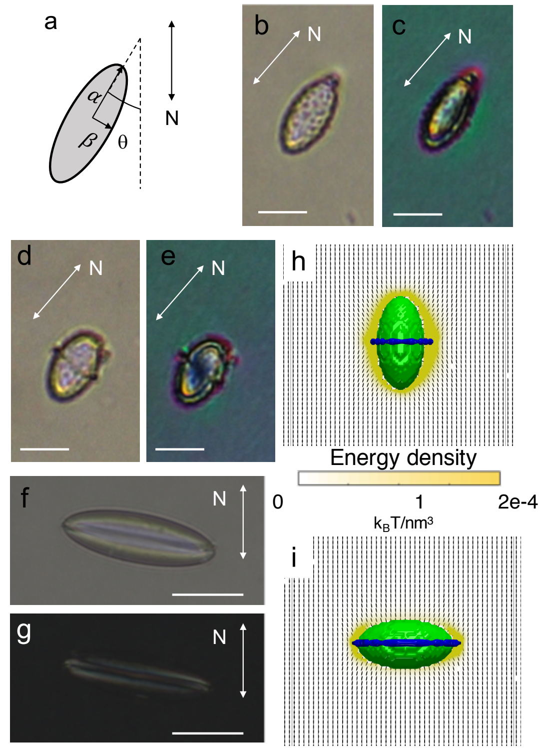

Figure 4.4: Defects and director field around ellipsoids far from the wall. (a) Schematic of an ellipsoid with semi major axis α and semi minor axis β, oriented with its long axis at angle θ with respect to the far field director field **N**. (b-c) Bright field (BF) and cross-polarized (XP) images of a dipole. (d-e) Bright field (BF) and cross-polarized (XP) images of a Saturn I. (f-g) Bright field (BF) and cross-polarized (XP) images of a Saturn II. (h-i) Elastic energy density around (h) Saturn I and **(i)** Saturn II. Simulation colloids have semi major axis $\alpha = 90\ nm$ and semi minor axis $\beta = 45\ nm$. Scale bars are 10 μm in (b-e) and 25 μm in (f-g).

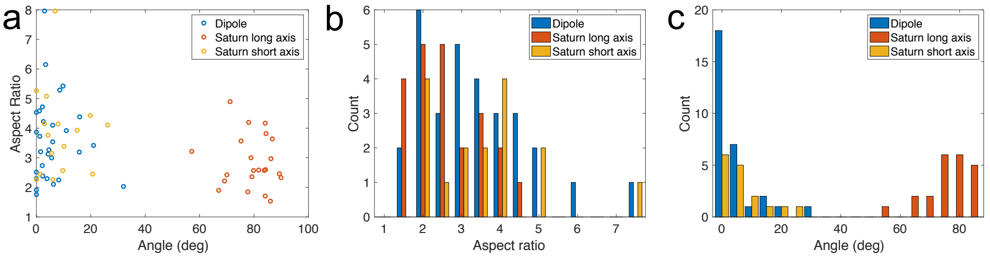

Figure 4.5: (a) Scatter polar of aspect ratio k versus colloid orientation θ. (b-c) Histograms of (b) aspect ratios and (c) orientations of colloids of different defects.

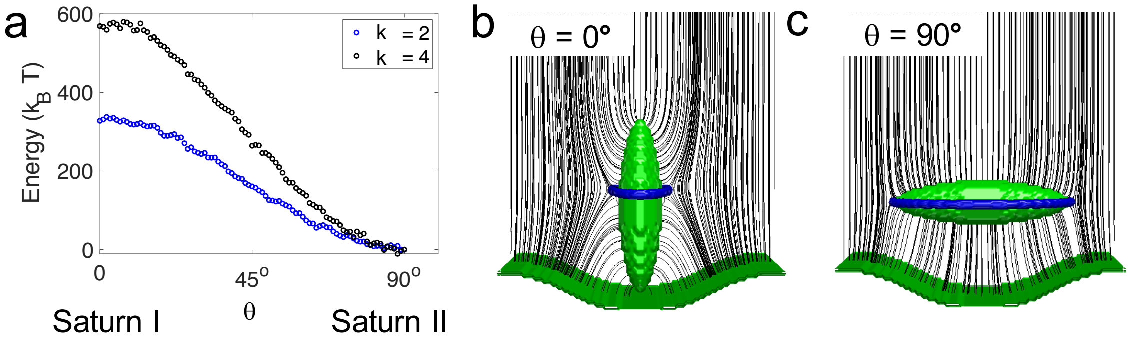

Figure 4.6: (a) Total energy of the system as the colloid goes through rotation from $\theta = 0$ to $\theta = 90°$ configuration when COM is located at $y = 153$ *nm* for $k = 4$ and $y = 99$ *nm* for $k = 2$. (b,c) Simulation snapshots of $\theta = 0$ and $\theta = 90°$ configurations **for a $k = 4$ ellipsoid** where $y = 153$ *nm*. In simulation, colloids have semi major axis $\alpha = 143$ *nm* and semi minor axis $\beta = 36$ *nm*.

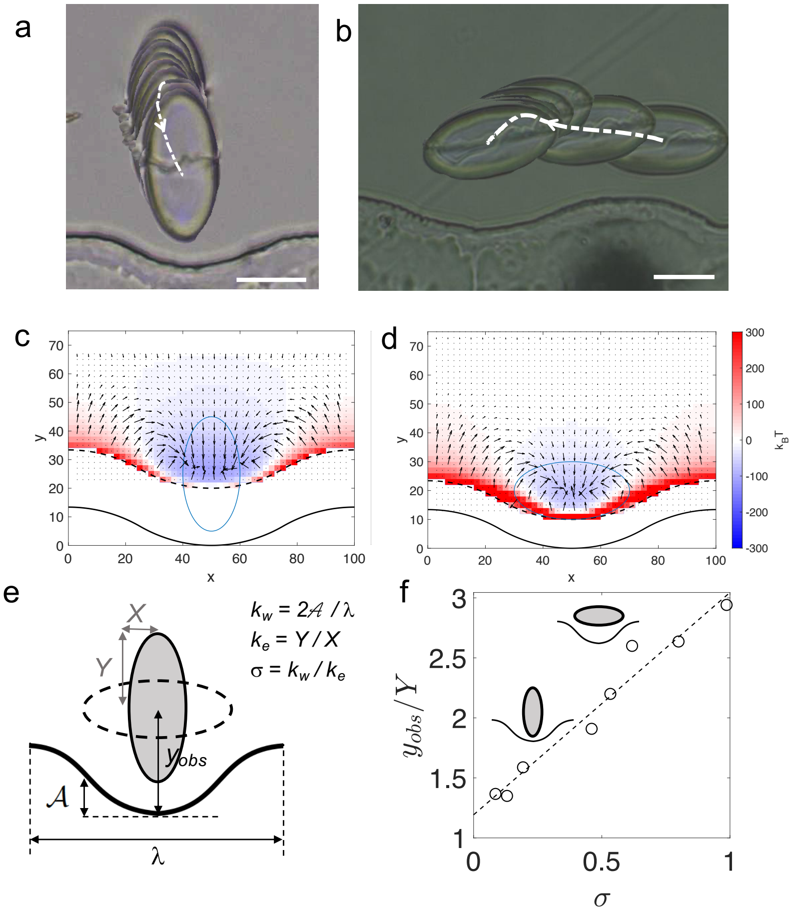

Figure 4.7: Ellipsoids docking near shallow well. (a-b) Composite images of the full trajectories of ellipsoids of $k = 2$ for (a) Saturn I, also in Supplemental Video 1, and (b) Saturn II, also in Supplemental Video 2. White dotted lines denote trajectories of the COM. The scale bars are 25 μm. The energy landscape for (c) Saturn I and (d) Saturn II near shallow wells. Simulations of total energy of the system are presented in the color map, the gradient is computed to show the force field assuming no tilting during migration. Semi major axis α = 90 nm, and semi minor axis $\beta = 45$ nm. Blue ellipses denote the position of the ellipsoid when the system is at lowest energy state. Solid line denotes the wall. Dashed line denotes excluded region next to the wall. (e) Schematic of an ellipsoid right next to the wall, with wavelength λ and amplitude $\mathcal{A}$. $X = \beta$, $Y = \alpha$ for $\theta = 0$ ° and vice versa. (f) Open dots denote normalized COM of the ellipsoids y_{obs}/Y versus σ, the ratio of aspect ratios. Dashed line serves as a guide to the eye.

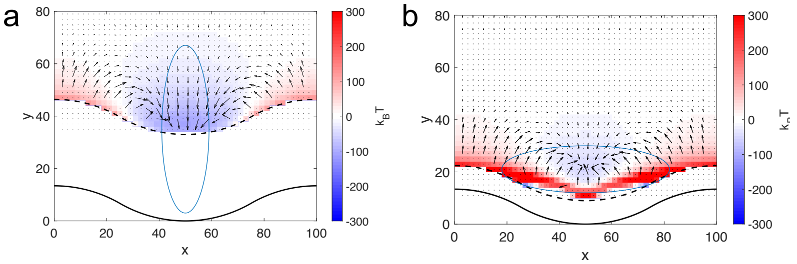

Figure 4.8: (a-b) Simulations of total energy of the ellipsoid (long axis $a = 143$ nm, and short axis $b = 36$ nm) when the center of mass of the particle is located at various locations above the wells for (a) Saturn I and (b) Saturn II. Blue ellipses denote the position the ellipsoid when the system is at lowest energy state. Solid line denotes the wall. Dashed line denotes excluded region next to the wall. Arrows denote the gradient, which is the force the ellipsoid experiences assuming no rotation occurs.

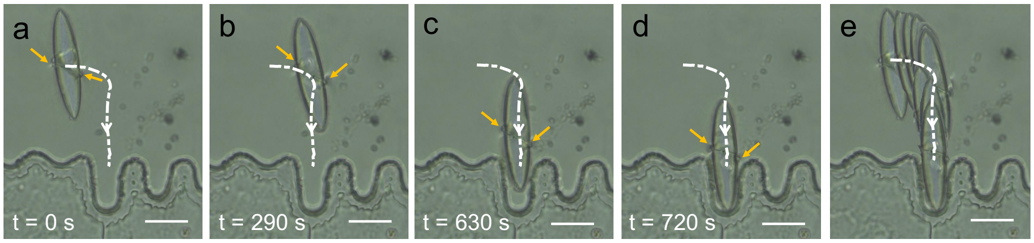

Figure 4.9: (a-d) Time-lapse images of an ellipsoid entering a deep well. The white dotted line denotes the trajectory of the COM of the migrating ellipsoid. (e) Composite image of the full trajectories of the ellipsoid. Video file of the migration can be found in Supplemental Video 3. **The yellow arrows denote the location of the defect.** The scale bars are 25 μm.

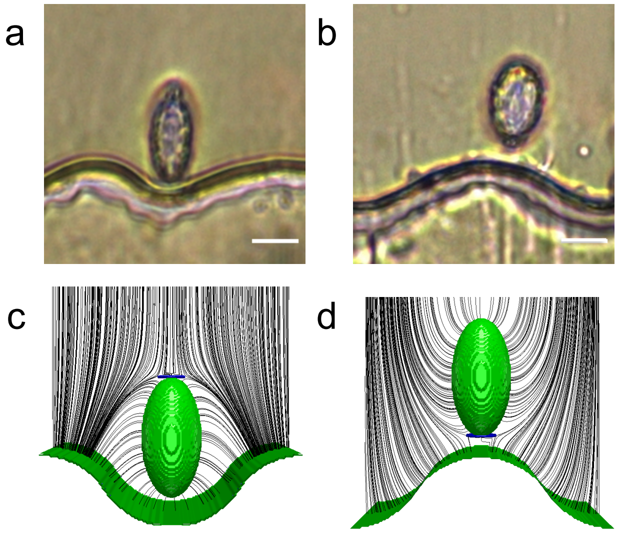

Figure 4.10: Docking behaviors of dipoles (aspect ratio $k = 2$). (a, b) Docking of dipoles when the dipole is oriented upwards in (a) and downwards in (b). The scale bars are 10 μm. (c) Simulations of the scenarios in (c)-(d) where the dipole is modeled as a small ring. Simulated colloids have semi-major axis $\alpha = 90\ nm$ and semi-minor axis $\beta = 45\ nm$.

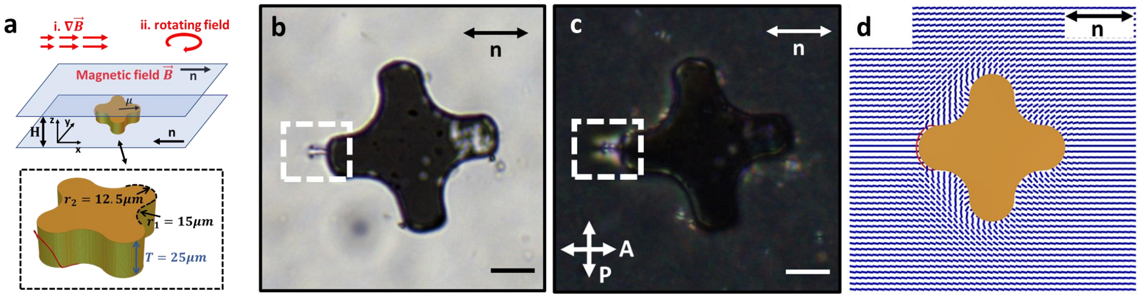

Figure 4.11: Experimental schematic (a) and static defect structure of the 4-armed micro-robot under bright field microscopy (b) crossed polarization microscopy (c) and in numerical simulation (d). The far-field director is along the horizontal direction indicated by the double headed arrows and the scale bars are 50 µm.

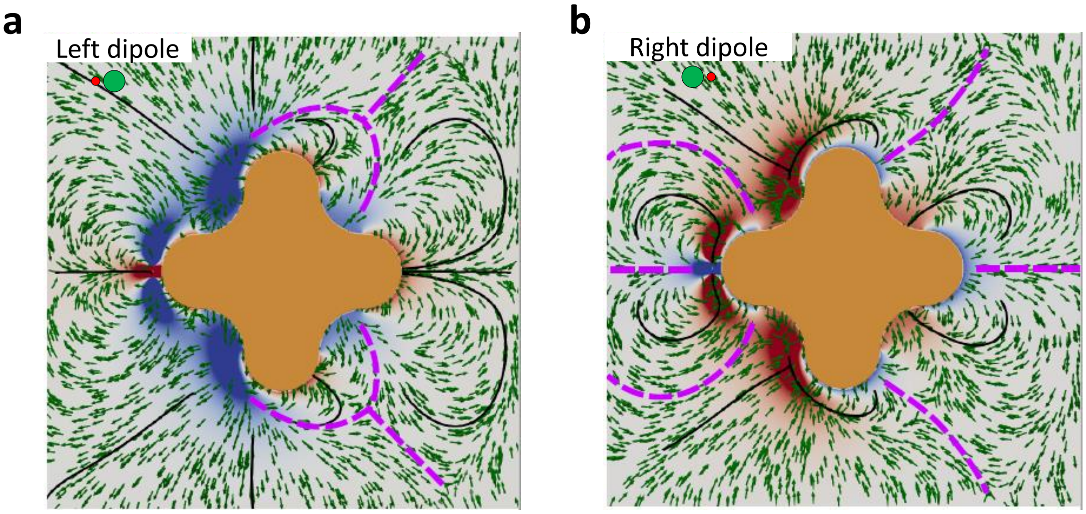

Figure 4.12: Force fields around the 4-armed micro-robot for point dipoles of left polarity (a) and right polarity (b). The underlying color maps indicated the energy field and the vector fields shown by green arrow indicates the force fields. The purple dashed lines indicate the separatrix for the trajectories of the point dipole.

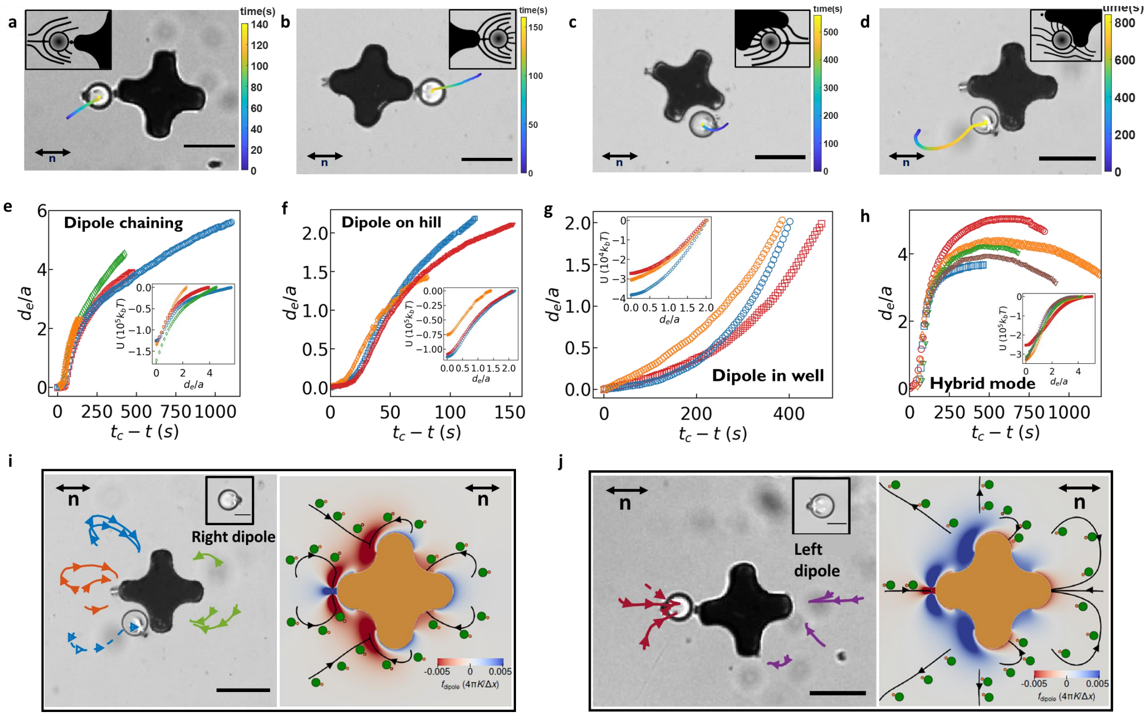

Figure 4.13: Microscopic images of different assembly configurations: dipole chaining (a), dipole on hill (b), dipole in well (c) and hybrid (d) configurations around the 4-armed micro-robot and their corresponding range of interactions (e-h) where different colors indicate different observations. The deviations between different trajectories are mainly caused by different initial relative positions of the micro-robot and passive colloid. The insets in (a)-(d) shows schematics of the director fields around the passive colloids and the insets in (e)-(h) shows the strengths of the attractive interactions, respectively. (i-j) Superposed experimentally observed trajectories of the assembled colloids (left) and corresponding numerical predictions from the calculated energy field (right) in the micro-robot fixed frame are shown for passive colloid with its hedgehog defect facing right (i) and left (j) as shown in the insets, respectively. Different colors represent different final assembly configuration: dipole chaining (red), zig-zag dipoles(orange), dipole on hill (purple), dipole in well (blue) and hybrid configuration (blue). Scale bars are 20 µm for the insets in (i) and (j) and are 50 µm otherwise.

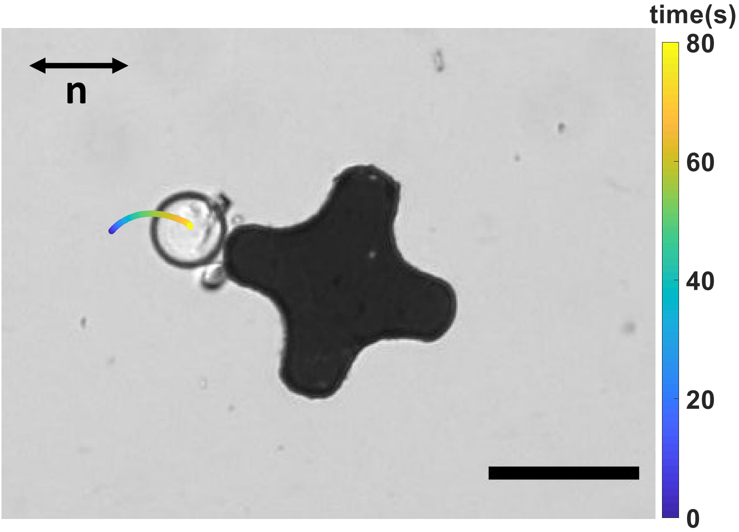

Figure 4.14: A rarely observed zigzag assembly configuration where the colloid with its defect facing the defect of the micro-robot assemble in a zigzag structure. Such assembly configuration occur only if the micro-robot is driven anbd parked with its defect really close to the defect of the passive colloid. Scale bars is 50 µm.

Chapter 5

Micro-robotics in NLCs via lock-and-key and far-from-equilibrium defect dynamics

Physically intelligent soft matter systems exploit information embedded in colloidal building blocks and their milieu to form functional structures for applications ranging from advanced optical devices [228, 229, 230] to micro-robotics [231, 20, 21, 40, 22]. To embed energy landscapes in the domain, the shape and surface anchoring conditions of colloids and domain boundaries can be designed to influence NLC orientation. Colloids within the domain distort, sense and respond to the energy landscape via emergent interactions. Such interactions can guide passive colloids to assemble with each other [204], and to be repelled from or attracted to walls of complementary shape [187, 192, 194, 195]. The introduction of active colloid dynamics dramatically expands the opportunity to sculpt such interactions and to introduce entirely new transient interactions. For example, active colloid shape and anchoring conditions can mold the local director field; repositioning of the colloid can bring this information to arbitrary sites in the domain. Furthermore, the energy landscape can be dynamically reconfigured to generate far-from-equilibrium defect structures by an interplay of the elasticity and flow in these highly non-linear fluids. These non-equilibrium structures provide new forms of mobility and interactions.

Active colloids that perform tasks are often described as micro-robots, an exciting intersection of materials science and robotics. In this chapter, we used the 4-armed ferromagnetic micro-robot described in the previous chapter to manipulate passive colloids in NLC via multiple modes of interaction. The micro-robot shape was designed to embed elastic energy in the domain and to attract passive colloids to specific sites on its surface via nematic lock-and-key interactions. Furthermore, the micro-robot's surface energies were designed to seed a companion defect which can also assemble passive colloids. These micro-robots can be actuated using external magnetic fields in NLCs to assemble passive colloids. Once assembled, the micro-robot can carry these colloids as cargo, as these interactions, which scale as $Ka \sim 10^4 - 10^5 k_B T$ are remarkably strong, where K is the Frank constant that describes the elastic energy cost to deviations from uniform alignment and a is the particle radius. Delivery of cargo, however, presents a challenge, owing to the very strength of these interactions. We find that rotation of the micro-robot using an external field generates remarkable far-from-equilibrium defect structures with complex dynamics that include sweeping motions and defect hopping. If colloids are assembled on the micro-robot, the colloids' companion defects and that of the micro-robot can merge to form shared structures. These highly non-equilibrium effects can be exploited to release assembled particles, and to deliver them to docking sites in the domain to build colloidal structures. To achieve fully autonomous control and manipulation of cargo, the rotation-induced translation we investigated in Chapter 3 is exploited for the locomotion of the micro-robot. By reversing the sense of rotation and changing rate of rotation of the external field, N-shaped and curved trajectories of the micro-robots are achieved which allows it to explore the medium and search for passive cargo. Finally, we demonstrate a complete micro-robotic cycle of cargo manipulation including approaching, assembly, transport and release using this platform we have developed in NLCs.

5.1. Transportation, defect relaxation and cargo carrying

Once the experiment cell is placed in an external magnetic field, the micro-robot can translate under a force exerted by the field gradient as shown in Fig. 5.1a. The micro-robot moved perpendicular to the far field director under a field gradient created by a permanent magnet placed close to the cell. In a period of 20 s, the micro-robot traveled a distance $\sim$ 159.6 µm, giving the average speed of $7.98\,\mu\mathrm{m\,s^{-1}}$. During the translation, the companion dipolar defect around the micro-robot was deformed and stretched by the flow. When the field was turned off, the micro-robot slowly rotate counter-clockwise to the quasi-static configuration with the dipolar defect at the tip of either arm aligned parallel to the far field director, indicated by the yellow dashed double headed arrow.

The micro-robot can be driven to find passive colloids in the domain. In the previous chapter, we have shown that when the micro-robot is placed close to passive colloids, there are several modes of assembly which depend on the colloid's initial position and orientation. Once assembled, the passive colloids could be carried as cargo as the micro-robot moves under an external magnetic field. For example, as shown in Fig 5.1b, a colloid is carried in the dipole-chaining configuration as the micro-robot moves with an average velocity of $2.9\,\mu\mathrm{m\,s^{-1}}$; as the micro-robot moves, the docked colloid oscillating around an equilibrium separation distance Fig 5.1c as the magnet is gradually moved away. In fact, passive cargo assembled in all configurations can be carried due to the strong attractive interaction in the order of $10^4 - 10^5 k_B T$ as calculated in Chapter 4. The very strength of these interactions is a potentially confounding factor to the development of micro-robotics in NLCs; while the micro-robots are excellent cargo carriers, the release of the cargo proves a challenge. This motivates our exploration of far-from-equilibrium defect structures.

5.2. Far-from-equilibrium defect dynamics

The highly non-linear elastic response of NLCs causes far-from-equilibrium defects to emerge when the micro-robot is rotated under an external torque, influenced by the structure's hybrid anchoring conditions, complex shape, and sharp edges. The dipolar loop, initially situated on the arm aligned with the far field director, extends due to the geometric frustration between the local boundary condition and far field director. Upon rotation by $\frac{\pi}{2}$ radians, the defect hops to the arm that has become aligned with the far field as shown in Fig. 5.2a. This hopping occurs via a complex mechanism in which the dipolar structure interacts with a portion of the disclination loop beneath the object. Upon cessation of rotation, the defect retracts to form a dipolar defect on the arm aligned with the director over time scales characterized by the relaxation dynamics of the system, given by $\tau = \frac{L^2\gamma_1}{K}$, where L is the characteristic length of the micro-robot, γ_1 is the rotational viscosity of NLCs. Upon slow rotation by multiples of $\frac{\pi}{2}$ radians, the defect "travels" via periodic extension, interaction, hopping and relaxation in the opposite sense of the particle's rotation. Numerical simulations (Figs. 5.2b and c) suggest that strong dynamic alignment of the director field provides pathways for rapid defect motion through the bulk phase.

Under continuous rotation at angular velocity ω that challenge the natural relaxation dynamics, the defects form smeared-out dynamic structures with periodic rearrangements that depend on the Ericksen number $Er = \omega\tau$. Under high $Er \sim 18$, for example, the defect gets significantly elongated and remains "smeared out" while hopping along the structure every $\frac{\pi}{2}$ radians determined by the geometric symmetry of the 4-armed micro-robot, lagging the alignment of the arm tips, without relaxing back to the equilibrium structure. The extent of defect elongation is positively related to Er and larger Er leads to greater defect elongation around the micro-robot which plays a very important role when interacting with passive colloids.

5.3. Cargo release and juggling

These far-from-equilibrium defect dynamics during the rotation of the micro-robot show clear evidence of director field restructuring and provide an important means to manipulate colloidal cargo. For example, an assembled colloid can be released into the bulk by defect dynamics on rotating micro-robots. When the micro-robot is rotated, its defect dynamically reconfigures and interacts with the passive colloid; this interaction can place the passive colloid in energetically unfavorable arrangements, leading to its release. Figure 5.3a (i) shows a colloid assembled in the upper left well (between arms labeled as 1 and 2) with its hedgehog defect tilted toward the nearest arm at $t = 0\,\text{s}$. When the micro-robot starts to rotate, the assembled colloid travels around the micro-robot due to steric hindrance and hydrodynamics and subsequently encounters the dynamic defect of the micro-robot at $t = 25s$ after a $\frac{3}{2}\pi$ rotation (Fig. 5.3a (ii)). The elongated disclination loop of the micro-robot merges with the hedgehog defect from the colloid. The defects form a larger loop that pulls the passive colloid with it (Fig. 5.3a (iii)). Further rotation leads to the breakdown of this merged loop and the colloid recovers its companion hedgehog defect (Fig. 5.3a (iv)). However, the passive colloids is now re-positioned on the hill of the adjacent arm with its defect point outward, and is repelled from the micro-robot (Fig. 5.3a (v)). Passive colloids assembled in other configurations can also be released by rotation via similar defect dynamics.

Two identical colloids docked on the micro-robot, can be juggled, rearranged, and restructured by similar far-from-equilibrium defect dynamics. The structure, shown in Fig. 5.3b (i), is initially at rest, and has colloid 1 (labeled as red) docked in the bottom left well with its hedgehog defect tilted toward the nearest arm, particle 2 (labeled as yellow) docked in the upper right well with its companion defect aligned with the far-field director, and the micro-robot's dipolar defect on its left arm aligned with the far-field director. As the micro-robot is rotated in the clockwise direction ($Er \sim 1 - 10$), its defect lags behind the arm, elongates and merges with the defect on colloid 1 to form a shared structure (Fig. 5.3b (ii)). This merged defect carries colloid 1, rearranging its orientation and position on the micro-robot (Fig. 5.3b (iii)). As the rotation continues, the merged defect further elongates along the sharp edges of the micro-robot, and encounters colloid 2 (Fig. 5.3b (iv)). The defect forms a larger loop containing both colloids. This larger loop also rotates and re-positions colloid 2. Finally, as shown in Fig. 5.3b (v), the merged defect loop becomes unstable, breaks down, and contracts; the micro-robot assumes the original defect structure at t=0s, and the colloids' companion hedgehog defects are restored. However, the changes in the positions and orientations of the colloids alter their ensuing interactions with the micro-robot. Colloid 1 is now stably docked in the well on the upper right side, with its hedgehog defect oriented along the director. Colloid 2, however, is oriented in an antagonistic fashion at the tip of the arm with its hedgehog defect pointing outward and is repelled from the micro-robot. Thus, colloid 1 is retained and colloid 2 moves away from $t = 77s$ to $t = 135s$ (Fig. 5.3b (vi)). The separation distance $d = r - r_{min}$, shown in Fig. 5.3c as as function of time, clearly tracks the opposite migration process for colloid 1 and colloid 2 due to the attractive and repulsive elastic interaction, respectively.

5.4. Micro-robotic directed assembly of colloidal structures

We exploit the micro-robot's ability to assemble, transport and release passive cargo to build structures by releasing these colloids near attractive sites on wavy walls. For example, a colloid in a dipole chaining configuration (Fig. 5.4a) is carried as cargo by a micro-robot and is released near an attractive well on a wavy micro-structure via rotational defect dynamics of elongation, sharing, and recovery. As the colloidal particle detaches from the micro-robot, it migrates into the attractive well (Fig. 5.4a (iii)), after which the micro-robot can be driven away to retrieve a different particle in the domain. This process can be repeated and multi-element systems can be built on the static micro-structures. Depends on the design of the attractive sites, various colloidal structures can be constructed by the serial addition of colloidal particles at particular locations as building blocks. Using a strip of wavy wall shown in Fig. 5.4a, multiple structures are constructed including a 1D colloidal lattice (Fig. 5.4b), a chain of 7 colloids (Fig. 5.4c) and a more complicated anisotropic structure (Fig. 5.4d). As our approach only depends on the surface chemistry of the passive cargo, it can be applicable to functional building blocks, e.g. silver coated silica colloids, for reconfigurable devices. Up to this point, we had used magnetic forces that relied on magnetic field gradients over length scales similar to our micro-robots. These gradients become harder to achieve as micro-robots are scaled down. However, the rotational dynamics remain robust even for colloids of sub-micron dimensions. This motivates the use of microrobot rotational dynamics for the retrieval, carrying, release and assembly of colloidal cargo, as is developed in the next section.

5.5. Trajectory planning of micro-robot and fully autonomous cargo manipulation

In Chapter 3, we established defect-propelled swimming of nematic colloids using a circular disk with the same hybrid anchoring condition as our micro-robot. As we rotate our micro-robot, similar swimming behaviors have been observed in which the translational speed and direction can be controlled by the rate and sense of rotation of the micro-robot. To demonstrate the ability to actuate and control the trajectories of the micro-robot, two types of trajectories are planned and executed as shown in Fig. 5.5. Mirror symmetric changes with respect to the axis perpendicular to the far field director can be achieved by reversing the sense of rotation of the micro-robot as shown in Fig. 5.5a. The direction of the external field of $T = 12\,\mathrm{s}$ was reversed twice at the location indicated by the red dashed lines which led to a N-shaped trajectory of the micro-robot. In a different case, as shown in Fig. 5.5b, the period of the external field was varied from $4\,\mathrm{s}$ to $8\,\mathrm{s}$ and finally to $16\,\mathrm{s}$ at the location indicated by the red dashed lines, generating a curved trajectory; this is due to different extents of defect elongation as greater elongation leads to translational direction closer to the far field director. With the ability to steer and make sharp turns while translating by purely tuning the parameters of the external field, our micro-robot is now ready for fully autonomous micro-robotic cargo manipulation.

Figure 5.6 shows a complete cycle of micro-robotic cargo manipulation using our 4-armed micro-robot under a programmable rotating magnetic field. Firstly, the micro-robot was driven toward a passive colloid, following an almost linear path of $\sim 137\,\mu\mathrm{m}$ with an average speed of $\sim 1.71\,\mu\mathrm{m\,s^{-1}}$ under an clockwise rotating external field of $T = 4\,\mathrm{s}$ (Fig. 5.6 (i)). After the micro-robot recovers its static dipolar defect, the passive colloid is attracted and migrated a distance $\sim$ 5.6 radii to form the dipole-chaining configuration (Fig. 5.6 (ii)). Note that the time the micro-robot takes to assemble the passive colloid depends on its initial separation distance and can be greatly reduced if the micro-robot is placed more closely to the passive colloid. Here, we locate the micro-robot relatively far from the colloid in order to demonstrate the range of this interaction. Once assembled, the pair was rotated counterclockwise under the same period of $T = 4\,\mathrm{s}$. During this process, the micro-robot follows a linear path, while the passive colloid followed a helical trajectory and traveled an effective distance $\sim$ 16.4 radii together with the micro-robot due to an interplay of defect-defect interaction and hydrodynamics (Fig. 5.6 (iii)). Finally, the period of the external field was reduced to $T = 20\,\mathrm{s}$ which significantly decreased the extent of defect elongation. Therefore, the attractive defect-defect interaction was weakened and the colloid was released from the micro-robot (Fig. 5.6 (iv)) which completed this fully autonomous cargo manipulation process.

5.6. Conclusions

The development of robust micro-robotic approaches for colloidal cargo manipulation is essential for a broad range of applications such as, drug delivery, bio-sensing and assembly of functional reconfigurable materials. Elastic interactions between micro-particles within NLCs are one means to address these needs. Since approaches developed in liquid crystals do not depend on the material properties of the particle, they are broadly applicable across materials platforms.

In the previous chapter, we have shown that passive particles can be assembled near a designed magnetic 4-armed micro-robot object in 5 different configurations. In this chapter, we have demonstrated that once the passive colloid is assembled, it can be carried as cargo with the micro-robot under an external field. To release cargo at desired locations, we firstly studied the defect dynamics around a rotating micro-robot without any passive particle. We have observed highly non-equilibrium defect dynamics in which the dipolar defect around the micro-robot was stretched and then merged with defect shedding from the next arm, and eventually hopped and contracted to the next arm. We attribute this rearrangement to the geometric frustration between the local boundary condition and the far-field director as the micro-robot is rotated. Similar hopping behaviors of the defect was also confirmed by numerical simulations.

Using such rotational dynamics, we have successfully released the cargo and achieved independent and simultaneous control of two colloids. During the release process, we have observed far-from-equilibrium defect interactions between the micro-robot and passive particles including merging, splitting and contraction. Furthermore, when additional attractive sites are present in the system, passive cargo can be deliberately released near those sites for

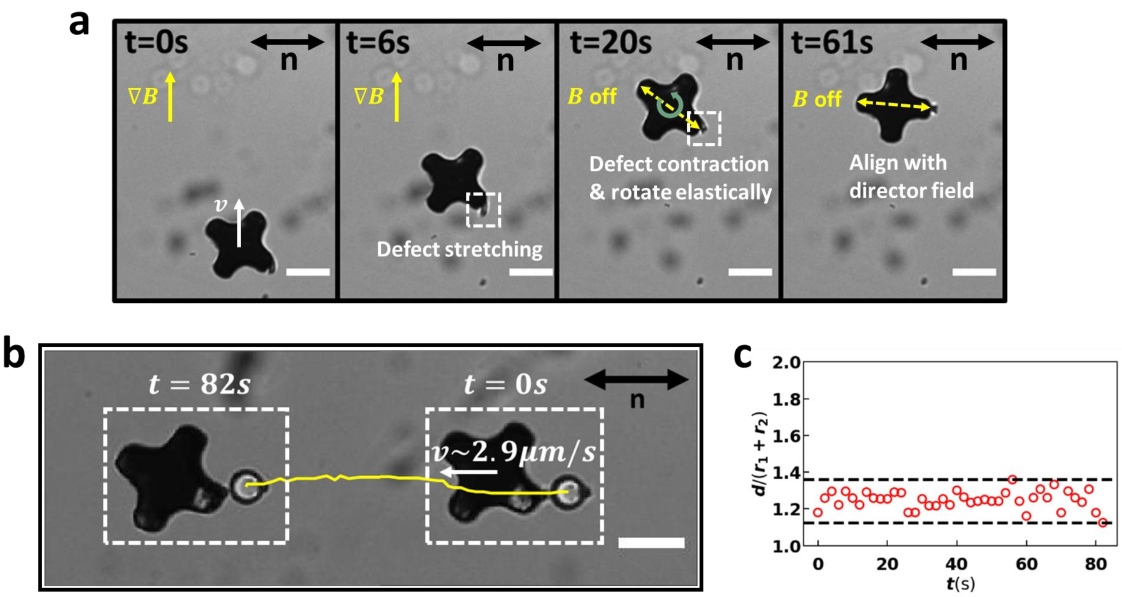

Figure 5.1: Transportation, defect relaxation and cargo carrying: (a) Time-stamped images of a micro-robot translating under a magnetic field gradient (solid yellow arrow). The white dashed box indicates the location of the defect and the dashed yellow double head arrow indicates the diagonal axis of the micro-robot on which the defect resides. (b) Superposed image of cargo carrying of a 25 µm diameter passive silica bead from t=0s to t=82s via dipole chaining configuration. The yellow curve indicates the trajectory of the cargo. (c) Normalized center-to-center distance as a function of time. d indicates the distance between centers of arm tip and the assembled colloid. r_1 and r_2 are radii of the colloid and arm tip, respectively. Scale bars are 50 µm.

targeted delivery and construction of colloidal structures. Finally, a fully autonomous cycle of cargo manipulation has been demonstrated using far-from-equilibrium defect dynamics generated purely by rotating the micro-robot and tuning the parameters of the external field. Given the ability to engineer the energy landscape in the domain, our approach opens up great opportunities for bottom up and top down material assembly for reconfigurable functional systems.

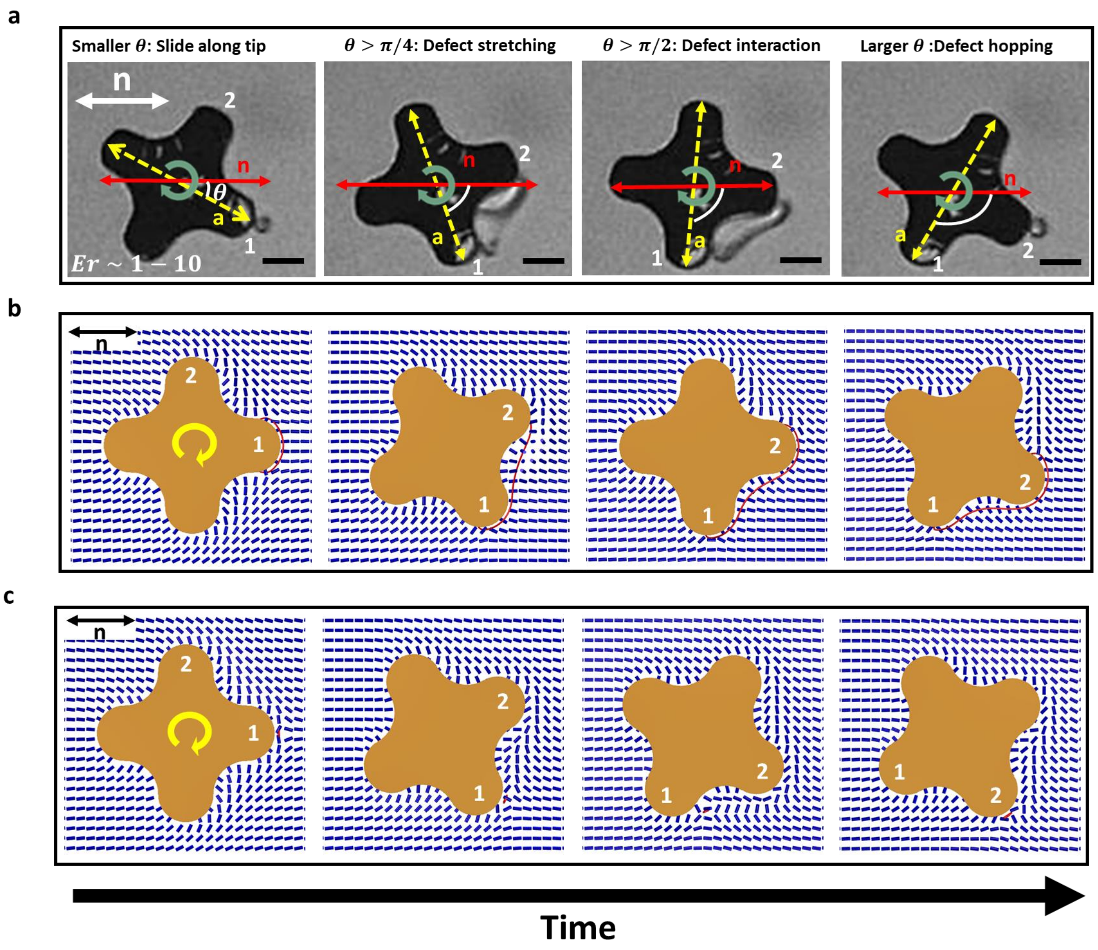

Figure 5.2: Defect hopping around the 4-armed micro-robot: Experimental time-series images (a) of defect hoping from one arm (labeled as 1) to another arm (labeled as 2) of the 4-armed micro-robot during a $\pi/2$ clockwise rotation. θ indicates the angle between the director (red arrow) and the diagonal (dashed yellow arrow) of the micro-robot. Scale bars are 20 µm. Time-series of numerical simulation of dipolar disclination loop defect (b) and a point dipolar defect (c) hopping between two arms of the 4-armed micro-robot (labeled as 1 and 2) during clockwise rotation. The red curves indicate where the defects are.

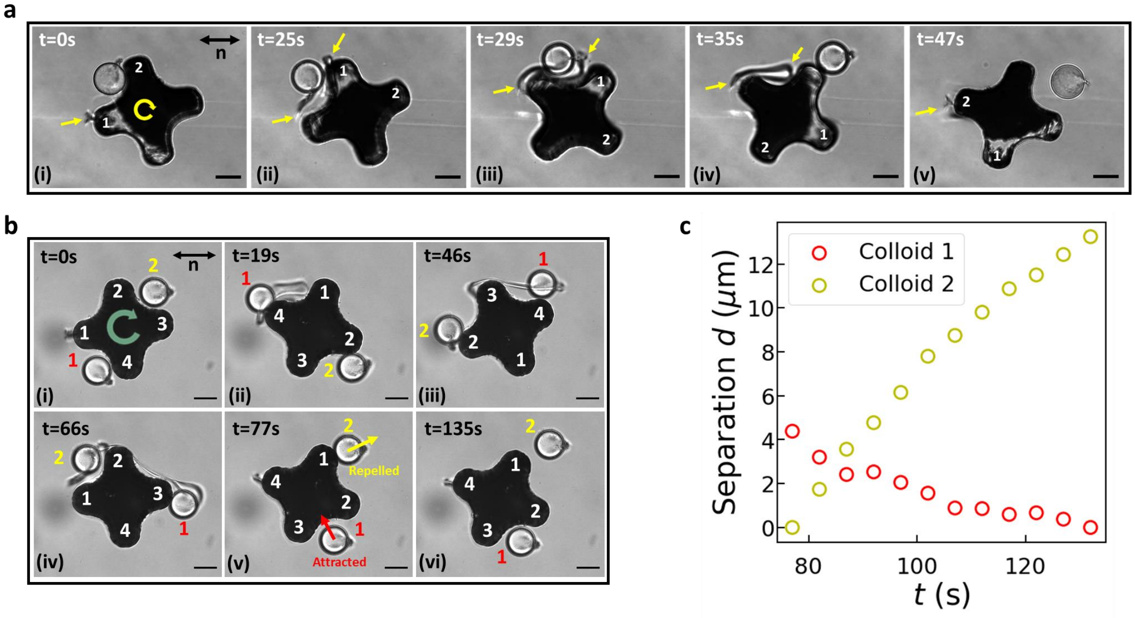

Figure 5.3: Cargo release and juggling: (a) Time-stamped images of cargo release of an assembled passive colloid between two arms of the micro-robot (labeled as 1 and 2) during clockwise rotation via dynamic defect interaction. The yellow arrows indicate the location of the (elongated) disclination loop of the micro-robot. Scale bars are 20 µm. (b) Time-stamped images of cargo juggling of two colloids (labeled as 1 and 2) during clockwise rotation of the micro-robot via dynamic defect interaction. 4 arms of the micro-robot are labeled for easier visualization. Scale bars are 20 µm.(c) Calibrated separation distance $d = r - r_{min}$ from $t = 77\,\text{s}$ to $t = 135\,\text{s}$ for colloid 1 (red circles) and colloid 2 (yellow circles).

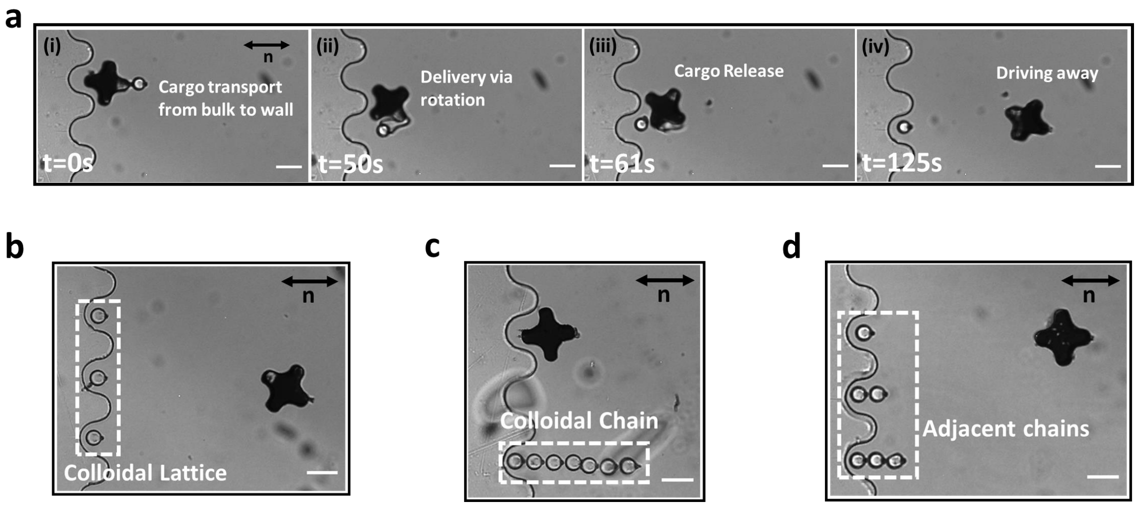

Figure 5.4: Micro-robotic directed assembly of colloidal structures: (a) Time-stamped images of micro-robotic cargo delivery process of an assembled passive colloid in the dipole chaining configuration near a wavy wall. Examples of colloidal structures built using our approach includes a 1D colloidal lattice (b), a chain of 7 colloids (c) and a more complicated anisotropic structure resembling the signal intensity symbol on cell phones (d). Scale bars are 50 µm.

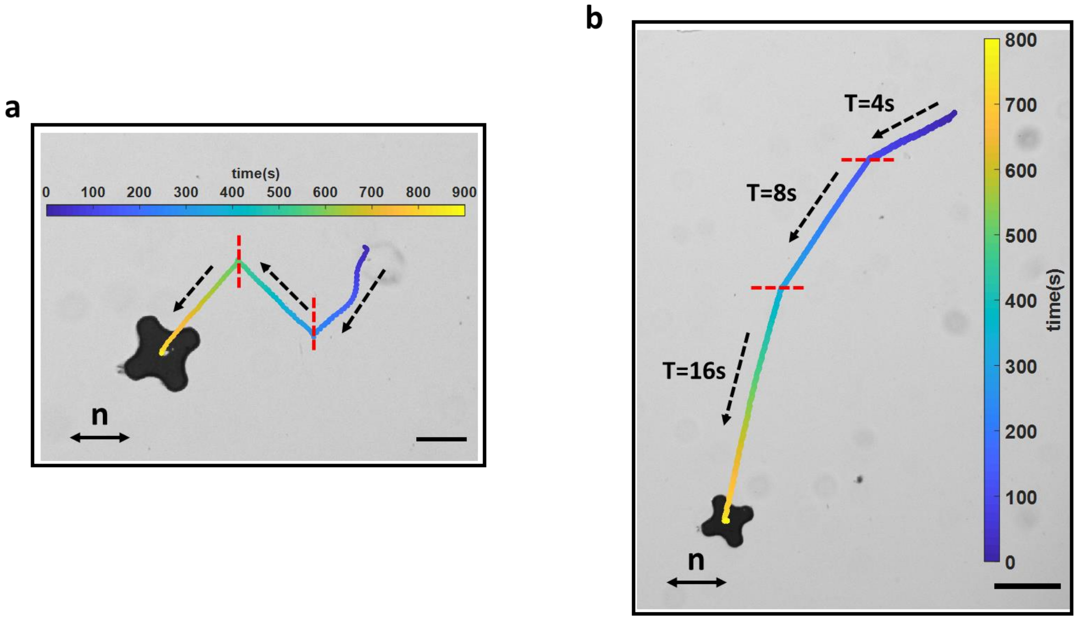

Figure 5.5: Trajectory planning of the micro-robot: (a) A N-shaped trajectory of the micro-robot achieved by reversing the sense of rotation of the external field at the locations indicated by the red dashed lines. The initial field is rotating counterclockwise with a period $T = 4\,\mathrm{s}$. (b) A curved trajectory of the micro-robot achieved by tuning the period of the external field from $T = 4\,\mathrm{s}$ to $T = 8\,\mathrm{s}$ and then from $T = 8\,\mathrm{s}$ to $T = 16\,\mathrm{s}$ at the locations indicated by the red dashed lines. For both (a) and (b), the black dashed arrows indicate the direction of the translation and the colored curved indicates the trajectory of the micro-robot as a function of time. Scale bars are 50 µm and 100 µm for (a) and (b), respectively.

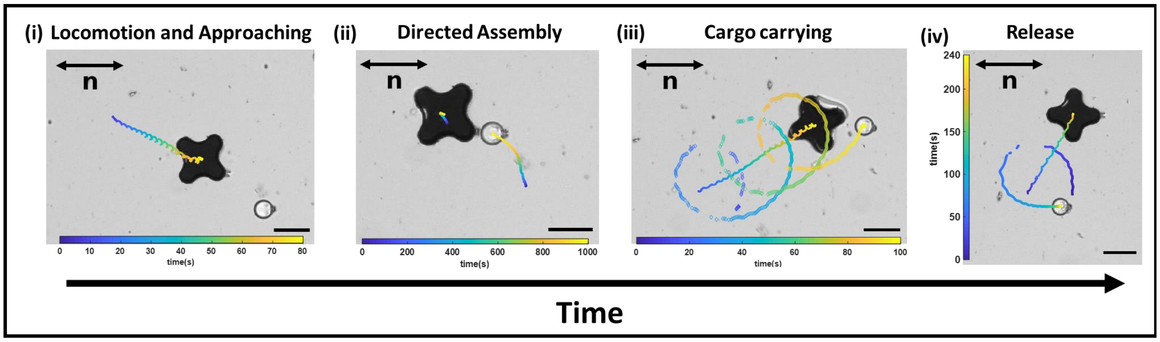

Figure 5.6: Fully autonomous cycle of cargo manipulation including (i) locomotion and approaching, (ii) directed assembly (iii) cargo carrying and (iv) release using our micro-robot. Scale bars are 50 µm.

Chapter 6

Conclusions and outlook

In this thesis, energy landscapes embedded in soft matter systems are studied as a form of physical intelligence to direct the motion of microscale objects in those systems. Using micro-robots to dynamically engineer the energy field in the domain, we have developed micro-robotic platforms for cargo manipulation on fluid interfaces and in NLCs, in which the fluid nature of these soft milieu allows colloids to move to minimize the free energy. The ability demonstrated in this thesis can be exploited for assembly of configurable structures which is of great interest in the field of material science and optics.

Micro-particles on fluid interfaces deform the interface shape, migrate, and assemble to minimize the capillary energy when trapped on a host interface with varying curvature. In the first part of my thesis, I have designed and fabricated a magnetic micro-robot as a mobile curvature source and built a magnetic control system to drive this micro-robot on the water/oil interface to interact with passive particles. To understand the interaction between the micro-robot and the passive particles, we have derived an analytical expression that describes the interplay of hydrodynamic and capillary interactions that captures the main features of experimental observations. I demonstrated directed assembly toward high curvature sites on the micro-robots and achieved multiple micro-robotic tasks including cargo carrying, desired release through rotation and cargo delivery to more attractive sites.

Micro-particles in confined nematic liquid crystals (NLCs) distort the orientation of nematogens as described in the nematic director field, generating interactions. Magnetic micro-robots are mobile distortion sources, capable of generating a broad range of interactions depending on the micro-robot shape and surface chemistry, geometric frustration of the director field, and the rate of robot motion. These interactions depend strongly on the behavior of topological defects, sites where order of the director field are lost, in the domain. To probe far-from-equilibrium effects in NLC, I have fabricated a magnetic disk with hybrid anchoring whose rotational dynamics are controlled by an external field. Upon rotation, the disk's companion defect elongates while remaining pinned on the disk's edge, peels away from the edge and sweeps across the disk's face, executing a complex swim stroke that propels disk translation. I have studied this new swimming modality in detail, emphasizing slow-rotation regimes where geometric frustration dominates and fast-rotation regimes in which the flow field and nematic order are highly coupled. In the high rotation regime, the defect elongates significantly adjacent to the disk, generating broken symmetries that allow control over disk migration direction. This ability has been exploited in path planning of the disk colloid. In addition, pair interactions of swimming disk colloids have been explored in which the defect polarity and extent of defect elongation play an important role.

Thereafter, I have designed a micro-robot with a complex four-armed shape designed to promote passive micro-particle assembly at particular sites on the robot by lock-and-key interactions or by defect interactions; the ranges and strengths of these interactions are characterized and found to be several orders of magnitude larger than thermal energies. The strength of these interactions allows colloidal cargo to remain docked on the micro-robot as it translates by action of the external field. However, this very strength also makes cargo release a challenge. We found that rotation of this micro-robot generates a complex dynamic defect-sharing event with colloidal cargo that spurs cargo release. Thereafter, I have demonstrated the ability to exploit NLC elastodynamics to construct reconfigurable colloidal structures in a micro-robotics platform in which magnetic field gradients generate micro-robot translation and rotational dynamics are exploited for cargo release. Finally, I have exploited the topological swimming modality of the four-armed micro-robot. Using rotating fields to direct the four-armed micro-robot's motion, we have achieved fully autonomous cycle of cargo manipulation including approach, assembly, transport, and release.

The ability to dynamically manipulate micro-particles and their structures in soft matter systems with embedded energy landscapes, as demonstrated in this thesis, creates new possibilities for micro-robotics and reconfigurable systems. The insights provided within this thesis not only develop the platform for micro-robotics by exploiting emergent interactions in soft matter systems but also raise fundamental open questions. In the following sections, I introduce some of the open issues and identify key extensions and concept space we plan to move forward. Those ideas are developed in collaboration with Professor Miha Ravnik and Dr. Ziğa Kos who have been performing state-of-the-art numerical simulations to help us understand experimental observations. A grant proposal covering the following ideas are currently under review to support ongoing work in the group after I graduate.

6.1. Understand the topological swimming and defect dynamics

6.1.1. Understand colloidal swimming as propelled by the topological defect

In preceding chapters, we have demonstrated topological defect-propelled swimming of nematic colloids due to periodic rearrangement of companion defect. We have proven that broken symmetries, elasticity, and disclination line pinning are essential elements for topological swimming and have identified elastic and viscous stresses that likely contribute to the translation. However, fundamental mechanistic understanding is still lacking to advance the design of colloids and their defect dynamics to enhance broken symmetry and swimmer propulsion.

We hypothesize that such far-from-equilibrium dynamics are influenced by geometric frustration, colloid features (edges/roughness/hybrid surface energies) and colloid rotation that place the system in unstable arrangements. For example, colloid rotation places the local director and defect in antagonistic arrangements with respect to the cell boundary and far field director; this geometric frustration drives edge pinning-depinning and release, an elastic instability. Defect elongation adjacent to the rotating colloid is also an instability determined by a competition between line tension and shear forces. We further hypothesize that these instabilities and their modes of release are essential elements that generate broken symmetries which drive translation.

Ongoing and future experimental and simulation analyses will relate colloid features and NLC director fields to defect instability thresholds for edge pinning/depinning and defect elongation. Observation of defect/colloid dynamics as the defects become unstable will be used to develop mechanistic understanding of the swimming dynamics. In experiment, disks of different diameter but with similar hybrid anchoring have been fabricated, and preliminary results shown in Fig. 6.1 indicate that smaller disks with similar aspect ratio translate faster than larger ones at the same Er. Those results suggests that smaller disks are more efficient swimmers. However, more systematic studies must be done to understand the roles of colloid size, curvature, and bend/splay/twist distortions on edge pinning/depinning thresholds.

Colloids with differing shapes and features including non-uniform edge curvatures (ellipses), sharp corners (triangles and squares) and broken symmetries (snow-man and pac-man shapes) can be fabricated to understand how these features influence defect reconfiguration and instabilities. Preliminary studies on static defect structures around elliptical, triangular, and square disk colloids are shown in Fig. 6.2. For an elliptical disk, the major axis of the colloid aligns with the far-field director, and the defect locates on one of the poles on the major axis (Fig. 6.2a). However, for triangular and square disks with shape edges and corners, the defect pins on one of the corners but still aligns with the director as shown in Figs. 6.2b and c. When those colloids are placed in a rotating magnetic field, they also translate with speeds comparable to that of the circular swimmer under the same field frequency (Fig. 6.3a), suggesting that the shape of the colloids make not play a major role in the rate of translation. However, as shown in Fig. 6.3b, the translational direction varies significantly comparing the circular disk and square disk which has the smallest translation angle ϕ, defined as the angle between translational direction and the director, across a broad range of frequency. We hypothesis that the straight edges and 4 sharp corners around the square enhance defect pinning and therefore promote defect elongation more significantly than the other shapes. This results in effects similar to those reported in Chapter 3 for disk colloids; more significant defect elongation leads to smaller ϕ. Roughness also plays an important role in defect pinning/depinning. A control experiment using a $2a = 8.74\,\mu\text{m}$ spherical colloid shows no apparent translation which can be investigated by varying edge and surface roughness of the magnetic particle by incorporating nanoparticles as defect pinning sites to understand their impact on these thresholds and ensuing swimming dynamics.

A more detailed study on the rate of rotation can be done to understand the balance of local shear stresses and disclination line tensions; this will enable identification of threshold Er numbers for defect elongation. These thresholds will be compared to simulation to understand the director fields and visco-nematic stresses in the vicinity of the defects. Stability analyses can be first performed on simplified geometries to understand depinning thresholds in terms of Frank free energies, edge pinning energies and disclination line tensions guided by these experiments and simulated director fields. The range and form of the flow field around the topological swimmers are not yet understood. To characterize the flow field over the entire period of rotation, we could seed the domain with passive tracer particles to measure the spatial range and form of the flow field. This would allow us to relate features of the flow to the instantaneous configuration of the elongated defect to understand the swimming mechanism and resulting 3-D flow field.

6.1.2. Understand topological defect hopping on complex shaped rotating colloids

In addition to the far-from-equilibrium defect swim strokes, defects on rotated colloids can become delocalized, moving from one preferred site to another via a hopping mechanism. As they hop, defects move rapidly adjacent to the rotating colloid, from one site to another. We have observed this only for colloids with invaginated structures like the four-armed structure described in Chapter 5; the dipolar defect loop at rest resides on one of the arm tips aligned with the director field and moves from tip to tip as the structure rotates. Preliminary simulations suggest that strong dynamic alignment of the director field provides pathways for rapid defect motion through the bulk phase. In addition to their fundamental interest, such invaginated structures allow nematic colloidal lock-and-key interactions, related to those on wavy walls [192, 194], in which colloids nest in curved sites to minimize distortions in the domains. While colloid capture is straightforward, release is a challenge. Defect hopping provides a means to restructure the director field and, thereby, releasing the colloidal cargo. We hypothesize that hopping is a distinct instability from the "swim stroke" shown in Chapter 3, which relies on the defect growing along and peeling away from the disk's edges. Rather, we hypothesize that hopping occurs by motion through the NLC adjacent to the colloid and relies on the presence of protrusions and invaginations in the colloid shape. Studies to understand this hopping instability could focus on the roles of the colloid's sharp edges and invaginated curved features using particles with multi-armed structures as shown in Fig. 6.4(a). The angles between the arms of those structure could be varied to introduce asymmetry and study the periodicity of the hopping. We could also vary the pitch length to probe how pitch lengths larger, comparable to, and smaller than the colloid and cell thickness impact defect instabilities and dynamics. The occurrence of defect hopping, its periodicity, and its relationship to the symmetries of the particles (e.g., boomerang, 3-armed and 4-armed rotated colloids) and the far field director alignment could be probed as a function of colloid shape and rotation rate. Preliminary experiments on rotated triangular and square shaped active colloids with straight sides do not exhibit defect hopping; the invaginated curved zones between the active colloid's arms appear to be essential to this phenomenon.

6.1.3. Explore topological swimmer genus and chiral liquid crystals (CLCs)

In has been previously shown in our group that by strategically placing holes on nematic colloids, additional topological defect can be formed near the colloid and direct the assembly of passive colloids [232]. It would be interesting to use such effects to influence and perhaps increase the broken symmetry of the system essential to swimming. In such a study, one could fabricate and rotate higher genus colloids as shown in Fig. 6.4(b) to generate defect instabilities and interactions between the defects on the rotating colloid (self-defect interactions). These interactions could be used to influence the swim stroke and the broken symmetries in elastoviscous stresses that propel colloid motion. In addition, those deliberately seeded defects could serve as extra assembly sites for cargo micro-manipulation to further explore more micro-robotic functionalities.

It would also be interesting to probe the addition of chiral dopants that promote the formation of CLC phases [233] which can give extra degrees of freedom when probing defect dynamics; CLCs form twisted helical structures with tunable pitch length. The introduction of the additional length scale, along with CLC's highly anisotropic elastic and viscous responses, which differ from those in NLCs, may yield additional means to shape non-equilibrium defect dynamics and dictate broken symmetries. In a recent study, our group has successfully demonstrated similar lock-and-key interactions in CLCs near a wavy well but with richer behaviors as cholesteric pitch competes with the other length scales in the system [234]. One could add chiral dopants that promote intrinsic twist distortions in CLCs and study the effects of cholesteric pitch on geometric frustration and viscous responses of the nematic swimmer system.

6.2. Understand topological swimmer pairs and topological swimmer-passive disclination line interactions

6.2.1. Understand topological swimmer pair interactions with and without defect sharing

As discussed in Chapter 3, dynamically elongated topological defect structures allow new kinds of dynamic interaction. For example, neighboring disk colloids with dipolar defects of similar polarity can move with separate elongated defect, allowing them to co-migrate without dimerizing. Alternatively, the elongated defect on neighboring colloids can merge to generate dynamic dimers, in which each swimmer follows a curvilinear trajectory; these dimers have enhanced broken symmetry and translate strongly. On the other hand, dimers of opposite polarity become more symmetric and translate weakly. We hypothesize that the strength and consequences of pair interactions depend on whether the far-from-equilibrium defects remain distinct or whether they merge to form shared entities which depend strongly on the extent of defect elongation. We also hypothesize that dimers of different broken symmetries can generate rotating structures that remain fixed in space or dimers that show enhanced translation.

Future work will focus on dimer swimming as a function of defect polarity, swimmer geometry, and initial configuration with respect to the far field director and rotation rate. The rotation rate determines the length of the extended defects and therefore their propensity to entangle and merge under rotation. In such a study, one could observe shared defect configuration as a function of rotational Er to identify thresholds for defect interaction and conditions that lead to broken symmetries. Preliminary results have focused on pairs of equal sized disks. Disks of unequal size or rotating colloids of different shape, including ellipsoids and triangles, could be investigated to enhance broken symmetry and determine how shared defects between asymmetric particles alter broken symmetries and dimer mobility. Colloids of higher genus with multiple defects and their effects on dimer (a)symmetry will also be studied. Interesting cases that emerge from the exploration of defect dynamics in CLC could also be explored for dimer formation.

6.2.2. Understand the dynamics of defect sharing between rotated colloids and disclination lines

Passive disclination lines can be seeded and stabilized in a NLCs domain using microstructures or antagonistic anchoring boundaries [209, 213, 214]. These passive disclination lines are attractive sites for nematic colloids and, therefore, can be used to direct the assembly of passive colloid. So far, reconfiguration of passive disclination lines is mainly achieved using external fields such as flow or electric field which affect the entire domain. Local manipulation of disclination line has remained largely explored. While colloids moved by laser tweezers have been used like ‘point forces’ to weakly distort disclination lines [235], we propose that colloid rotation and translation can be used to interact with passive disclination lines in the domain, and we propose to study interactions between the dynamic defect on the active colloid and passive disclination lines. One could study these interactions as a function of Er to understand when the rotating colloids remain associated with and extend the disclination line or when they can release the filaments to allow them to contract. Such research would pave the way to new cargo manipulation approach in NLCs in which these passive disclination lines are dynamically reconfigured by active colloids and developed as mobile trapping sites for passive cargo capture. Future work could also study the most interesting aspects of the colloids with different genus and the responses in CLC. For example, if the particles with higher genus yield shared or entangled defect structures with interesting thresholds and broken symmetries, one could place them in interaction with the disclination lines. The presence of additional whipping defects might enhance the trapping or escape from the disclination line.

6.3. Study passive colloidal cargo in far-from-equilibrium defects

6.3.1. Defect interactions between active and passive colloids

In Chapter 5, we have shown that the 4-armed micro-robots can collect passive colloidal cargo by nematic lock and key interactions and dipole-dipole interactions; at rest, the passive colloids remain bound to the micro-robot by elastic interactions. Upon rotation, the companion defect of the micro-robot undergoes periodic rearrangements and hops between the micro-robot's arms. Once this traveling defect encounters the assembled passive colloid with a hedgehog defect, it merges with the hedgehog and forms a larger disclination loop. Upon continued rotation, this loop splits and contracts, and the passive colloid recovers its hedgehog defect. Although such defect interactions have been explored as a means to release assembled colloid, the mechanism of such defect merging and splitting remains to be elucidated. For example, key questions regarding reversibility of defect reformation (will the passive colloid always recover its original defect structure after splitting?), and whether there is material exchange between the defects during the merging process are to be answered.

6.3.2. Passive cargo capture and release on topological filaments

The disclination line on the micro-robot with assembled objects can get highly elongated as the micro-robot translate. For example, as shown in Fig. 6.5, the disclination line from the micro-robot can stay pinned on the passive colloid (Fig. 6.5a) or chains of colloids (Fig. 6.5b) even after the micro-robot has been moved away significantly. Upon cessation of the motion, this elongated disclination line formed on the micro-robot contracts due to elastic tension and tows the object at the other end in the domain like a fishing line. The merged disclination line in Fig. 6.5a eventually breaks down, and the passive colloid recovers its hedgehog defect and docks on the micro-robot in the hybrid configuration discussed in Chapter 5. We hypothesize that elongation of disclination line is influenced by backflow caused by the motion of the micro-robot and surface roughness of the passive object. Passive colloid assembly on dynamic disclination line filaments that are deformed by the movement of swimming colloids could be studied. Colloids with designed surface roughness could be used to promote disclination line pinning. The micro-robot's speed could be varied to investigate hydrodynamic/elastic interactions between the passive colloids and the filaments and their relationship to passive cargo retention and structure formation. Interaction range and type in the three-dimensional director field near these dynamic filaments could be characterized using particle tracking, polarization microscopy, and simulation to understand how local flow, geometric frustration, and rate of extension alter the director field around the filaments as they extend and contract.

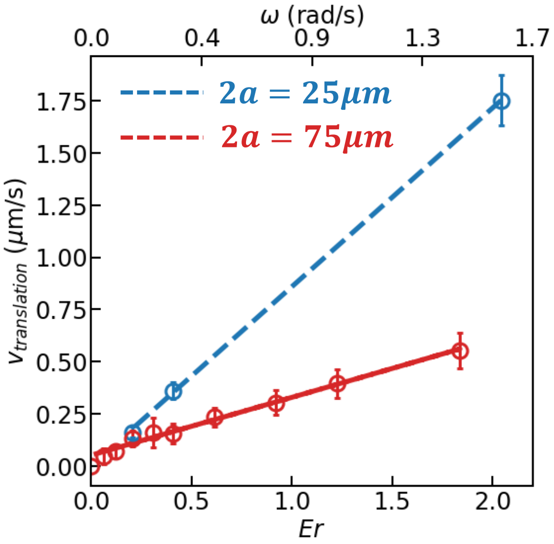

Figure 6.1: Comparison of translational speeds of $2a = 25\,\mu\text{m}$ disk colloids (blue) and $2a = 25\,\mu\text{m}$ disk colloids (red) at different Er

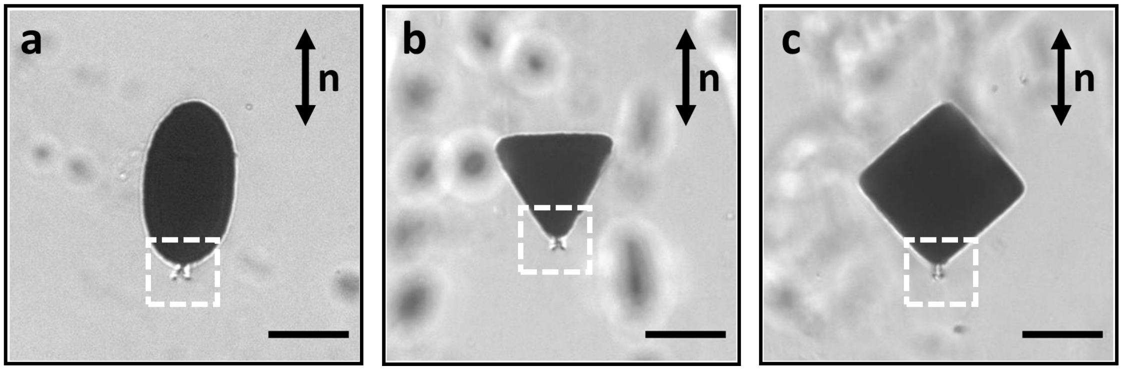

Figure 6.2: Static defect structures around (a) elliptical disk of major axis $2a$=100 µm and minor axis $2b$=100 µm, (b) triangular disk of side length 75 µm and (c) square disk of side length 75 µm. The white dashed boxes indicate where the defect locate around the colloids. Scale bars are 50 µm.

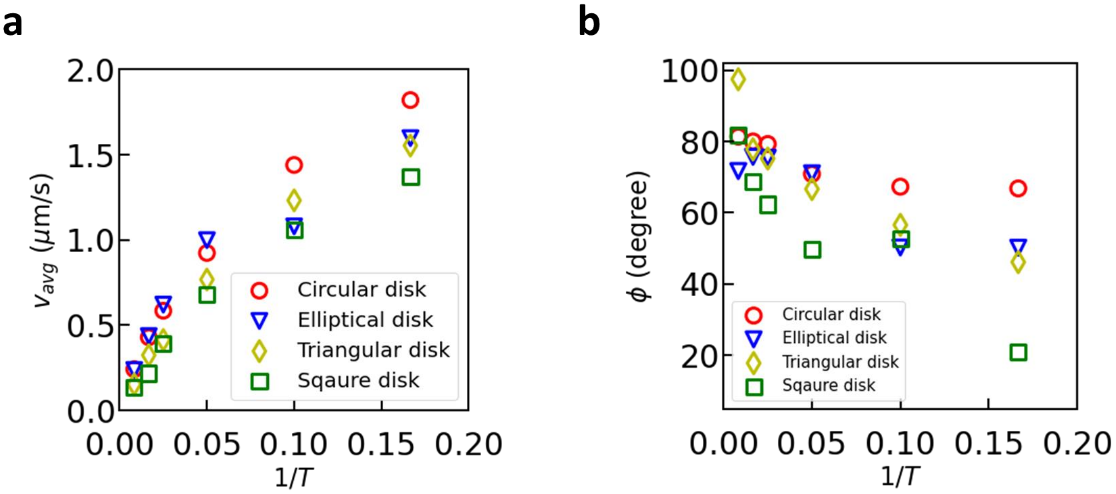

Figure 6.3: (a) Translational speed and (b) direction of the defect-propelled nematic colloids of different shapes (red circles: circular disks of $2a$=75 µm; blue triangles: elliptical disk of major axis $2a$=100 µm and minor axis $2b$=100 µm; Yellow diamonds: triangular disk of side length 75 µm; green square: square disk of side length 75 µm) as a function of frequency of the external field $\frac{1}{T}$.

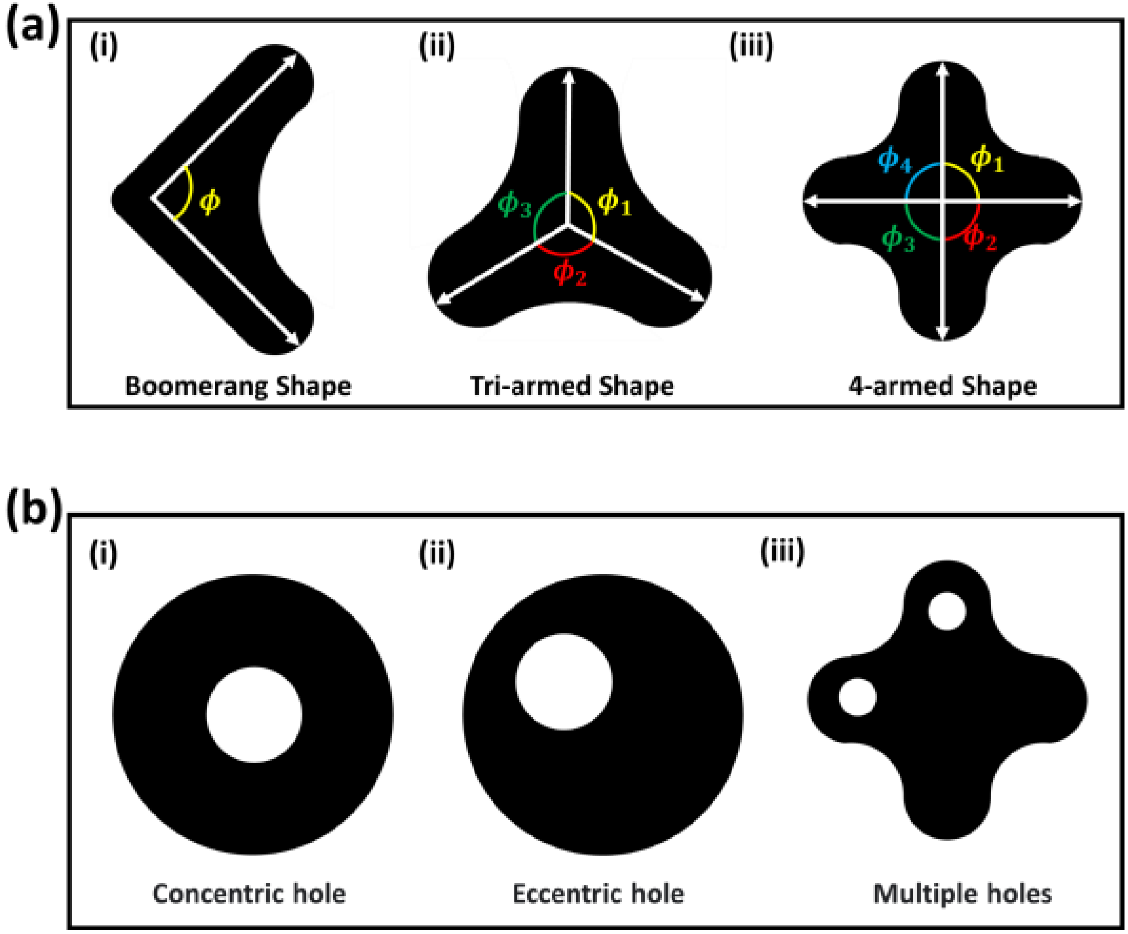

Figure 6.4: (a) Multi-armed structures: Boomerang (i), tri-armed (ii) and 4-armed (iii) with tunable angles ϕ between axis of their arms and (b) higher genus structures with a concentric hole (i), an eccentric hole (ii) and multiple holes (iii) to study the hopping behavior and of the defect and introduce additional disclination lines around rotating objects.

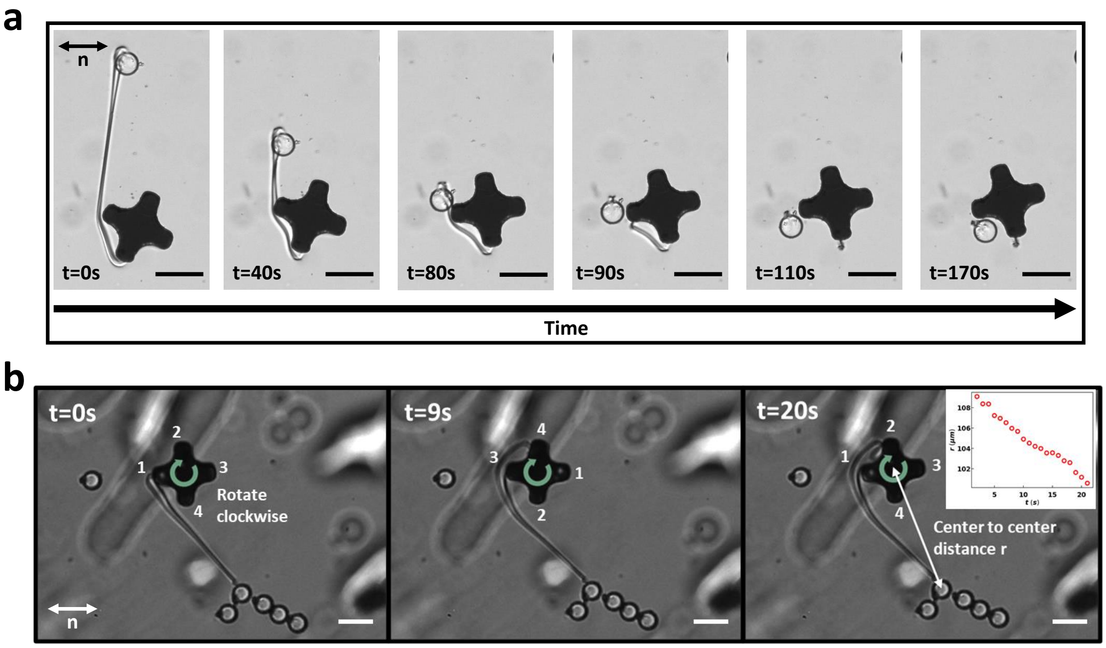

Figure 6.5: The elongated disclination line of the micro-robot tows a passive colloid (a) and a chain of passive colloids (b), which are pulled in by discliantion line contraction. Inset in (b) shows the center to center distance r as a function time, indicating the chain of passive colloid is being towed toward the micro-robot.

APPENDIXA. Interactions between micro-robot and passive particles at oil/water interface

As I have briefly discussed in Chapter 2, there is also hydrodynamics interaction between the moving microrobot and passive particles at oil/water interface in Stokes flow. In this appendix, I will first describe the fundamentals of micro-hydrodynamics and then focus on the following problems:

1. Hydrodynamic drag on particles in the bulk and trapped at fluid interface.

2. Stokeslet solution for flow field far from the micro-robot.

3. Hydrodynamic pair interaction in the near field- Faxen's law, method of reflection and

4. Competition between hydrodynamic and capillary interaction.

Let's start with Stokes equations for creeping flow which is the case for my system. Creeping flow or Stokes flow is a type of fluid flow where inertial forces are small compared with viscous forces. The Reynolds number is small. This is a typical situation in flows where the fluid velocities are very slow, the viscosities are very large, or the length-scales of the flow are very small. The stokes equation is for Stokes flow is derived in detail in Appendix A and the non-dimensional form is given as Eqns B.1 and B.2:

$$0 = -\nabla' P + \nabla'^2 \mathbf{v}' \tag{A.1}$$

$$\nabla' \cdot \mathbf{v}' = 0 \tag{A.2}$$

where P' is the nondimensional modified pressure and $\mathbf{v}'$ is the nondimensional velocity. The Stokes equations are the bases for solving complex problem with particles present in the flow field which will be discussed in detail later in this appendix.

A.1. Viscous drag from the fluid

When a colloid is moving relative to a fluid, it experience a drag force in the opposite direction of its motion exerted by the fluid. Similarly, when colloids are trapped and translating at a fluid-fluid interface as my micro-robots and passive particles, they also experience a drag from both fluid phases. The presence of the interface results in a more complicated expression for the drag which competes with the capillary interactions between my micro-robot and passive particles.

To begin with, I first consider the simplest case of a uniform flow past a solid sphere. The slow motion of a solid sphere relative to a stagnant, viscous fluid, first analyzed by Stokes [236], is the most widely known problem in low Reynolds number hydrodynamics. Suppose we have a sphere of radius R is stationary and the fluid far away is moving at a uniform velocity $\mathbf{U} = U\mathbf{e_z}$ as shown in Fig. A.1 and we would like to determine the velocity, the pressure and the drag on the sphere, given that $Re = \frac{UR}{v} \ll 1$.

Here, I adopt the stream function solutions for Stokes equation and calculated the drag on the sphere and the final expression for the drag is shown in Eq. B.3.

$$F_D = 6\pi\mu UR \tag{A.3}$$

Equation B.3 is known as the Stokes' law and it describes the frictional force – also called drag force – exerted on spherical objects with very small Reynolds numbers in a viscous fluid.

A.2. Drag at the interface

For a particle trapped at fluid-fluid interface, the simplest case which has been studied is the case of an isolated sphere moving steadily along a flat interface with velocity U between two immiscible fluid, for example oil or air with viscosity μ_o on top of water with viscosity μ_w, in Stokes flow. For this case, the hydrodynamic resistance F_drag for a sphere with radius a is given in term of a translational drag resistance coefficient f [151] as

$$F_d = 6\pi\mu_0 a f(d/a, \kappa)U, \tag{A.4}$$

where d is the immersion depth into the water phase, $\kappa = \mu_w/\mu_o$ is the viscosity ratio, and the limit $d/a \rightarrow \pm\infty$ corresponds to the resistance of a particle in an infinite liquid of either adjoining phase as described by Stokes's law in Eq. B.3.

As for the drag coefficient f, both numerical and experimental methods have been applied to calculate f for single particles trapped at interface. Danov et al. [237, 238] conducted numerical calculations of f under Stokes flow assumptions at a flat air-liquid interface and more generally on a spherical surface with arbitrary viscosity ratio. These calculations were extended by Pozrikidis to include shear flow in the bounding phase [239].

Meanwhile, experimental studies have been done to measure drag on isolated spheres forced to move along a surface by capillary or magnetic forces. To compare the drag to the theoretical predictions, the contact angle or the immersion depth is also required. For large particles ($2a \sim 1mm$), the contact angle can be measured directly from images taken by goniometer. For smaller particles, other techniques such as gel trapping, and interferometry have been developed [149]. Petkov et al. [240] tracked the trajectory and calculated velocity of single glass beads (of submillimeter radius) as they migrate along an air-water meniscus formed at a Teflon barrier by capillarity. Contact angles were measured directly by visualization. On the basis of the values of the contact angle and corresponding capillary force, a theoretical particle trajectory was simulated as a function of time and comparison with the experimental data yielded the Stokes drag coefficient f, which was in very good agreement with the theoretical predictions in [237, 238]. Similarly, Vassileva et al. [241] experimentally measured f for single submillimeter-sized glass particles placed at a pentadecane/glycerol-water interface in which the viscosities of the oil and the aqueous phase were matched. The contact angles were measured by direct visualization, and the particle pairs interacted with each other by capillary attractive forces. Comparison of the experimental trajectories with the simulations yielded a value of f slightly larger than the theoretical prediction in [238]. Ally et al. [242] floated isolated polystyrene particles (a few microns in radius) embedded with magnetite at a planar water/air and silicone oil/air interface and applied a measured lateral magnetic field to move the particles. Contact angles were measured using film trapping and interferometry, and from comparisons of the measured trajectories with the simulation values of the isolated drag coefficient f were obtained in very good agreement with theory. The fairly good agreement of the theoretical predictions for the trajectories with the experiments indicates that the effect of the meniscus around the particles, which is not included in the theory for the drag, is not very significant for single particle. With all the studies above, it is proved that Eq. B.4 is a good correction for the drag calculation for single spherical particle moving at fluid-fluid interface under Stokes flow.

A.3. Pairwise hydrodynamic interaction between approaching particles

As I have shown previously, the hydrodynamic drag experienced by an isolated single particle moving at fluid-fluid under the Stokes flow assumption is express as Eq. B.4 in which the drag resistance coefficient f corrects for the presence of interface. Pair hydrodynamic interaction between approaching particles are more complicated since it involves the extra resistance due to the fluid drainage between the particles. Again, I first consider the simplest model where two identical spheres are trapped at an interface and moving along their line of center. Although direct theoretical calculation of the drag has not been done, experiment on this interaction have been undertaken by Vassileva et al. [241]. They used an approximate expression for the hydrodynamic resistance in which the single particle drag was multiplied by the drag coefficient for two particles in a continuous phase approaching one another. The expression is shown as

$$F_d = 6\pi\mu_0 a f(d/a, \kappa) G^{-1}(l/a) U, \tag{A.5}$$

where $G(l/a)$ is the mobility function for two spheres approaching one another in a continuous phase. For $G(l/a)$, Vassileva used the expression in [243] and by comparing the experiments to the simulations, they found a value of $f(d/a, \kappa = 1)$ equal to 1.2. Similarly, two particle capillary attraction experiments were undertaken by Dalbe et al. [244] for millimeter-sized polyethylene and nylon spheres at the air/glycerol-water interface with direct measurement of contact angles. Using the same expression for the drag to simulate the trajectories, these authors compared theory and experiment by setting $f = 1$ for all sphere sizes and wetting angles and found qualitative agreement, as they did not account for the dependence of f on the immersion depth. Boneva et al. [245, 246] considered the motion of two submillimeter-sized hydrophobized glass colloids (charged and uncharged) under the influence of electrostatic and capillary attractive forces at a tetradecane-water interface and measured contact angles directly by visualization. They used a single particle wetted area approximation for the isolated drag and a mobility function derived from the bispherical solution for two spheres approaching each other in a continuous viscous phase. They found reasonable agreement for uncharged particles, although the experimental drag was larger than the theoretical prediction due to the effect of the meniscus around the particles. For the charged particles, comparison of theory and experiment demonstrated the contribution of the electrostatic induced capillary attraction alongside the gravity-induced attraction. Those studies examine, in more detail, the pairwise hydrodynamic interaction of two colloids trapped at an interface and moving along their line of center, and the validity of the multiplicative approximating formulas for Stokes drag for this motion. To be more specific, the experimental validation of this formulation by Vassileva and Boneva were for an oil/water interface whose viscosity ratio κ was one or nearly one. For this case, the drag resistance coefficient is not sensitive to the immersion depth and its values fell into the range between 1 and 1.1. Later, Archit et.al. [151] did both numerical and experimental studies for system where the viscosity of oil on top is much larger than that of the water phase below. They derived the analytical expression for drag resistance coefficient f with the help of solutions of Stokes equation in toroidal coordinates and also used Boneva's expression for $G(l/a)$ in [246]. Experiments showed good agreement with the theoretical prediction using their analytical solution for f. One interesting phenomenon that Archit observed in their experiment is that at short separation ($l/a \sim 3-4$) show that the velocity begins to decrease, as the hydrodynamics resistance overwhelms the increase in capillary interaction.

In my experiments shown in chapter 2, both micro-robot and passive colloids are trapped at hexadecane/water interface and the micro-robot is moving toward a smaller passive particle under external magnetic field. Take the circular micro-robot as an example, tracking of the relative position of the two gives approach velocity as shown in red circles in Fig. 2.5(e). Similar to what Archit had observed, there is also a decrease in velocity as the micro-robot is approaching the passive particle. If there are no hydrodynamic interactions, as the micro-robot moving close to the particle, the velocity will keep increasing because of the increasing capillary attraction between the pair. Thus, it is obvious that hydrodynamics between the two objects is playing a role and it dominates at some range and, as a result, causes the decrease in the relative velocity. In order to understand the hydrodynamics between the two, the next step is to figure out the flow field a moving micro-robot creates at the interface since the drag experienced by the passive particle depends strongly on the velocity field of the fluid.

A.4. Point force solutions — the Stokeslet

A fundamental solution for Stokes' flow corresponds to the force $\mathbf{F}$ acting on the fluid at the origin $r = 0$. It satisfies

$$\nabla P = \mu \nabla^2 \mathbf{v} + \delta(\mathbf{r})\mathbf{F}, \tag{A.6}$$

$$\nabla \cdot \mathbf{v} = 0, \tag{A.7}$$

together with condition that $\mathbf{v} \to 0$ and $P \to 0$ as $r \to \infty$. The product of the Dirac delta and $\mathbf{F}$ in Eq. B.6 represents a force per unit volume acting on the fluid. The point-force solution for Eqns. B.6 and B.7 is called the stokeslet and is given in many textbooks [247, 248, 2] as

$$\mathbf{v}(\mathbf{r}) = \frac{1}{8\pi\mu}(\frac{\mathbf{delta}}{r} + \frac{\mathbf{rr}}{r^3}) \cdot \mathbf{F} = \mathbf{\Lambda}(\mathbf{r}) \cdot \mathbf{F}, \tag{A.8}$$

$$P(\mathbf{r}) = \frac{1}{r\pi r^3}\mathbf{r} \cdot \mathbf{F}. \tag{A.9}$$

The multiplier of the force in Eq. B.8,

$$\mathbf{\Lambda}(\mathbf{r}) = \frac{1}{8\pi\mu}(\frac{\delta}{r} + \frac{\mathbf{rr}}{r^3}), r = |\mathbf{r}| \tag{A.10}$$

is the Oseen tensor. It is important to note that the stokeslet solution represents only the disturbance caused by the force **F**; there is often an unperturbed or base velocity and pressure filed to which such disturbance must be added.

A relative simple way to derive the Stokeslet is to examine the solution to Stokes' problem (flow past a sphere) for a vanishingly small sphere (i.e. for $R \to 0$). Discarding the leading terms correspond to the unperturbed velocity for from the sphere, the velocity disturbance from the point force is

$$v_r(r,\theta) = -Ucos\theta[\frac{3}{2}(\frac{R}{r}) - \frac{1}{2}(\frac{R}{r})^3], \tag{A.11}$$

$$v_\theta(r,\theta) = Usin\theta[\frac{3}{4}(\frac{R}{r}) + \frac{1}{4}(\frac{R}{r})^3]. \tag{A.12}$$

Using Stokes' law to relate R to U and to the drag gives

$$R = -\frac{F_Z}{6\pi\mu U} \tag{A.13}$$

The minus sign is needed since F is the force exerted on the fluid by the sphere. That is, $F_z = -F_{drag}$, where F_{drag} is the hydrodynamic drag given by Stokes's law by Eq. B.3. Using Eq. B.13 to rewrite the terms involving the polar coordinate r in Eqs. B.11 and B.12, it is found that $\frac{R}{r} = -\frac{F_Z}{6\pi\mu Ur}$, $(\frac{R}{r})^3 = -\frac{F_Z}{6\pi\mu Ur}(\frac{R}{r})^2$. As $R \to 0$ with F_Z remaining constant, the linear term is unaffected and the cubic one vanishes. Thus, combining Eqs. B.11 and B.12, the velocity disturbance caused by a point force is

$$\mathbf{v}(r,\theta) = -\frac{F_Z}{8\pi\mu r}(2cos\theta\mathbf{e_r} - sin\theta\mathbf{e}_\theta) \tag{A.14}$$

which is based on a spherical coordinate system. To get a more universal form, I convert $\mathbf{e_r}$ and $\mathbf{e}_\theta$ to rectangular base vector using

$$\mathbf{e_r} = sin\theta cos\phi\mathbf{e_x} + sin\theta sin\phi\mathbf{e_y} + cos\theta\mathbf{e_z}, \tag{A.15}$$

$$\mathbf{e}_\theta = cos\theta cos\phi\mathbf{e_x} + cos\theta sin\phi\mathbf{e_y} - sin\theta\mathbf{e_z}, \tag{A.16}$$

and $cos\theta = \frac{z}{r}$, $\frac{x}{rsin\theta} = cos\phi$, $\frac{y}{rsin\theta} = sin\phi$. Eq. B.14 can be rewritten into

$$\begin{aligned}\mathbf{v} &= \frac{F_Z}{8\pi\mu r}[\frac{z}{r}\frac{x}{r}\mathbf{e_x} + \frac{z}{r}\frac{y}{r}\mathbf{e_y} + (1+\frac{z^2}{r^2})\mathbf{e_z}] = \frac{F_Z}{8\pi\mu r}[\frac{z}{r^2}x\mathbf{e_x} + \frac{z}{r^2}y\mathbf{e_y} + \frac{z}{r^2}z\mathbf{e_z} + \mathbf{e_z}] \\ &= \frac{F_Z}{8\pi\mu r}[\frac{z}{r^2}(x\mathbf{e_x} + y\mathbf{e_y} + z\mathbf{e_z})] = \frac{F_Z}{8\pi\mu r}[\frac{z}{r^2}\mathbf{r} + \mathbf{e_z}] = \frac{F_Z}{8\pi\mu}[\frac{z}{r^3}\mathbf{r} + \frac{\mathbf{e_z}}{r}].\end{aligned} \tag{A.17}$$

Since $zF_z\mathbf{r} = (\mathbf{r}\cdot\mathbf{F})\mathbf{r} = \mathbf{rr}\cdot\mathbf{F}$ and $\mathbf{F} = F_z\mathbf{e_z}$, Eq. B.15 is reduced to

$$\mathbf{v}(\mathbf{r}) = \frac{1}{8\pi\mu}(\frac{\boldsymbol{\delta}}{r} + \frac{\mathbf{rr}}{r^3})\cdot\mathbf{F} \tag{A.18}$$

which recovers the universal Stokeslet solution in Eq. (A.8) and the tensor in the parenthesis is the Oseen tensor.

A.5. Reciprocal Theorem

As the velocity disturbance caused by a point force is given by Eq. B.14 in spherical coordinates, the next step is to calculate the hydrodynamic force experienced by a passive particle in such velocity field. An elegant result that greatly simplifies certain force calculation is in creeping flow is the reciprocal theorem. Let v' be a velocity field that satisfies continuity and Stokes' equation throughout a volume V bounded by a surface S, and let σ' be the corresponding stress tensor. From Stokes' equation we have

$$\boldsymbol{\nabla} \cdot \boldsymbol{\sigma'} = 0, \tag{A.19}$$

where

$$\boldsymbol{\sigma'} = -P'\boldsymbol{\delta} + 2\mu\boldsymbol{\Gamma'} \tag{A.20}$$

for an incompressible, Newtonian fluid and gravitational force is incorporated into pressure. Now let $\mathbf{v}''$ and $\boldsymbol{\sigma''}$ be the velocity and stress for creeping flow of the same fluid in the same geometry, but with different boundary conditions on S. Then, according to the reciprocal theorem, we get

$$\int_S \boldsymbol{n} \cdot \boldsymbol{\sigma'} \cdot \boldsymbol{v''} dS = \int_S \boldsymbol{n} \cdot \boldsymbol{\sigma''} \cdot \boldsymbol{v'} dS. \tag{A.21}$$

A.6. Force on Spheres in Unbounded Flows: Faxén's law

To calculate the force and on a small, solid sphere in a Stokes' flow field created by a moving micro-robot, I first focus on the more general case for spheres in an arbitrary velocity field. This will differ from that given by Stokes' law, which assumes a uniform streaming flow far from the sphere (or a sphere translating in a quiescent fluid). In general, the flow will be three-dimensional, making it difficult to solve the Stokes' equation Eq. B.15 throughout the fluid and integrate the resulting pressure and shear stress over the sphere surface, However, the reciprocal theorem allows the force to be calculated very simply from Stokes' law and the unperturbed velocity far from the sphere.

For convenience, I will call the two flows in the reciprocal theorem as"prime" problem and "double-prime" problem. As Brenner did in [249], the prime problem is chosen to be a sphere of radius R moving at velocity $-\mathbf{U}$ in a fluid that is at rest far from the sphere. Using a particle fixed reference frame, this is the same problem dictated by Stokes' law. Thus, writing Stokes' law in vector form, the drag force on the sphere is

$$\mathbf{F}' = 6\pi\mu R\mathbf{U} \tag{A.22}$$

The direction of the force is opposite to that of the particle motion. In the double-prime problem, it is supposed that a sphere moves at velocity $\mathbf{U_0}$ through a fluid that has an unperturbed velocity $\mathbf{u}(\mathbf{r})$ which is the velocity of the fluid when the sphere is absent. The sphere is assumed not able to rotate. The reference frame is modified by subtracting $\mathbf{u}(\mathbf{r})$ from the sphere and fluid velocities. Thus, the velocity of the sphere center in the double-prime system is $\mathbf{U_0} - \mathbf{u_0}$, where $\mathbf{u_0}$ is the unperturbed velocity evaluated at the sphere center; in the double-prime problem the fluid velocity far from the sphere is zero, that is $\mathbf{u}(r \to \infty) = 0$. It is desired to determine the force $\mathbf{F}''$ that acts on the sphere in this second situation.

An important point is that subtracting the unperturbed velocity does not affect the force in the second problem, even through $\mathbf{u}(\mathbf{r})$ is not a constant. Because $\mathbf{u}(\mathbf{r})$ is a creeping flow solution, the stress calculated from $\mathbf{u}(\mathbf{r})$ must satisfy Eq. B.17 everywhere, including the volume occupied by the sphere. Accordingly, the net force at the surface caused by $\mathbf{u}(\mathbf{r})$ must vanishes since

$$\int_V \boldsymbol{\nabla} \cdot \boldsymbol{\sigma} dV = \mathbf{0} = \int_S \boldsymbol{n} \cdot \boldsymbol{\sigma} dS \tag{A.23}$$

In both problems, the fluid is assumed to be bounded only by the sphere surface (S_0) and by an outer surface (S_∞), which is arbitrarily far away. In other words, S consists of S_0 and S_∞. Having selected both problems so that $v = 0$ on S_∞, the right-hand side of Eq. B.19 can be rewritten as

$$\begin{aligned} \int_S \boldsymbol{n} \cdot \boldsymbol{\sigma''} \cdot \boldsymbol{v'} dS &= \int_{S_0} \boldsymbol{n} \cdot \boldsymbol{\sigma''} \cdot \boldsymbol{v'} dS + \int_{S_\infty} \boldsymbol{n} \cdot \boldsymbol{\sigma''} \cdot \boldsymbol{v'} dS \\ &= \int_{S_0} \boldsymbol{n} \cdot \boldsymbol{\sigma''} \cdot \boldsymbol{v'} dS = -\mathbf{U} \int_{S_0} \boldsymbol{n} \cdot \boldsymbol{\sigma''} dS = -\mathbf{U} \cdot \mathbf{F}'' \end{aligned} \tag{A.24}$$

The evaluation of the left-hand side of Eq. B.19 is facilitated by the fact that the stress vector in Stokes's problem, $\boldsymbol{n} \cdot \boldsymbol{\sigma'}$, is independent of position on the sphere surface, Thus,

$$\boldsymbol{n} \cdot \boldsymbol{\sigma'} = \frac{\mathbf{F}'}{4\pi R^2} = (\frac{3\mu}{2R}\mathbf{U}) \tag{A.25}$$

and the left-hand side of Eq. B.19 becomes

$$\int_{S_0} \boldsymbol{n} \cdot \boldsymbol{\sigma'} \cdot \boldsymbol{v''} dS = (\frac{3\mu}{2R})\mathbf{U} \cdot \int_{S_0} [\mathbf{U_0} - \mathbf{u}(\mathbf{r})] dS. \tag{A.26}$$

Combining this with Eq. A.24 gives

$$\boldsymbol{U} \cdot \boldsymbol{F''} = (\frac{3\mu}{2R})\, \boldsymbol{U} \cdot \int_{S_0} [\mathbf{u}(\mathbf{r}) - \mathbf{U_0}] dS \tag{A.27}$$

or

$$\mathbf{F}'' = (\frac{3\mu}{2R}) \int_{S_0} [\mathbf{u}(\mathbf{r}) - \mathbf{U_0}] dS. \tag{A.28}$$

Because $\mathbf{U_0}$ does not depend on surface position, Eq. A.28 can be reduced to

$$\mathbf{F}'' = (\frac{3\mu}{2R})[\int_{S_0} \mathbf{u}(\mathbf{r})dS - 4\pi R^2\mathbf{U_0}. \tag{A.29}$$

All that is needed now to calculate the force is to integrate the unperturbed velocity over the sphere surface. In particular, Eq. A.29 indicates that it is not necessary to solve a boundary-value problem for the second physical situation as dictated by double-prime problem.

To evaluate the integral in Eq. A.29, the unperturbed velocity is expanded in a Taylor series about the sphere center ($\mathbf{r} = \mathbf{0}$),

$$\mathbf{u}(\mathbf{r}) = \mathbf{u_0} + \mathbf{r}\cdot(\boldsymbol{\nabla u}) + \frac{1}{2}\boldsymbol{rr} : (\boldsymbol{\nabla\nabla u})_{\mathbf{0}} + ... \tag{A.30}$$

where the subscript 0 denote evaluation at $\mathbf{r} = \mathbf{0}$. I will focus on the first three terms and higher order terms in Eq. A.30 are neglected for now. From the integral identity of position vector, we know that

$$\int_{S_0} rdS = 0, \int_{S_0} rrdS = \frac{4\pi R^4}{3}\boldsymbol{\delta}. \tag{A.31}$$

Accordingly, the expansion for the surface integral becomes

$$\int_{S_0} \mathbf{u}(\mathbf{r}) = 4\pi R^2[\mathbf{u_0} + \frac{R^2}{6}(\boldsymbol{\nabla}^2\mathbf{u})_0]. \tag{A.32}$$

Substituting Eq. A.32 into Eq. A.29 give the final expression for the force as

$$\mathbf{F} = 6\pi\mu R[\mathbf{u_0} - \mathbf{U_0} + \frac{R^2}{6}(\boldsymbol{\nabla}^2\mathbf{u})_0] \tag{A.33}$$

which is known as the Faxén's first law. For a uniform unperturbed velocity, where $\boldsymbol{\nabla}^2\mathbf{u} = \mathbf{0}$, Stokes' law is recovered. That is, the drag is proportional to the velocity difference between the unperturbed fluid and the sphere. In general, however, there is an additional contribution to the force that is proportional to $\boldsymbol{\nabla}^2\mathbf{u}$.

With all the relations derived above, let's revisit our system. A micro-robot and a passive particle are both trapped at the interface at location $\mathbf{x_1}$ and $\mathbf{x_2}$ respectively. The micro-robot is moving along the centerline of the two at a steady velocity $\mathbf{U}$. We assume no net force on passive particle and a hydrodynamic force $\mathbf{F_d}$ on the micro-robot, with $\mathbf{F_d}||\mathbf{d_12}$. The velocity field created by the micro-robot is expressed as a stokeslet and a degenerate quadrupole at $\mathbf{x_1}$ as

$$\mathbf{v}(\mathbf{x}') = -\mathbf{F_d} \cdot (1 + \frac{a^2}{6}\boldsymbol{\nabla}^2)\frac{\mathbf{g}(\mathbf{x}')}{8\pi\mu} \tag{A.34}$$

where $\mathbf{g}(\mathbf{x}')$ is the Oseen tensor and $\mathbf{x}' = \mathbf{x} - \mathbf{x_1}$.

From Faxén's law we know that for passive particle with radius b at $\mathbf{x_2}$, the force on the sphere by the fluid is given by Eq. A.33 as

$$\mathbf{F} = 6\pi\mu b[1 + \frac{b^2}{6}\boldsymbol{\nabla}^2]\mathbf{v}(\mathbf{x}')|_{\mathbf{x}=\mathbf{x_2}} - 6\pi\mu b\mathbf{U_p} \tag{A.35}$$

where $\mathbf{U_p}$ is the velocity for the passive particle. Since it is force free, $\mathbf{F} = \mathbf{0}$, we can calculate $\mathbf{U_p}$ by substitution of $\mathbf{v}(\mathbf{x}')|_{\mathbf{x}=\mathbf{x_2}}$ using Eq. A.34 and get the expression for $\mathbf{U_p}$ as

$$\mathbf{U_p} = \frac{3a\mathbf{U}}{4}[\frac{2}{r} - \frac{2b^2}{3r^3} - \frac{2a^2}{3r^3}] \tag{A.36}$$

For far field when $r \gg b$, we have

$$\mathbf{U_p} \approx \frac{3a\mathbf{U}}{4}[\frac{2}{r} - \frac{2a^2}{3r^3}] = \mathbf{U}(\frac{3}{2}R^{-1} - \frac{1}{2}R^{-3}) \tag{A.37}$$

where $R = \frac{r}{a}$.

For smaller passive particles, I assumed that they are moving with the velocity field as tracer particles and, Therefore, according to Eq. A.37, the hydrodynamic force experienced by the passive particles is proportional to $(AR^{-1} + BR^{-3})$, where A and B are constants accounts for the geometry for the micro-robot (for example, we have $A = 3/2$,$B = -1/2$ for spherical micro-robot), while the capillary attraction force is proportional to (R^{-5}) for small particles at curved interface with quadrupolar deformation[121] as

$$F_{cap} = 24\pi\gamma h_{qp1} h_{qp2} a^2 b^2 / r^5. \tag{A.38}$$

where γ is surface tension and h_{qp1}, h_{qp2} are magnitude of quadrupolar deformation of the micro-robot and the passive particle, respectively. Adding this force to eq. A.35, we get the expression for relative velocity between the micro-robot and passive micro-particle as shown in chapter 2 as

$$\mathbf{U} - \mathbf{U_p} = \mathbf{U} - \mathbf{U}\left[\frac{3}{2}\left(\frac{a}{r}\right) - \frac{1}{2}\left(\frac{a}{r}\right)^3\right] + \frac{\mathbf{F}_{cap}}{6\pi\mu b}. \tag{A.39}$$

Qualitatively, capillary attraction decays faster than hydrodynamic interaction which pushes the particles away. Therefore, capillary attraction dominates in the near field while hydrodynamic interaction plays a more important role when the pair is several radii away from each other. At large separations, both capillary and hydrodynamic interaction are negligible and drift dominates. Such hypothesis is in agreement with the experimental observations by Archit et al. [151] and in my system. As shown in Fig. 2.5e, as the micro-robot is moving toward the passive particle, it first enters the domian that hydrodynamic interaction dominates. The corresponding relative velocity is decreasing since hydrodynamics is trying to push the particle away from the micro-robot. When the particle is getting closer to the micro-robot, it reaches a point where hydrodynamics interaction is balanced by the capillary attraction. Then, as capillary is taking over in the near field, the relative velocity ramps up until close contact.

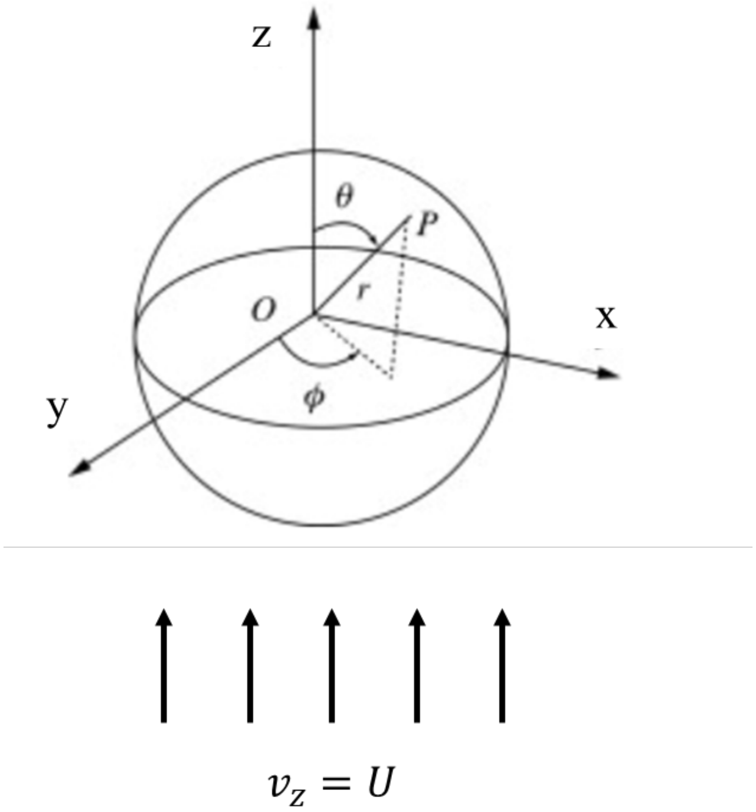

Figure A.1: Flow past a stationary, solid sphere with uniform velocity U along the z-axis far from the sphere.

APPENDIX B. Drag coefficient for a tilted plate translating between two solid boundaries

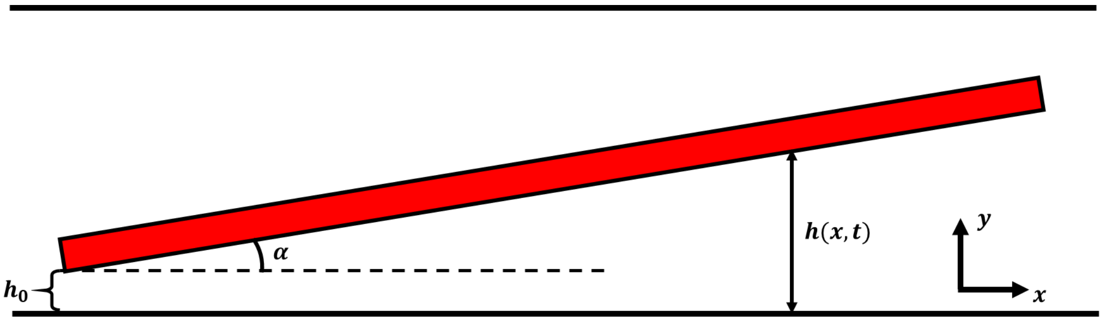

Figure B.1: Schematics for a tilted plate translating between two parallel boundaries

In this appendix, we consider a problem where a tilted plate with length L and width W translating between two solid boundaries (as shown in Fig. B.1) in lubrication limit for scaling analysis of our nametic swimmer described in chapter 3. We assume small gap thickness $\varepsilon = \frac{h_0}{L} \ll 1$ between the plate and boundaries and small slope ($\alpha \sim sin\alpha = \frac{h_0}{L} = \varepsilon$) for the tilting. The speeds of the plate along the x and y direction are V_{xc} and V_{yc}, respectively. The Reynolds number in our experiment is much smaller than 1 and therefore the fluid is in equilibrium with the instantaneous position of the boundaries. The goal is derive a scaling argument for the drag coefficient with which we can calculate the translation speed of the swimmer due to multiple mechanisms proposed in Chapter 3.

We begin our analysis with the Navier-Stokes and continuity equations for an incompressible fluid, in there most general dimensional form,

$$\nabla' \cdot \mathbf{u}' = 0, \tag{B.1}$$

$$\rho(\frac{\partial \mathbf{u}'}{\partial t'} + \mathbf{u}' \cdot \nabla' \mathbf{u}') = -\nabla' p' + \mu \nabla'^2 \mathbf{u}'. \tag{B.2}$$

Let $\nabla' = \frac{1}{L}\nabla$, $u_x = \frac{u_x{}'}{V_{xc}}$, $u_y = \frac{u_y{}'}{\varepsilon V_{xc}}$, $p = \frac{p'}{p_c}$ and $t = \frac{t'}{t_c}$, where$t_c = \frac{L}{V_{xc}}$ and $p_c \sim \frac{\mu V_{xc}}{\varepsilon^2 L}$. In dimensionless form, eq. B.1 can be written as

$$\frac{\partial u_x}{\partial x} + \frac{\partial u_y}{\partial y} = 0. \tag{B.3}$$

and eq. B.2 can be written as

$$\frac{\rho {V_{xc}}^2}{L}(\frac{\partial u_x}{\partial t} + u_x\frac{\partial u_x}{\partial x} + u_y\frac{\partial u_x}{\partial y}) = -\frac{p_c}{L}\frac{\partial p}{\partial x} + \frac{p_c}{L}[\varepsilon^2\frac{\partial^2 u_x}{\partial x^2} + \frac{\partial^2 u_x}{\partial y^2}], \tag{B.4}$$

$$\frac{\rho\varepsilon {V_{xc}}^2}{L}(\frac{\partial u_y}{\partial t} + u_x\frac{\partial u_y}{\partial x} + u_y\frac{\partial u_y}{\partial y}) = -\frac{p_c}{\varepsilon L}\frac{\partial p}{\partial y} + \frac{p_c}{L}[\varepsilon\frac{\partial^2 u_y}{\partial x^2} + \frac{\partial^2 u_y}{\partial y^2}]. \tag{B.5}$$

Since $Re = \frac{\rho V_{xc} L}{\mu}$, eqns. B.4 and B.5 can be rewritten as

$$\frac{\partial^2 u_x}{\partial y^2} - \frac{\partial p}{\partial x} = -\varepsilon^2\frac{\partial^2 u_x}{\partial x^2} + \varepsilon^2 Re(u_x\frac{\partial u_x}{\partial x} + u_y\frac{\partial u_x}{\partial y}), \tag{B.6}$$

$$\frac{\partial p}{\partial y} = -\varepsilon^2\{[\frac{\partial^2 u_y}{\partial y^2} + \varepsilon^2\frac{\partial^2 u_y}{\partial x^2}] + \varepsilon^2 Re(u_x\frac{\partial u_y}{\partial x} + u_y\frac{\partial u_y}{\partial y})\}. \tag{B.7}$$

Since $\varepsilon \ll 1$ and $\varepsilon^2 Re \ll 1$, eqns. B.6 and B.7 can be simplified into

$$\frac{\partial^2 u_x}{\partial y^2} = \frac{\partial p}{\partial x}, \tag{B.8}$$

$$\frac{\partial p}{\partial y} = 0. \tag{B.9}$$

Integrate eq. B.8 along x, we get

$$u_x = \frac{1}{2}\frac{dp}{dx}y^2 + C_1 y + C_2. \tag{B.10}$$

Plug in boundary conditions $u_x(y=0)=0$ and $u_x(y=h)=V_x$, we get

$$u_x = \frac{1}{2}\frac{dp}{dx}(y^2 - hy) + \frac{V_x y}{h}. \tag{B.11}$$

Integrate the eq. B.3 along y direction and plug in the expression for u_x, we can get

$$\frac{\partial h}{\partial t} = \frac{\partial}{\partial x}[\frac{h^3}{12}\frac{\partial p}{\partial x}] - \frac{h}{2}\frac{\partial V_c}{\partial x} + \frac{1}{2}V_x\frac{\partial h}{\partial x}, \tag{B.12}$$

which is a general form of Reynolds equation. With the boundary motion specified and the shape of the thin film specified, it can be used as a DE for the unknown pressure distribution in the thin film. If the dimensionless gap width is only a function of position, $h(x)$. Then, eq. B.12 can be integrated for the pressure along the x direction and get

$$p = -6m\int_0^x \frac{sds}{h^3 s} + c_1\int_0^x \frac{ds}{h^3(s)} + c_2. \tag{B.13}$$

where $m = \frac{dh}{dx}$. The integration constants c_1 and c_2 are given by the boundary values for p at $x=0$ and $x=1$; these come from the dynamic pressure values for a stationary fluid in the region outside the lubrication layer. We assume that the slider block is moving through a large body of fluid that completely surrounds it. In this case, it is obvious that $p(0) = p(1) = p_0$, where p_0 is an arbitrary reference pressure which is a consequence of the assumed incompressibility of the fluid. Plug in c_1 and c_2 from boundary condition, we get

$$p(x) - p_0 = \frac{6m}{m+2}\frac{x - x^2}{(1+mx)^2}. \tag{B.14}$$

Converting eq.B.14 back to the dimentional terms, the pressure distribution becomes

$$p'(x) - p'_0 = \frac{6\mu U m}{L\varepsilon^2(m+2)}\frac{Lx' - x'^2}{(L+mx')^2}. \tag{B.15}$$

Now we can calculate the hydrodynamic forces on the plate. In general, for any body in a viscous fluid,

$$F' = \int_A \mathbf{t}' dA = \int_A \mathbf{n} \cdot \mathbf{T}' dA = -\int_A p'\mathbf{n} dA + \int_A \mathbf{n} \cdot \tau' dA, \tag{B.16}$$

where A represent the surface area of the plate. In eq. **??**, $p'(0)$ was used as the background reference pressure. Thus, to a first approximation,

$$\mathbf{F}' = -\int_A -\mathbf{n}[p' - p'(0)] dA + \int_A \mathbf{n} \cdot \tau' dA. \tag{B.17}$$

Finally, we can calculate the x component of $\mathbf{F}$ on the bottom surface of the plate is

$$F_x' = W(\int_0^L -[p'(x) - p'(0)] m dx' + \int_0^L [m\tau_{xx}' - \tau_{xy}'] dx'). \tag{B.18}$$

Substituting for $[p'(x) - p'(0)]$ and $[m\tau_{xx}' - \tau_{xy}']$ by using eq. B.14 and the corresponding expression for τ_{xx}' and τ_{xy}' from the velocity field calculated using the pressure gradient, we find that

$$\begin{aligned} F_x' &= \mu V_x W[\frac{6}{\varepsilon(2+m)} - \frac{2}{\varepsilon m} ln(1+m)] \\ &= \frac{\mu V_x L W}{h_0}[\frac{6}{2+m} - \frac{2}{m} ln(1+m)] \\ &= \{\frac{\mu L W}{h_0}[\frac{6}{2+m} - \frac{2}{m} ln(1+m)]\} V_x \end{aligned} \tag{B.19}$$

Equating eq. B.19 to the drag force, we get

$$F_x' = \{\frac{\mu L W}{h_0}[\frac{6}{2+m} - \frac{2}{m} ln(1+m)]\} V_x = F_{drag} = C_D \mu a V_x. \tag{B.20}$$

Therefore, the drag coefficient for a tilted plate translating near a solid boundary with lubrication limit scale as

$$C_D \sim \frac{LW}{ah_0}. \tag{B.21}$$

For our system where we have a circular disk with radius $2a$, we have $L \sim 2a$ and $W \sim 2a$, thus $C_D \ \sim \frac{4a}{h_0}$. For a disk translating in a confined environment between two parallel plates, the drag coefficient is estimated from as $c_d \sim c_{d,bottom} + c_{d,top} \sim \frac{4a}{h_0} + \frac{4a}{h_1}$, where h_0 and h_1 are the gap thickness between the disk surface and the bottom plate and the top plate, respectively. For a typical cell we used in the experiment, FCPM reveals that $h_0 \sim \frac{1}{2}h_1 \sim 8.6\,\mu\text{m}$. By using the dimensionless parameter $\varepsilon = \frac{h_0}{2a}$, a drag coefficient $c_d = \frac{3}{\varepsilon}$ is used in Chapter 3 for calculating translation speed due to multiple mechanism.

BIBLIOGRAPHY

[1] Dhont, J. K. *An introduction to dynamics of colloids* (Elsevier, 1996).

[2] Kim, S. & Karrila, S. J. *Microhydrodynamics: principles and selected applications* (Courier Corporation, 2013).

[3] Aranson, I. S. & Tsimring, L. S. Patterns and collective behavior in granular media: Theoretical concepts. *Reviews of modern physics* **78**, 641 (2006).

[4] Palacci, J., Sacanna, S., Steinberg, A. P., Pine, D. J. & Chaikin, P. M. Living crystals of light-activated colloidal surfers. *Science* **339**, 936–940 (2013).

[5] Bialké, J., Speck, T. & Löwen, H. Active colloidal suspensions: Clustering and phase behavior. *Journal of Non-Crystalline Solids* **407**, 367–375 (2015).

[6] Driscoll, M. *et al.* Unstable fronts and motile structures formed by microrollers. *Nature Physics* **13**, 375–379 (2017).

[7] Cappelleri, D., Efthymiou, D., Goswami, A., Vitoroulis, N. & Zavlanos, M. Towards mobile microrobot swarms for additive micromanufacturing. *International Journal of Advanced Robotic Systems* **11**, 150 (2014).

[8] Tasoglu, S., Diller, E., Guven, S., Sitti, M. & Demirci, U. Untethered micro-robotic coding of three-dimensional material composition. *Nature communications* **5**, 1–9 (2014).

[9] Diller, E. & Sitti, M. Three-dimensional programmable assembly by untethered magnetic robotic micro-grippers. *Advanced Functional Materials* **24**, 4397–4404 (2014).

[10] Vikram Singh, A. & Sitti, M. Targeted drug delivery and imaging using mobile milli/microrobots: A promising future towards theranostic pharmaceutical design. *Current pharmaceutical design* **22**, 1418–1428 (2016).

[11] Jang, D., Jeong, J., Song, H. & Chung, S. K. Targeted drug delivery technology using untethered microrobots: A review. *Journal of Micromechanics and Microengineering* **29**, 053002 (2019).

[12] Hwang, G. *et al.* Catalytic antimicrobial robots for biofilm eradication. *Science robotics* **4** (2019).

[13] Jager, E. W., Inganäs, O. & Lundström, I. Microrobots for micrometer-size objects in aqueous media: potential tools for single-cell manipulation. *Science* **288**, 2335–2338 (2000).

[14] Li, J. *et al.* Development of a magnetic microrobot for carrying and delivering targeted cells. *Science Robotics* **3** (2018).

[15] Jin, Q., Yang, Y., Jackson, J. A., Yoon, C. & Gracias, D. H. Untethered single cell grippers for active biopsy. *Nano Letters* **20**, 5383–5390 (2020).

[16] Yan, X. *et al.* Multifunctional biohybrid magnetite microrobots for imaging-guided therapy. *Science Robotics* **2** (2017).

[17] Zhang, Y. *et al.* Real-time tracking of fluorescent magnetic spore–based microrobots for remote detection of c. diff toxins. *Science advances* **5**, eaau9650 (2019).

[18] Miriyev, A. & Kovač, M. Skills for physical artificial intelligence. *Nature Machine Intelligence* **2**, 658–660 (2020).

[19] Sitti, M. Physical intelligence as a new paradigm. *Extreme Mechanics Letters* **46**, 101340 (2021).

[20] Hines, L., Petersen, K., Lum, G. Z. & Sitti, M. Soft actuators for small-scale robotics. *Advanced materials* **29**, 1603483 (2017).

[21] Alapan, Y., Yigit, B., Beker, O., Demirörs, A. F. & Sitti, M. Shape-encoded dynamic assembly of mobile micromachines. *Nature materials* **18**, 1244–1251 (2019).

[22] Bernasconi, R., Pané, S. & Magagnin, L. Soft microrobotics. In *Soft Robotics*, vol. 57, 1–44 (Elsevier, 2021).

[23] Manoharan, V. N. Colloidal matter: Packing, geometry, and entropy. *Science* **349**, 1253751 (2015).

[24] Cademartiri, L. & Bishop, K. J. Programmable self-assembly. *Nature materials* **14**, 2–9 (2015).

[25] Li, W. *et al.* Colloidal molecules and patchy particles: Complementary concepts, synthesis and self-assembly. *Chemical Society Reviews* **49**, 1955–1976 (2020).

[26] Marchetti, M. C. *et al.* Hydrodynamics of soft active matter. *Reviews of Modern Physics* **85**, 1143 (2013).

[27] Elgeti, J., Winkler, R. G. & Gompper, G. Physics of microswimmers—single particle motion and collective behavior: a review. *Reports on progress in physics* **78**, 056601 (2015).

[28] Bechinger, C. *et al.* Active particles in complex and crowded environments. *Reviews of Modern Physics* **88**, 045006 (2016).

[29] Zöttl, A. & Stark, H. Emergent behavior in active colloids. *Journal of Physics: Condensed Matter* **28**, 253001 (2016).

[30] Gompper, G. *et al.* The 2020 motile active matter roadmap. *Journal of Physics: Condensed Matter* **32**, 193001 (2020).

[31] Ramaswamy, S. The mechanics and statistics of active matter. *Annu. Rev. Condens. Matter Phys.* **1**, 323–345 (2010).

[32] Aranson, I. S. Active colloids. *Physics-Uspekhi* **56**, 79 (2013).

[33] Moran, J. L. & Posner, J. D. Phoretic self-propulsion. *Annual Review of Fluid Mechanics* **49**, 511–540 (2017).

[34] Tsang, A. C., Demir, E., Ding, Y. & Pak, O. S. Roads to smart artificial microswimmers. *Advanced Intelligent Systems* **2**, 1900137 (2020).

[35] Carlsen, R. W. & Sitti, M. Bio-hybrid cell-based actuators for microsystems. *Small* **10**, 3831–3851 (2014).

[36] Lauga, E. & Powers, T. R. The hydrodynamics of swimming microorganisms. *Reports on Progress in Physics* **72**, 096601 (2009).

[37] Han, K., Shields IV, C. W. & Velev, O. D. Engineering of self-propelling microbots and microdevices powered by magnetic and electric fields. *Advanced Functional Materials* **28**, 1705953 (2018).

[38] Kummer, M. P. *et al.* Octomag: An electromagnetic system for 5-dof wireless micromanipulation. *IEEE Transactions on Robotics* **26**, 1006–1017 (2010).

[39] Steager, E. B. *et al.* Automated biomanipulation of single cells using magnetic microrobots. *The International Journal of Robotics Research* **32**, 346–359 (2013).

[40] Yao, T., Chisholm, N. G., Steager, E. B. & Stebe, K. J. Directed assembly and micromanipulation of passive particles at fluid interfaces via capillarity using a magnetic micro-robot. *Applied Physics Letters* **116**, 043702 (2020).

[41] Snezhko, A., Belkin, M., Aranson, I. & Kwok, W.-K. Self-assembled magnetic surface swimmers. *Physical review letters* **102**, 118103 (2009).

[42] Xie, H. *et al.* Reconfigurable magnetic microrobot swarm: Multimode transformation, locomotion, and manipulation. *Science robotics* **4** (2019).

[43] Purcell, E. M. Life at low reynolds number. *American journal of physics* **45**, 3–11 (1977).

[44] Dreyfus, R. *et al.* Microscopic artificial swimmers. *Nature* **437**, 862–865 (2005).

[45] Ghosh, A. & Fischer, P. Controlled propulsion of artificial magnetic nanostructured propellers. *Nano letters* **9**, 2243–2245 (2009).

[46] Zhang, L. *et al.* Artificial bacterial flagella: Fabrication and magnetic control. *Applied Physics Letters* **94**, 064107 (2009).

[47] Zhang, L. *et al.* Characterizing the swimming properties of artificial bacterial flagella. *Nano letters* **9**, 3663–3667 (2009).

[48] Gao, W., Sattayasamitsathit, S., Manesh, K. M., Weihs, D. & Wang, J. Magnetically powered flexible metal nanowire motors. *Journal of the American Chemical Society* **132**, 14403–14405 (2010).

[49] Pak, O. S., Gao, W., Wang, J. & Lauga, E. High-speed propulsion of flexible nanowire motors: Theory and experiments. *Soft Matter* **7**, 8169–8181 (2011).

[50] Martinez-Pedrero, F., Ortiz-Ambriz, A., Pagonabarraga, I. & Tierno, P. Colloidal microworms propelling via a cooperative hydrodynamic conveyor belt. *Physical review letters* **115**, 138301 (2015).

[51] Martinez-Pedrero, F., Navarro-Argemí, E., Ortiz-Ambriz, A., Pagonabarraga, I. & Tierno, P. Emergent hydrodynamic bound states between magnetically powered micropropellers. *Science advances* **4**, eaap9379 (2018).

[52] Fang, W.-Z., Ham, S., Qiao, R. & Tao, W.-Q. Magnetic actuation of surface walkers: The effects of confinement and inertia. *Langmuir* **36**, 7046–7055 (2020).

[53] Zhang, L. *et al.* Controlled propulsion and cargo transport of rotating nickel nanowires near a patterned solid surface. *ACS nano* **4**, 6228–6234 (2010).

[54] Mair, L. *et al.* Magnetic microkayaks: propulsion of microrods precessing near a surface by kilohertz frequency, rotating magnetic fields. *Nanoscale* **9**, 3375–3381 (2017).

[55] Tierno, P., Golestanian, R., Pagonabarraga, I. & Sagués, F. Controlled swimming in confined fluids of magnetically actuated colloidal rotors. *Physical review letters* **101**, 218304 (2008).

[56] O'Brien, R. W. & White, L. R. Electrophoretic mobility of a spherical colloidal particle. *Journal of the Chemical Society, Faraday Transactions 2: Molecular and Chemical Physics* **74**, 1607–1626 (1978).

[57] Ramos, A., Morgan, H., Green, N. G. & Castellanos, A. Ac electrokinetics: a review of forces in microelectrode structures. *Journal of Physics D: Applied Physics* **31**, 2338 (1998).

[58] Gangwal, S., Cayre, O. J., Bazant, M. Z. & Velev, O. D. Induced-charge electrophoresis of metallodielectric particles. *Physical review letters* **100**, 058302 (2008).

[59] Lavrentovich, O. D., Lazo, I. & Pishnyak, O. P. Nonlinear electrophoresis of dielectric and metal spheres in a nematic liquid crystal. *Nature* **467**, 947–950 (2010).

[60] Lazo, I. & Lavrentovich, O. D. Liquid-crystal-enabled electrophoresis of spheres in a nematic medium with negative dielectric anisotropy. *Philosophical Transactions of*

the Royal Society A: Mathematical, Physical and Engineering Sciences **371**, 20120255 (2013).

[61] Jiang, H.-R., Wada, H., Yoshinaga, N. & Sano, M. Manipulation of colloids by a nonequilibrium depletion force in a temperature gradient. *Physical review letters* **102**, 208301 (2009).

[62] Jiang, H.-R., Yoshinaga, N. & Sano, M. Active motion of a janus particle by self-thermophoresis in a defocused laser beam. *Physical review letters* **105**, 268302 (2010).

[63] Volpe, G., Kurz, L., Callegari, A., Volpe, G. & Gigan, S. Speckle optical tweezers: micromanipulation with random light fields. *Optics express* **22**, 18159–18167 (2014).

[64] Jones, P. H., Maragò, O. M. & Volpe, G. *Optical tweezers: Principles and applications* (Cambridge University Press, 2015).

[65] Volpe, G., Buttinoni, I., Vogt, D., Kümmerer, H.-J. & Bechinger, C. Microswimmers in patterned environments. *Soft Matter* **7**, 8810–8815 (2011).

[66] Buttinoni, I., Volpe, G., Kümmel, F., Volpe, G. & Bechinger, C. Active brownian motion tunable by light. *Journal of Physics: Condensed Matter* **24**, 284129 (2012).

[67] Samin, S. & Van Roij, R. Self-propulsion mechanism of active janus particles in near-critical binary mixtures. *Physical review letters* **115**, 188305 (2015).

[68] Würger, A. Self-diffusiophoresis of janus particles in near-critical mixtures. *Physical review letters* **115**, 188304 (2015).

[69] Yuan, Y., Abuhaimed, G. N., Liu, Q. & Smalyukh, I. I. Self-assembled nematic colloidal motors powered by light. *Nature communications* **9**, 1–12 (2018).

[70] Wang, W., Castro, L. A., Hoyos, M. & Mallouk, T. E. Autonomous motion of metallic microrods propelled by ultrasound. *ACS nano* **6**, 6122–6132 (2012).

[71] Paxton, W. F. *et al.* Catalytic nanomotors: autonomous movement of striped nanorods. *Journal of the American Chemical Society* **126**, 13424–13431 (2004).

[72] Fournier-Bidoz, S., Arsenault, A. C., Manners, I. & Ozin, G. A. Synthetic self-propelled nanorotors. *Chemical Communications* 441–443 (2005).

[73] Mano, N. & Heller, A. Bioelectrochemical propulsion. *Journal of the American Chemical Society* **127**, 11574–11575 (2005).

[74] Solovev, A. A., Mei, Y., Bermúdez Ureña, E., Huang, G. & Schmidt, O. G. Catalytic microtubular jet engines self-propelled by accumulated gas bubbles. *Small* **5**, 1688–1692 (2009).

[75] Solovev, A. A., Sanchez, S., Pumera, M., Mei, Y. F. & Schmidt, O. G. Magnetic control of tubular catalytic microbots for the transport, assembly, and delivery of micro-objects. *Advanced Functional Materials* **20**, 2430–2435 (2010).

[76] Howse, J. R. *et al.* Self-motile colloidal particles: from directed propulsion to random walk. *Physical review letters* **99**, 048102 (2007).

[77] Maass, C. C., Krüger, C., Herminghaus, S. & Bahr, C. Swimming droplets. *Annual Review of Condensed Matter Physics* **7**, 171–193 (2016).

[78] Thutupalli, S., Seemann, R. & Herminghaus, S. Swarming behavior of simple model squirmers. *New Journal of Physics* **13**, 073021 (2011).

[79] Schmitt, M. & Stark, H. Swimming active droplet: A theoretical analysis. *EPL (Europhysics Letters)* **101**, 44008 (2013).

[80] Izri, Z., Van Der Linden, M. N., Michelin, S. & Dauchot, O. Self-propulsion of pure water droplets by spontaneous marangoni-stress-driven motion. *Physical review letters* **113**, 248302 (2014).

[81] Dietrich, K., Jaensson, N., Buttinoni, I., Volpe, G. & Isa, L. Microscale marangoni surfers. *Physical Review Letters* **125**, 098001 (2020).

[82] Behkam, B. & Sitti, M. Bacterial flagella-based propulsion and on/off motion control of microscale objects. *Applied Physics Letters* **90**, 023902 (2007).

[83] Steager, E. *et al.* Control of microfabricated structures powered by flagellated bacteria using phototaxis. *Applied Physics Letters* **90**, 263901 (2007).

[84] Di Leonardo, R. *et al.* Bacterial ratchet motors. *Proceedings of the National Academy of Sciences* **107**, 9541–9545 (2010).

[85] Magdanz, V., Sanchez, S. & Schmidt, O. G. Development of a sperm-flagella driven micro-bio-robot. *Advanced Materials* **25**, 6581–6588 (2013).

[86] Park, B.-W., Zhuang, J., Yasa, O. & Sitti, M. Multifunctional bacteria-driven microswimmers for targeted active drug delivery. *ACS nano* **11**, 8910–8923 (2017).

[87] Alapan, Y. *et al.* Soft erythrocyte-based bacterial microswimmers for cargo delivery. *Science Robotics* **3** (2018).

[88] Vaccari, L., Molaei, M., Leheny, R. L. & Stebe, K. J. Cargo carrying bacteria at interfaces. *Soft Matter* **14**, 5643–5653 (2018).

[89] Rajabi, M., Baza, H., Turiv, T. & Lavrentovich, O. D. Directional self-locomotion of active droplets enabled by nematic environment. *Nature Physics* **17**, 260–266 (2021).

[90] Chen, X.-Z. *et al.* Small-scale machines driven by external power sources. *Advanced Materials* **30**, 1705061 (2018).

[91] Baraban, L. *et al.* Catalytic janus motors on microfluidic chip: deterministic motion for targeted cargo delivery. *ACS nano* **6**, 3383–3389 (2012).

[92] Ren, L. *et al.* 3d steerable, acoustically powered microswimmers for single-particle manipulation. *Science advances* **5**, eaax3084 (2019).

[93] McNeill, J. M., Nama, N., Braxton, J. M. & Mallouk, T. E. Wafer-scale fabrication of micro-to nanoscale bubble swimmers and their fast autonomous propulsion by ultrasound. *ACS nano* **14**, 7520–7528 (2020).

[94] Maggi, C., Saglimbeni, F., Dipalo, M., De Angelis, F. & Di Leonardo, R. Micromotors with asymmetric shape that efficiently convert light into work by thermocapillary effects. *Nature communications* **6**, 1–5 (2015).

[95] Dai, B. *et al.* Programmable artificial phototactic microswimmer. *Nature nanotechnology* **11**, 1087–1092 (2016).

[96] Zheng, J. *et al.* Orthogonal navigation of multiple visible-light-driven artificial microswimmers. *Nature communications* **8**, 1–7 (2017).

[97] Zhang, L., Peyer, K. E. & Nelson, B. J. Artificial bacterial flagella for micromanipulation. *Lab on a Chip* **10**, 2203–2215 (2010).

[98] Martínez-Pedrero, F. & Tierno, P. Advances in colloidal manipulation and transport via hydrodynamic interactions. *Journal of colloid and interface science* **519**, 296–311 (2018).

[99] Ebbens, S., Jones, R. A., Ryan, A. J., Golestanian, R. & Howse, J. R. Self-assembled autonomous runners and tumblers. *Physical Review E* **82**, 015304 (2010).

[100] Gao, W., Pei, A., Feng, X., Hennessy, C. & Wang, J. Organized self-assembly of janus micromotors with hydrophobic hemispheres. *Journal of the American Chemical Society* **135**, 998–1001 (2013).

[101] Wang, W., Giltinan, J., Zakharchenko, S. & Sitti, M. Dynamic and programmable self-assembly of micro-rafts at the air-water interface. *Science advances* **3**, e1602522 (2017).

[102] Yigit, B., Alapan, Y. & Sitti, M. Programmable collective behavior in dynamically self-assembled mobile microrobotic swarms. *Advanced Science* **6**, 1801837 (2019).

[103] Zhang, J., Luijten, E., Grzybowski, B. A. & Granick, S. Active colloids with collective mobility status and research opportunities. *Chemical Society Reviews* **46**, 5551–5569 (2017).

[104] Alapan, Y., Bozuyuk, U., Erkoc, P., Karacakol, A. C. & Sitti, M. Multifunctional surface microrollers for targeted cargo delivery in physiological blood flow. *Science Robotics* **5** (2020).

[105] Sakar, M. S. *et al.* Single cell manipulation using ferromagnetic composite microtransporters. *Applied physics letters* **96**, 043705 (2010).

[106] Tottori, S. *et al.* Magnetic helical micromachines: fabrication, controlled swimming, and cargo transport. *Advanced materials* **24**, 811–816 (2012).

[107] Gultepe, E. *et al.* Biopsy with thermally-responsive untethered microtools. *Advanced materials* **25**, 514–519 (2013).

[108] Fusco, S. *et al.* An integrated microrobotic platform for on-demand, targeted therapeutic interventions. *Advanced Materials* **26**, 952–957 (2014).

[109] Han, K. *et al.* Sequence-encoded colloidal origami and microbot assemblies from patchy magnetic cubes. *Science advances* **3**, e1701108 (2017).

[110] Burdick, J., Laocharoensuk, R., Wheat, P. M., Posner, J. D. & Wang, J. Synthetic nanomotors in microchannel networks: Directional microchip motion and controlled manipulation of cargo. *Journal of the American Chemical Society* **130**, 8164–8165 (2008).

[111] Gao, W. *et al.* Cargo-towing fuel-free magnetic nanoswimmers for targeted drug delivery. *small* **8**, 460–467 (2012).

[112] Ye, Z., Diller, E. & Sitti, M. Micro-manipulation using rotational fluid flows induced by remote magnetic micro-manipulators. *Journal of Applied Physics* **112**, 064912 (2012).

[113] Petit, T., Zhang, L., Peyer, K. E., Kratochvil, B. E. & Nelson, B. J. Selective trapping and manipulation of microscale objects using mobile microvortices. *Nano letters* **12**, 156–160 (2012).

[114] Tung, H.-W., Peyer, K. E., Sargent, D. F. & Nelson, B. J. Noncontact manipulation using a transversely magnetized rolling robot. *Applied Physics Letters* **103**, 114101 (2013).

[115] Ye, Z. & Sitti, M. Dynamic trapping and two-dimensional transport of swimming microorganisms using a rotating magnetic microrobot. *Lab on a Chip* **14**, 2177–2182 (2014).

[116] Huang, T.-Y. *et al.* Generating mobile fluidic traps for selective three-dimensional transport of microobjects. *Applied Physics Letters* **105**, 114102 (2014).

[117] Huang, T.-Y. *et al.* 3d printed microtransporters: Compound micromachines for spatiotemporally controlled delivery of therapeutic agents. *Advanced Materials* **27**, 6644–6650 (2015).

[118] Mishler, G., Tsang, A. C. H. & Pak, O. S. Hydrodynamic capture and release of passively driven particles by active particles under hele-shaw flows. *Journal of Nonlinear Science* **28**, 1379–1396 (2018).

[119] Lin, Z. *et al.* Magnetically actuated peanut colloid motors for cell manipulation and patterning. *ACS nano* **12**, 2539–2545 (2018).

[120] Lee, S. *et al.* A capsule-type microrobot with pick-and-drop motion for targeted drug and cell delivery. *Advanced healthcare materials* **7**, 1700985 (2018).

[121] Liu, I. B., Sharifi-Mood, N. & Stebe, K. J. Capillary assembly of colloids: Interactions on planar and curved interfaces. *Annual Review of Condensed Matter Physics* **9**, 283–305 (2018).

[122] Ni, S., Isa, L. & Wolf, H. Capillary assembly as a tool for the heterogeneous integration of micro-and nanoscale objects. *Soft Matter* **14**, 2978–2995 (2018).

[123] Wong, D., Liu, I. B., Steager, E. B., Stebe, K. J. & Kumar, V. Directed micro assembly of passive particles at fluid interfaces using magnetic robots. In *2016 International Conference on Manipulation, Automation and Robotics at Small Scales (MARSS)*, 1–6 (IEEE, 2016).

[124] He, Y., Wang, L., Zhong, L., Liu, Y. & Rong, W. Transporting microobjects using a magnetic microrobot at water surfaces. In *2018 15th International Conference on Control, Automation, Robotics and Vision (ICARCV)*, 108–112 (IEEE, 2018).

[125] Grosjean, G., Hubert, M. & Vandewalle, N. Magnetocapillary self-assemblies: Locomotion and micromanipulation along a liquid interface. *Advances in colloid and interface science* **255**, 84–93 (2018).

[126] Barbot, A., Tan, H., Power, M., Seichepine, F. & Yang, G.-Z. Floating magnetic microrobots for fiber functionalization. *Science Robotics* **4** (2019).

[127] Piñan Basualdo, F. N., Bolopion, A., Gauthier, M. & Lambert, P. A microrobotic platform actuated by thermocapillary flows for manipulation at the air-water interface. *Science Robotics* **6**, eabd3557 (2021).

[128] Aubry, N., Singh, P., Janjua, M. & Nudurupati, S. Micro-and nanoparticles self-assembly for virtually defect-free, adjustable monolayers. *Proceedings of the National Academy of Sciences,U.S.A.* **105**, 3711–3714 (2008).

[129] Crassous, J. J. *et al.* Field-induced assembly of colloidal ellipsoids into well-defined microtubules. *Nature Communications* **5** (2014).

[130] Khalil, I. S., van den Brink, F., Sukas, O. S. & Misra, S. Microassembly using a cluster of paramagnetic microparticles. In *Robotics and Automation (ICRA), 2013 IEEE International Conference on*, 5527–5532 (IEEE, 2013).

[131] Floyd, S., Pawashe, C. & Sitti, M. Two-dimensional contact and noncontact micromanipulation in liquid using an untethered mobile magnetic microrobot. *IEEE Transactions on Robotics* **25**, 1332–1342 (2009).

[132] El-Gazzar, A. G., Al-Khouly, L. E., Klingner, A., Misra, S. & Khalil, I. S. Non-contact manipulation of microbeads via pushing and pulling using magnetically controlled clusters of paramagnetic microparticles. In *2015 IEEE/RSJ International Conference on Intelligent Robots and Systems (IROS)*, 778–783 (IEEE, 2015).

[133] Liu, I. B., Sharifi-Mood, N. & Stebe, K. J. Curvature-driven assembly in soft matter. *Phil. Trans. R. Soc. A* **374**, 20150133 (2016).

[134] Botto, L., Yao, L., Leheny, R. & Stebe, K. Capillary bond between rod-like particles and the micromechanics of particle-laden interfaces. *Soft Matter* **8**, 4971–4979 (2012).

[135] Snezhko, A. & Aranson, I. S. Magnetic manipulation of self-assembled colloidal asters. *Nature materials* **10**, 698 (2011).

[136] Cavallaro, M., Botto, L., Lewandowski, E. P., Wang, M. & Stebe, K. J. Curvature-driven capillary migration and assembly of rod-like particles. *Proc. Natl. Acad. Sci. U.S.A.* **108**, 20923–20928 (2011).

[137] Yao, L., Sharifi-Mood, N., Liu, I. B. & Stebe, K. J. Capillary migration of microdisks on curved interfaces. *Journal of Colloid and Interface Science* **449**, 436–442 (2015).

[138] Kaz, D. M., McGorty, R., Mani, M., Brenner, M. P. & Manoharan, V. N. Physical ageing of the contact line on colloidal particles at liquid interfaces. *Nature Materials* **11**, 138 (2012).

[139] Gifford, W. & Scriven, L. On the attraction of floating particles. *Chemical Engineering Science* **26**, 287–297 (1971).

[140] Bowden, N., Terfort, A., Carbeck, J. & Whitesides, G. M. Self-assembly of mesoscale objects into ordered two-dimensional arrays. *Science* **276**, 233–235 (1997).

[141] Bowden, N., Choi, I. S., Grzybowski, B. A. & Whitesides, G. M. Mesoscale self-assembly of hexagonal plates using lateral capillary forces: synthesis using the "capillary bond". *Journal of the American Chemical Society* **121**, 5373–5391 (1999).

[142] Bowden, N., Arias, F., Deng, T. & Whitesides, G. M. Self-assembly of microscale objects at a liquid/liquid interface through lateral capillary forces. *Langmuir* **17**, 1757–1765 (2001).

[143] Stamou, D., Duschl, C. & Johannsmann, D. Long-range attraction between colloidal spheres at the air-water interface: The consequence of an irregular meniscus. *Physical Review E* **62**, 5263 (2000).

[144] Sharifi-Mood, N., Liu, I. B. & Stebe, K. J. Curvature capillary migration of microspheres. *Soft Matter* **11**, 6768–6779 (2015).

[145] Yao, L. *et al.* Near field capillary repulsion. *Soft Matter* **9**, 779–786 (2013).

[146] Liu, I. B., Bigazzi, G., Sharifi-Mood, N., Yao, L. & Stebe, K. J. Curvature capillary repulsion. *Physical Review Fluids* **2**, 100501 (2017).

[147] Wong, D., Steager, E. B. & Kumar, V. Independent control of identical magnetic robots in a plane. *IEEE Robotics and Automation Letters* **1**, 554–561 (2016).

[148] Grosjean, G. *et al.* Remote control of self-assembled microswimmers. *Scientific reports* **5**, 1–8 (2015).

[149] Paunov, V. N. Novel method for determining the three-phase contact angle of colloid particles adsorbed at air- water and oil- water interfaces. *Langmuir* **19**, 7970–7976 (2003).

[150] Brakke, K. A. The surface evolver. *Experimental Mathematics* **1**, 141–165 (1992).

[151] Dani, A., Keiser, G., Yeganeh, M. & Maldarelli, C. Hydrodynamics of particles at an oil–water interface. *Langmuir* **31**, 13290–13302 (2015).

[152] Lauga, E. Bacterial hydrodynamics. *Annual Review of Fluid Mechanics* **48**, 105–130 (2016).

[153] Sokolov, A., Aranson, I. S., Kessler, J. O. & Goldstein, R. E. Concentration dependence of the collective dynamics of swimming bacteria. *Physical review letters* **98**, 158102 (2007).

[154] Rafaï, S., Jibuti, L. & Peyla, P. Effective viscosity of microswimmer suspensions. *Physical Review Letters* **104**, 098102 (2010).

[155] Petroff, A. P., Wu, X.-L. & Libchaber, A. Fast-moving bacteria self-organize into active two-dimensional crystals of rotating cells. *Physical review letters* **114**, 158102 (2015).

[156] Lopez, D. & Lauga, E. Dynamics of swimming bacteria at complex interfaces. *Physics of Fluids* **26**, 400–412 (2014).

[157] Molaei, M., Barry, M., Stocker, R. & Sheng, J. Failed escape: solid surfaces prevent tumbling of escherichia coli. *Physical review letters* **113**, 068103 (2014).

[158] Espinosa-Garcia, J., Lauga, E. & Zenit, R. Fluid elasticity increases the locomotion of flexible swimmers. *Physics of Fluids* **25**, 031701 (2013).

[159] Qiu, T. *et al.* Swimming by reciprocal motion at low reynolds number. *Nature communications* **5**, 1–8 (2014).

[160] Stark, H. Physics of colloidal dispersions in nematic liquid crystals. *Physics Reports* **351**, 387–474 (2001).

[161] Lavrentovich, O. D. Active colloids in liquid crystals. *Current opinion in colloid & interface science* **21**, 97–109 (2016).

[162] Muševič, I. *Liquid crystal colloids* (Springer, 2017).

[163] Smalyukh, I. I. Liquid crystal colloids. *Annual Review of Condensed Matter Physics* **9**, 207–226 (2018).

[164] Lavrentovich, O. D. Design of nematic liquid crystals to control microscale dynamics. *Liquid Crystals Reviews* 1–148 (2021).

[165] Mushenheim, P. C., Trivedi, R. R., Tuson, H. H., Weibel, D. B. & Abbott, N. L. Dynamic self-assembly of motile bacteria in liquid crystals. *Soft Matter* **10**, 88–95 (2014).

[166] Peng, C., Turiv, T., Guo, Y., Wei, Q.-H. & Lavrentovich, O. D. Command of active matter by topological defects and patterns. *Science* **354**, 882–885 (2016).

[167] Krüger, C., Klös, G., Bahr, C. & Maass, C. C. Curling liquid crystal microswimmers: A cascade of spontaneous symmetry breaking. *Physical review letters* **117**, 048003 (2016).

[168] Lapointe, C. *et al.* Elastic torque and the levitation of metal wires by a nematic liquid crystal. *Science* **303**, 652–655 (2004).

[169] Rovner, J. B., Borgnia, D. S., Reich, D. H. & Leheny, R. L. Elastic and hydrodynamic torques on a colloidal disk within a nematic liquid crystal. *Physical Review E* **86**, 041702 (2012).

[170] Yuan, Y., Liu, Q., Senyuk, B. & Smalyukh, I. I. Elastic colloidal monopoles and reconfigurable self-assembly in liquid crystals. *Nature* **570**, 214–218 (2019).

[171] De Gennes, P.-G. & Prost, J. *The physics of liquid crystals*, vol. 83 (Oxford university press, 1993).

[172] Xia, Y., Cedillo-Servin, G., Kamien, R. D. & Yang, S. Guided folding of nematic liquid crystal elastomer sheets into 3d via patterned 1d microchannels. *Advanced Materials* **28**, 9637–9643 (2016).

[173] Agha, H., Fleury, J.-B. & Galerne, Y. Micro-wires self-assembled and 3d-connected with the help of a nematic liquid crystal. *The European Physical Journal E* **35**, 1–12 (2012).

[174] McConney, M. *et al.* Topography from topology: photoinduced surface features generated in liquid crystal polymer networks. *Advanced Materials* **25**, 5880 (2013).

[175] Peng, C. *et al.* Liquid crystals with patterned molecular orientation as an electrolytic active medium. *Physical Review E* **92**, 052502 (2015).

[176] Peng, C. *et al.* Control of colloidal placement by modulated molecular orientation in nematic cells. *Science advances* **2**, e1600932 (2016).

[177] Lavrentovich, O. D. Topological defects in dispersed words and worlds around liquid crystals, or liquid crystal drops. *Liq. Cryst.* **24**, 117–126 (1998).

[178] Lavrentovich, O. D. Transport of particles in liquid crystals. *Soft Matter* **10**, 1264–1283 (2014).

[179] Hung, F. R., Guzmán, O., Gettelfinger, B. T., Abbott, N. L. & de Pablo, J. J. Anisotropic nanoparticles immersed in a nematic liquid crystal: Defect structures and potentials of mean force. *Physical Review E* **74**, 011711 (2006).

[180] Tasinkevych, M., Mondiot, F., Mondain-Monval, O. & Loudet, J.-C. Dispersions of ellipsoidal particles in a nematic liquid crystal. *Soft Matter* **10**, 2047–2058 (2014).

[181] Beller, D. A., Gharbi, M. A. & Liu, I. B. Shape-controlled orientation and assembly of colloids with sharp edges in nematic liquid crystals. *Soft Matter* **11**, 1078–1086 (2015).

[182] Lapointe, C. P., Mason, T. G. & Smalyukh, I. I. Shape-controlled colloidal interactions in nematic liquid crystals. *Science* **326**, 1083–1086 (2009).

[183] Senyuk, B. *et al.* Topological colloids. *Nature* **493**, 200–205 (2013).

[184] Nikkhou, M. & Muševič, I. Geometric stabilisation of topological defects on micro-helices and grooved rods in nematic liquid crystals. *Soft matter* **14**, 9819–9829 (2018).

[185] Ravnik, M. *et al.* Entangled nematic colloidal dimers and wires. *Physical Review Letters* **99**, 247801 (2007).

[186] Čopar, S., Tkalec, U., Muševič, I. & Žumer, S. Knot theory realizations in nematic colloids. *Proceedings of the National Academy of Sciences* **112**, 1675–1680 (2015).

[187] Silvestre, N., Patricio, P. & da Gama, M. T. Key-lock mechanism in nematic colloidal dispersions. *Physical Review E* **69**, 061402 (2004).

[188] Hung, F. R., Gettelfinger, B. T., Koenig Jr, G. M., Abbott, N. L. & de Pablo, J. J. Nanoparticles in nematic liquid crystals: Interactions with nanochannels. *The Journal of chemical physics* **127**, 124702 (2007).

[189] Eskandari, Z., Silvestre, N., da Gama, M. T. & Ejtehadi, M. Particle selection through topographic templates in nematic colloids. *Soft Matter* **10**, 9681–9687 (2014).

[190] Silvestre, N. M., Liu, Q., Senyuk, B., Smalyukh, I. I. & Tasinkevych, M. Towards template-assisted assembly of nematic colloids. *Physical review letters* **112**, 225501 (2014).

[191] Peng, C. *et al.* Controlling placement of nonspherical (boomerang) colloids in nematic cells with photopatterned director. *Journal of Physics: Condensed Matter* **29**, 014005 (2016).

[192] Luo, Y., Serra, F. & Stebe, K. J. Experimental realization of the "lock-and-key" mechanism in liquid crystals. *Soft Matter* **12**, 6027–6032 (2016).

[193] Silvestre, N. M. & Tasinkevych, M. Key-lock colloids in a nematic liquid crystal. *Physical Review E* **95**, 012606 (2017).

[194] Luo, Y., Beller, D. A., Boniello, G., Serra, F. & Stebe, K. J. Tunable colloid trajectories in nematic liquid crystals near wavy walls. *Nature communications* **9**, 1–11 (2018).

[195] Luo, Y., Yao, T., Beller, D. A., Serra, F. & Stebe, K. J. Deck the walls with anisotropic colloids in nematic liquid crystals. *Langmuir* **35**, 9274–9285 (2019).

[196] Smalyukh, I. I., Shiyanovskii, S. & Lavrentovich, O. Three-dimensional imaging of orientational order by fluorescence confocal polarizing microscopy. *Chemical Physics Letters* **336**, 88–96 (2001).

[197] Beris, A. N., Edwards, B. J. *et al. Thermodynamics of flowing systems: with internal microstructure.* 36 (Oxford University Press on Demand, 1994).

[198] Kleman, M. & Lavrentovich, O. *Soft Matter Physics: An Introduction* (Springer-Verlag, New York, 2003).

[199] Škarabot, M. *et al.* Two-dimensional dipolar nematic colloidal crystals. *Physical Review E* **76**, 051406 (2007).

[200] Alexander, G. P., Chen, B. G.-g., Matsumoto, E. A. & Kamien, R. D. Colloquium: Disclination loops, point defects, and all that in nematic liquid crystals. *Reviews of Modern Physics* **84**, 497 (2012).

[201] Martinez-Pedrero, F. & Tierno, P. Magnetic propulsion of self-assembled colloidal carpets: efficient cargo transport via a conveyor-belt effect. *Physical Review Applied* **3**, 051003 (2015).

[202] Han, K. *et al.* Reconfigurable structure and tunable transport in synchronized active spinner materials. *Science advances* **6**, eaaz8535 (2020).

[203] Bricard, A., Caussin, J.-B., Desreumaux, N., Dauchot, O. & Bartolo, D. Emergence of macroscopic directed motion in populations of motile colloids. *Nature* **503**, 95–98 (2013).

[204] Muševič, I., Škarabot, M., Tkalec, U., Ravnik, M. & Žumer, S. Two-dimensional nematic colloidal crystals self-assembled by topological defects. *Science* **313**, 954–958 (2006).

[205] Tkalec, U. & Muševič, I. Topology of nematic liquid crystal colloids confined to two dimensions. *Soft Matter* **9**, 8140–8150 (2013).

[206] Škarabot, M. *et al.* Hierarchical self-assembly of nematic colloidal superstructures. *Phy. Rev. E* **77**, 061706 (2008).

[207] Legge, C. & Mitchell, G. Photo-induced phase transitions in azobenzene-doped liquid crystals. *J. Phys. D* **25**, 492 (1992).

[208] Kurihara, S. *et al.* Manipulation and assembly of small objects in liquid crystals by dynamical disorganizing effect of push-pull-azobenzene-dye. *Sci. Rep.* **3**, 2167 (2013).

[209] Pires, D., Fleury, J.-B. & Galerne, Y. Colloid particles in the interaction field of a disclination line in a nematic phase. *Physical Review Letters* **98**, 247801 (2007).

[210] Senyuk, B. *et al.* Shape-dependent oriented trapping and scaffolding of plasmonic nanoparticles by topological defects for self-assembly of colloidal dimers in liquid crystals. *Nano letters* **12**, 955–963 (2012).

[211] Whitmer, J. K. *et al.* Nematic-field-driven positioning of particles in liquid crystal droplets. *Physical review letters* **111**, 227801 (2013).

[212] Wang, X. *et al.* Experimental insights into the nanostructure of the cores of topological defects in liquid crystals. *Phys. Rev. Lett.* **116**, 147801 (2016).

[213] Sengupta, A., Bahr, C. & Herminghaus, S. Topological microfluidics for flexible micro-cargo concepts. *Soft Matter* **9**, 7251–7260 (2013).

[214] Bhadwal, A., Mottram, N., Saxena, A., Sage, I. & Brown, C. Electrically controlled topological micro cargo transportation. *Soft matter* **16**, 2961–2970 (2020).

[215] Nikkhou, M. *et al.* Light-controlled topological charge in a nematic liquid crystal. *Nature physics* **11**, 183 (2015).

[216] Fleury, J.-B., Pires, D. & Galerne, Y. Self-connected 3d architecture of microwires. *Phys. Rev. Lett.* **103**, 267801 (2009).

[217] Fischer, E. Einfluss der configuration auf die wirkung der enzyme. *Ber. deutsch. chem. Gesell.* **27**, 2985–2993 (1894).

[218] Sacanna, S., Irvine, W., Chaikin, P. M. & Pine, D. J. Lock and key colloids. *Nature* **464**, 575–578 (2010).

[219] König, P.-M., Roth, R. & Dietrich, S. Lock and key model system. *Eur. Phys. J.* **84**, 68006 (2009).

[220] Law, C., Ashton, D. J., Wilding, N. B. & Jack, R. L. Coarse-grained depletion potentials for anisotropic colloids: Application to lock-and-key systems. *The Journal of chemical physics* **145**, 084907 (2016).

[221] Terentjev, E. Disclination loops, standing alone and around solid particles, in nematic liquid crystals. *Phys. Rev. E* **51**, 1330 (1995).

[222] Senyuk, B., Liu, Q., Nystrom, P. D. & Smalyukh, I. I. Repulsion–attraction switching of nematic colloids formed by liquid crystal dispersions of polygonal prisms. *Soft Matter* **13**, 7398–7405 (2017).

[223] Tkalec, U., Škarabot, M. & Muševič, I. Interactions of micro-rods in a thin layer of a nematic liquid crystal. *Soft matter* **4**, 2402–2409 (2008).

[224] Mondiot, F., Chandran, S. P., Mondain-Monval, O. & Loudet, J.-C. Shape-induced dispersion of colloids in anisotropic fluids. *Physical review letters* **103**, 238303 (2009).

[225] Gharbi, M. A. *et al.* Micro-bullet assembly: Interactions of oriented dipoles in confined nematic liquid crystal. *arXiv preprint arXiv:1210.1881* (2012).

[226] Gennes, P.-G. D. & Prost, J. *The Physics of Liquid Crystals* (Oxford University Press, 1993).

[227] Pishnyak, O. P., Tang, S., Kelly, J., Shiyanovskii, S. V. & Lavrentovich, O. D. Levitation, lift, and bidirectional motion of colloidal particles in an electrically driven nematic liquid crystal. *Phys. Rev. Lett.* **99**, 127802 (2007).

[228] Zhang, S., Pelligra, C. I., Feng, X. & Osuji, C. O. Directed assembly of hybrid nanomaterials and nanocomposites. *Advanced Materials* **30**, 1705794 (2018).

[229] Mayer, M., Schnepf, M. J., König, T. A. & Fery, A. Colloidal self-assembly concepts for plasmonic metasurfaces. *Advanced Optical Materials* **7**, 1800564 (2019).

[230] Chen, Y., Ai, B. & Wong, Z. J. Soft optical metamaterials. *Nano Convergence* **7**, 1–17 (2020).

[231] Sitti, M. Voyage of the microrobots. *Nature* **458**, 1121–1122 (2009).

[232] Cavallaro Jr, M. *et al.* Ring around the colloid. *Soft Matter* **9**, 9099–9102 (2013).

[233] Eelkema, R. & Feringa, B. L. Amplification of chirality in liquid crystals. *Organic & biomolecular chemistry* **4**, 3729–3745 (2006).

[234] Boniello, G., Luo, Y., Beller, D. A., Serra, F. & Stebe, K. J. Colloids in confined liquid crystals: a plot twist in the lock-and-key mechanism. *Soft matter* **15**, 5220–5226 (2019).

[235] Smalyukh, I. I., Kuzmin, A., Kachynski, A., Prasad, P. & Lavrentovich, O. Optical trapping of colloidal particles and measurement of the defect line tension and colloidal forces in a thermotropic nematic liquid crystal. *Applied Physics Letters* **86**, 021913 (2005).

[236] Stokes, G. G. *et al.* On the effect of the internal friction of fluids on the motion of pendulums (1851).

[237] Danov, K., Aust, R., Durst, F. & Lange, U. Influence of the surface viscosity on the hydrodynamic resistance and surface diffusivity of a large brownian particle. *Journal of colloid and interface science* **175**, 36–45 (1995).

[238] Danov, K. D., Dimova, R. & Pouligny, B. Viscous drag of a solid sphere straddling a spherical or flat surface. *Physics of Fluids* **12**, 2711–2722 (2000).

[239] Pozrikidis, C. Particle motion near and inside an interface. *Journal of Fluid Mechanics* **575**, 333–357 (2007).

[240] Petkov, J. T. *et al.* Measurement of the drag coefficient of spherical particles attached to fluid interfaces. *Journal of colloid and interface science* **172**, 147–154 (1995).

[241] Vassileva, N. D., van den Ende, D., Mugele, F. & Mellema, J. Capillary forces between spherical particles floating at a liquid- liquid interface. *Langmuir* **21**, 11190–11200 (2005).

[242] Ally, J. & Amirfazli, A. Magnetophoretic measurement of the drag force on partially immersed microparticles at air–liquid interfaces. *Colloids and Surfaces A: Physicochemical and Engineering Aspects* **360**, 120–128 (2010).

[243] Batchelor, G. Brownian diffusion of particles with hydrodynamic interaction. *Journal of Fluid Mechanics* **74**, 1–29 (1976).

[244] Dalbe, M.-J., Cosic, D., Berhanu, M. & Kudrolli, A. Aggregation of frictional particles due to capillary attraction. *Physical Review E* **83**, 051403 (2011).

[245] Boneva, M. P., Christov, N. C., Danov, K. D. & Kralchevsky, P. A. Effect of electric-field-induced capillary attraction on the motion of particles at an oil–water interface. *Physical chemistry chemical physics* **9**, 6371–6384 (2007).

[246] Boneva, M. P., Danov, K. D., Christov, N. C. & Kralchevsky, P. A. Attraction between particles at a liquid interface due to the interplay of gravity-and electric-field-induced interfacial deformations. *Langmuir* **25**, 9129–9139 (2009).

[247] Deen, W. M. *Analysis of transport phenomena*, vol. 2 (Oxford university press New York, 1998).

[248] Leal, L. G. *Advanced transport phenomena: fluid mechanics and convective transport processes*, vol. 7 (Cambridge University Press, 2007).

[249] Brenner, H. The stokes resistance of an arbitrary particle—iv arbitrary fields of flow. *Chemical Engineering Science* **19**, 703–727 (1964).